Smart Materials for Advanced Applications: Self-Decontaminating Polymers, Photofunctional Composites, and Electroconductive Fibers

by

Brian Kevin Little

A dissertation submitted to the Graduate Faculty of
Auburn University
in partial fulfillment of the
requirements for the Degree of
Doctor of Philosophy

Auburn, Alabama
May 9, 2011

Keywords: smart materials, photochemistry, high energy chemistry, electroconductive fibers

Approved by

German Mills, Chair, Associate Professor of Chemistry
Rik Blumenthal, Associate Professor of Chemistry
Vincenzo Cammarata, Associate Professor of Chemistry
Curtis Shannon, Professor of Chemistry

Abstract

Materials capable of providing multifunctional properties controllable by some external stimulus (pH, light, temperature, etc) are highly desirable and obtainable given recent advancements in material science. Development of these so called “Smart” materials spanned across many disciplines of science with applications in industrial areas such as medical, military, security, and environmental. Furthermore, next-generation materials require the ability to not only sense/respond to changes in their external/internal environment, but process information in regards to these changes and adapt accordingly in a dynamic fashion, autonomously, so called “Intelligent” materials. Findings reported in this manuscript detail the synthesis, characterization, and application of smart materials in the following three areas: 1) self-cleaning polymers 2) photoresponsive composites and 3) electroconductive fibers.

Self-Cleaning Polymers: Self-decontaminating polymers are unique materials capable of degrading toxic organic chemicals (TOCs). Barriers composed of or coated with our photochemical reactive polymer matrix could be applied to multiple surfaces for defense against TOCs; for example, military garments for protection against chemical warfare agents. This study investigates conditions necessary for formation of peroxides via O_2 reduction induced by long-lived, strongly reducing benzophenyl ketyl (BPK) polymer radicals. Photolysis of aqueous solutions composed of sulphonated poly(ether etherketone), SPEEK, and poly(vinyl alcohol), PVA lead to the formation of the BPK radicals. Experiments investigate the formation and decomposition of peroxides in aqueous solutions of SPEEK/PVA under photolysis.

Photofunctional Composites: Photoresponsive nanoporous (PN) films and powders were studied and evaluated as possible additives to sensitize the initiation of CH_3NO_2 via a mechanism involving coalescence of reaction sites. Such materials consist of a 3-D mesoporous silica framework possessing open interconnected pores. Attached to the pore walls are azobenzene ligands that undergo *trans* to *cis* isomerization upon exposure to 350-360 nm photons; the reverse reaction occurs with heat or under illumination with $\lambda > 420$ nm. PN films were studied to ascertain the mass transport properties for the filling/releasing of CH_3NO_2 from within the pores of the films in the absence/presence of UV-Vis light. PN powders were evaluated for pore morphology, ligand mobility, and particle size and shape in order to determine their ability to be utilized as an effective sensitizing agent.

Electroconductive Fibers: This study investigates electroless and electrochemical techniques for purposes of producing highly conductive metal coatings on the surface of high strength fibers. Metallized fibers were envisioned to be utilized as high strength low weight tethers for space applications. Findings suggest that these materials could be valuable as components within "Intelligent" textiles, but, at present, not suitable for conditions witnessed in space (high energy UV irradiation, Atomic Oxygen, etc). Kevlar fibers were coated utilizing an electroless and then electrochemical deposition processes. Metallized fibers were evaluated for their resistivity, power output, tensile strength, uniform coverage, and mass gain. Presented in this section are the results of such measurements.

Acknowledgments

The author would like to graciously thank German Mills. Professor Mills has been and will continue to have an influential impact on my knowledge of chemistry and my future development as an independent scientist. Thanks are given to Professor Buster Slaten for his never ending source of pursuance and insight throughout this project. Thanks are extended to members of the author's committee and others including Rik Blumenthal, Vince Cammarata, Curtis Shannon, Mike Lindsay and German Mills for their guidance and time.

Gratitude is extended to the following funding agencies for support of this research: NASA (contract # NASA-NCC8-237-MTM), NTC (contract # C06-AC01), and AFRL (contract # BAA-RWK-08-0001).

The author would like to thank his parents, David and Pam Little and siblings, Bradd, Erik, Brett, Zachary and Sara Little for their untiring feelings of love and encouragement. Special thanks are given to my wife Alisa and two daughters, Carmen and Tristan for their undying love and support.

Table of Contents

List of Tables

List of Figures

List of Abbreviations

Å	angstrom
$^{\circ}$C	degrees Celsius
cm	centimeter
ε	extinction coefficient
e^-	electron
E^o	potential energy, redox potential
EPR	electron paramagnetic resonance
fcc	face cubic center
FT	Fourier transform
g	gram
h	hour
hν	photon
I_o	light intensity
IR	infrared
K	Kelvin
keV	kiloelectron volt
k_1	rate constant for first step
k_2	rate constant for second step
λ	wavelength

L	Liter
M	molar concentration
M^x	metal ion
µm	micrometer
mol	mol
MW	molecular weight
min	minute
mL	milliter
mm	millimeter
nm	nanometer
NMR	nuclear magnetic resonance
O.D.	optical density
pH	$-\log[H^+]$
PVA	poly(vinyl alcohol)
s	second
SEM	scanning electron microscopy
t	time
TEM	transmission electron microscopy
UV	ultraviolet light
Vis	visible light
W	watt
wt	weight
XRD	x-ray diffraction

I. DEVELOPMENT OF SMART MATERIALS

Evolution of Material Functionality

Since mankind's discovery of simple materials such as stone, bronze, and iron, human civilization has prospered in many areas with advances in weapons, pottery, construction materials, and multiple types of tools. These discoveries were so influential in our history that periods in time were named after these materials (Stone Age, Bronze Age, and Iron Age). However, as influential as these resources were to our way of living, progress was slow toward applying these materials to new areas outside what was initially accomplished. Advances in the design and application of materials require greater insight into macroscale properties (brittleness, color, ductility) and their association with the underlying molecular structure of the material. For instance, the discovery of synthetic materials *e.g.* plastics, through polymer chemistry, led to materials designed and applied across multiple fields of science and technology in an exponential manner that is continuing at this very moment.

Nevertheless, all materials described above are valued for possessing either a structural or functional property (elasticity, conductivity, hardness), but not both, and are therefore limited in their use towards more advanced applications. Tables 1-1, 1-2, and 1-3 are examples of structural and functional materials and their inherent properties.[1] Materials listed in Tables 1-1 through 1-3, are classified as structural, functional, and poly-functional, respectfully. A structural material would be considered a substance that possesses an ideal property, given the application, such as steel versus wood for composing a tool, *e.g.* an axe. Materials containing functional properties are chosen not based on their structure as much as their ability to perform a unique process, for example germanium (germanium is a photoconductive material able to absorb light and

subsequently generate a current). Poly-functional materials are able to deliver more than one function such as lead zirconate titanate, which can actually perform three functions (piezoelectricity, pyroelectricity, and ferroelectricity).

Scientists have recognized through the study of biological systems, that the next big jump in human civilization will come from the ability to synthesize "intelligent" materials which possess both structural and functional capabilities that operate **autonomously** based on specific conditions within their environment (pH, temperature, light intensity …etc). Couple this insight with the advancements in nanoengineering across so many broad disciplines of science in combination with the ability to access information via the internet, and with the possible discovery of practical renewable energy sources, intelligent materials will be unbound in their impact towards the improvements of human civilization marking the next era in the material age. It is important to note that there are many definitions for smart materials, but at a minimum, most are confined to materials with the ability to change one or more functions significantly given some outside stimulus. [2-4] Given this definition of smart materials, functional and poly-functional materials are considered "smart" materials. For the purpose of clarity and relevance to the research results reported in the following chapters, smart materials will contain ideal structural properties and sensing or actuating functionality that can be significantly altered in a controlled fashion by some type of external stimulus (pH, light, temperature, pressure, etc). Furthermore, the term "intelligent" materials is commonly used to describe smart materials, however inappropriately, given that the word intelligent suggests the ability to learn, gain knowledge, and adapt, which would not be the case for smart materials. An intelligent material could be a material composed of smart materials, but in addition has the ability to process information and "learn" to adapt to its surrounding environmental conditions.

Table 1-1. Structural materials. Adapted from Gandhi *et al.*[1]

Material
Steel
Polycarbonate
Wood
Iron
Concrete
Graphite-epoxy laminates

Table 1-2. Functional materials. Adapted from Gandhi *et al.*[1]

Material	**Properties**
Nickel-titanium	shape-memory
Cadmium sulphide	piezoelectric
Terbium iron	magnetostrictive
Quartz	pyroelectric
Electro-rheological fluids	viscoplastic
Aluminum soap solution	viscoelastic
Barium titanate	ferroelectric
Copper oxide	photoelectric
Potassium dihydrogen phosphate	electro-optic
Selenium	photoelectric
Germanium	photoconductive

Table 1-3. Poly-functional materials. Adapted from Gandhi *et al*.[1]

Material	**Properties**
Lead zirconate titanates	Piezoelectric
	Pyroelectric
	Ferroelectric
Bone	Mineral Homeostasis
	Structural Homeostasis
	Piezoelectric
	Pyroelectric
Lead-magnesium niobate	Thermo-electrostrictive
Terbium-iron-dysprosium	Thermo-magnetostrictive

Actuators and Sensors

The ability of some smart materials to detect and respond to their environment is a critical process for next generation intelligent materials or systems. As stated earlier, intelligent materials have the ability to adapt to their surrounding conditions dynamically from some form of learning (knowledge), which requires the capability to sense changes (sensor) in their environment and act accordingly *i.e.* actuation. Actuator is a material that simply converts some form of energy into output, usually mechanical (motion). Figure 1-1 shows a schematic for a dielectric elastomer actuator (DEA). DEA are basically rubber capacitors, composed of two electrodes which have a dielectric polymer film sandwiched between their surfaces.

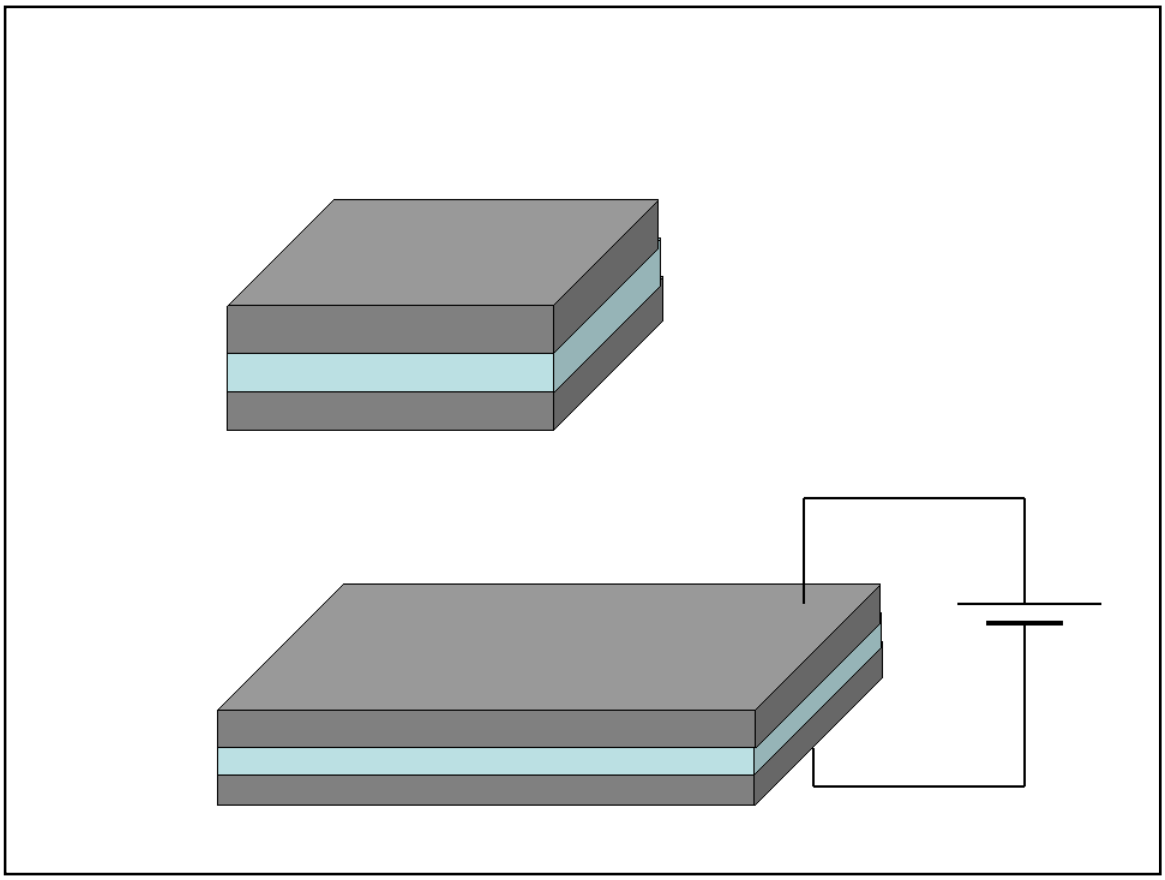

Figure 1 - 1. Schematic for a DEA (rubbery capacitor). When a potential difference is applied between the two electrodes, the two oppositely charged electrodes are attracted to one another causing compression of the film in the direction of the electric field, thus expanding the film in perpendicular directions.[5]

Upon placing a voltage across the rubber capacitor, positive charges begin to accumulate on one electrode as negative charges build-up on the other electrode (this induces an attraction between the two electrodes), thus compressing the dielectric polymer film.

Dielectric elastomers are used in many applications given that they are constructed of low-cost materials and provide reliable performance capabilities. Of particular interest is the possibility of utilizing these materials as artificial muscle actuators in robotics given that they can be electrically stimulated to induce motion similar to the behavior of natural muscle. Table 1

- 4 is a list of artificial muscle actuator technologies and natural muscle along with their relevant properties.

Sensors on the other hand, are materials capable of associating the intensity of the stimulus to some event such as stress, strain, temperature, radiation, or chemical change as a signal that can be read by an observer or instrument. One of the most common types of sensors in the field of smart materials is piezoelectric sensors. Piezoelectric sensors transform an imposed pressure into a change in electrical charge on their surface *i.e.* piezoelectricity. Conversely, these same materials show a proportional link with the generated geometric strain from an applied electric field. In other words, these materials can convert mechanical energy into electrical energy or vice versa, which makes them very useful as sensors and/or actuators. Piezoelectric materials are utilized in diverse appliances which require the generation of a charge or high voltage such as spark ignition of gas heaters, cooking stoves, and cigarette lighters as well as analytical devices like microbalances. Piezoelectric actuators are commonly used as ultrasonic transducers by converting electrical energy into sound from oscillations within the crystal. Piezoelectric sensor/actuators can be engineered from different compositions (single-crystal materials, piezopolymers, piezocomposites, and piezofilms), based on the desired function, making them highly attractive across many different disciplines of science and industry. Furthermore, it is not uncommon for some smart materials to contain both sensor and actuator capabilities as pointed out with piezoelectric materials and which is also true for some dielectric elastomers. Application of smart materials can be witnessed across multiple areas of technology in such fields as surface coatings, medical, defense, solar energy, and aerospace to just name a few. While there are many review articles on the different types of smart materials, their preferred

Table 1 – 4. Comparison of artificial muscle actuator technologies and natural muscle. Adapted from Shahinpoor and Kornbluh.[5,6]

Actuator type (*specific example*)	**Max. strain (%)**	**Max. press. (MPa)**	**Max. efficiency (%)**	**Relative speed (full cycle)**
Dielectric elastomers				
Acrylic	**380**	**8.2**	**60-80**	**Medium**
Silicone	**63**	**3.0**	**90**	**Fast**
Electrostrictive polymer				
Graft Elastomer	**4**	**24**	**—**	**Fast**
Piezoelectric				
Ceramic (PZT)[a]	**0.2**	**110**	**>90**	**Fast**
Single crystal (PZN-PT)	**1.7**	**131**	**>90**	**Fast**
Polymer (PVDF)[b]	**0.1**	**4.8**	**n/a**	**Fast**
Shape-memory alloy (TiNi)	**>5**	**>200**	**<10**	**Slow**
Thermal (expansion)[c]	**1**	**78**	**<10**	**Slow**
Electrochemomechanical conducting polymer (polyaniline)	**10**	**450**	**<1**	**Slow**
Mechanochemical polymer/gels (polyelectrolyte)	**>40**	**0.3**	**30**	**Slow**
Natural muscle (human skeletal)	**>40**	**0.35**	**>35**	**Medium**

[a] PZT B, at a maximum electric field of 4 V/μm; [b] PVDF, at a maximum electric field of 30 V/μm; [c] Aluminum, with a temperature change of 500 °C;

area of application, and their impact in particular markets, it is the intent of this author to focus on certain kinds of smart materials and not to provide an exhausting review on the subject.[7-11] Therefore, the following sections will be devoted to smart materials within the areas of self-cleaning composites, photofunctional materials, and electroconductive fibers given that these materials are more relevant to the research results contained in the following chapters of this manuscript.

Self-Cleaning Composites

Smart materials with self-cleaning properties are highly sought after for multiple applications like self-cleaning fibers *e.g.* to minimize odor and bacteria contamination, water treatment, water proofing coatings for water sensitive electronics, self-cleaning windows for automobiles and buildings, and stain resistant textiles.[12-15] In general, "self-cleaning" can be defined as the ability to keep a material's surface or interior free of contamination such as dirt, bacteria, or water. The two most common methods employed to achieve this function are super-hydrophobicity and photocatalytic decomposition. Scientists discovered in 1977 via SEM that lotus leafs have a unique ability to cleanse themselves of foreign particles by forming and rolling water droplets across their surface.[16] The ability of a surface to form a water droplet is dictated by the attraction of water to the surface versus that of water to itself. Surfaces that promote a high degree of water-water attraction are hydrophobic (repelling) thus forming near spherical water droplets and surfaces that promote surface-water interaction are called hydrophilic (dispersant), which consequently promotes the formation of flat puddles of water *i.e.* wetting the surface. The hydrophobicity on the surface of a leaf is due to the roughness of the surface, which facilitates a high contact angle (CA) with respect to the water droplet's side tangent to the plane of the

surface. In other words, contact angles greater than 90 degrees for the side of the liquid droplet tangent to the plane of the surface will induce hydrophobicity; contact angles greater than 150 degrees are called super-hydrophobic. Presented in Figure 1-2 is an illustration of the mechanism by which a rough super-hydrophobic surface promotes cleaning of contaminates by rolling spherical water droplets. Also notice in Figure 1-2, that a smooth super-hydrophobic surface is inefficient in creating spherical water droplets, hence flatter water droplets are not able to provide adequate self-cleaning.

Smart materials able to control the surface-water interactions can be highly useful for on/off self-cleaning processes such as the example in Figure 1-3. Lim *et al.* reported the ability to control the surface roughness effect of an inorganic oxide semiconductor substrate (WO_3, TiO_2, ZnO, SnO_2, V_2O_5, Ga_2O_3) by UV irradiation which switches the valence states (oxygen vacancies to hydroxyl groups) at the surface of the substrate in contact with a water droplet.[19] This photosensitive material was able to revert to the original state upon storing in the dark storage. Irradiation of the substrate in contact with the water droplet decreased the surface roughness by increasing the interaction between the water and the surface thus allowing water to adsorb and enter the microgrooves of the substrate facilitating wetting of the surface. Afterwards, it was noticed that while leaving the substrate in the dark, hydroxyl groups convert back to oxide groups, which lead to a water/air interface at the rough surface and promoted a super-hydrophobic effect, demonstrating the self-cleaning ability of the material. Figure 1-3a illustrates the switchable surface interaction properties of the substrate from super-hydrophobic to super-hydrophilic (after irradiation). Ultimately the surface roughness effect is controlled by the valence state of the inorganic oxide and not by a physical change in the surface morphology, which is a fixed structural property (see Figure 1-3b).

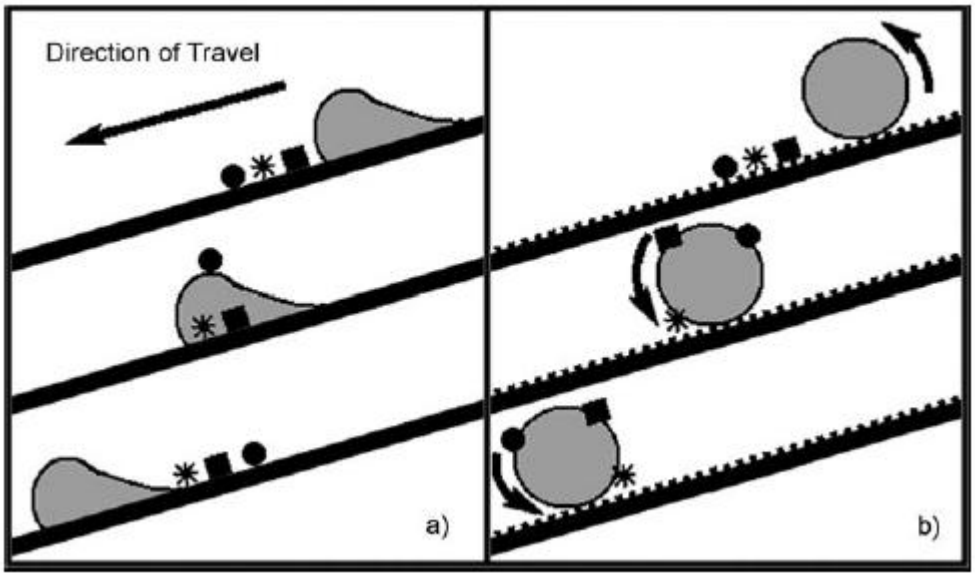

Figure 1-2. Diagram demonstrating the cleaning mechanism on smooth (a) and rough (b) super-hydrophobic surfaces. Reproduced with permission from ref 17. Copyright Wiley-VCH Verlag GmbH & Co. KGaA.

Photocatalytic decomposition, as stated earlier, is another common method for creating self-cleaning materials. TiO_2 is a very popular choice for composing self-cleaning materials especially for self-cleaning windows.[20] Inorganic oxide semiconductors such as TiO_2 can control the surface interaction of a water droplet by UV irradiation, which ultimately converts the droplet into a super-hydrophilic state. Another beneficial self-cleaning property of TiO_2 is its functionality as a strong oxidizer through activation by UV light.[21] When TiO_2 is irradiated with photons greater than its band gap energy, 3.0 eV (rutile) or 3.2 eV (anatase), excited charge carriers are formed in the conduction band, which in turn generates positively charged holes in the valence band.

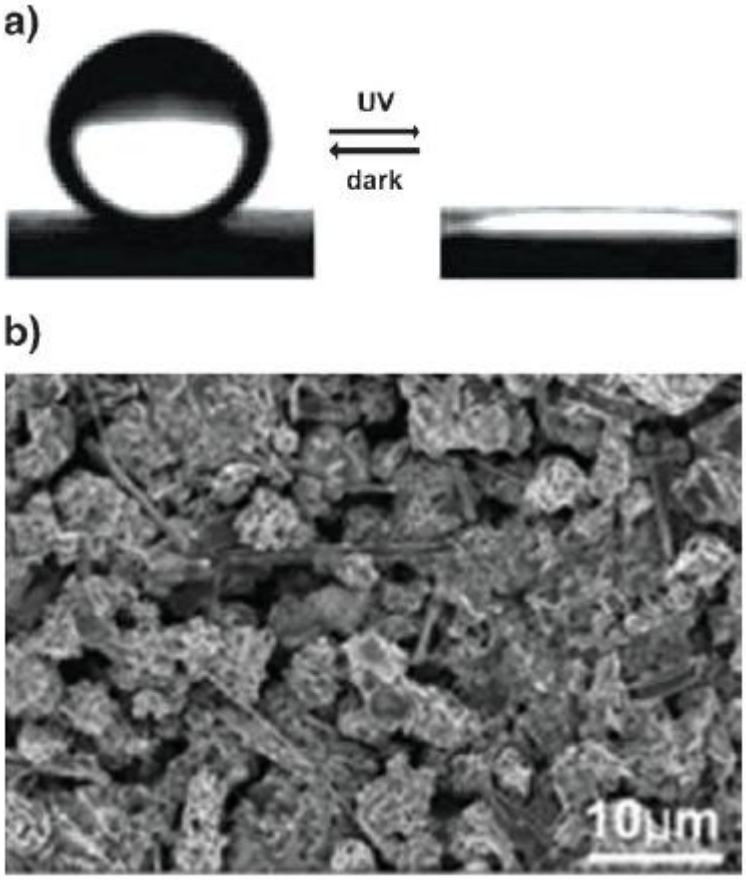

Figure 1-3. a) Water drop profiles for photoresponsive nanostructured V_2O_5 switching between super-hydrophobicity and super-hydrophilicity upon UV irradiation. b) SEM of the rose-garden-like nanostructure of the V_2O_5 substrate. Reproduced with permission from ref 18. Copyright Wiley-VCH Verlag GmbH & Co. KGaA.

These positive holes can oxidize water into hydroxyl radicals which can proceed to decomposed organic pollutants and/or the pollutants can be oxidized directly at the surface of the TiO_2 substrate by positive holes.[20] An example of this is shown in Figure 1-4, where Mills and Crow report the change in hydrophilicity of a water droplet as a function of UV irradiation time.[22] Of particular interest, with respect to how common these materials are, is the fact that the authors use a commercially available self-cleaning photocatalytic glass (Activ) as a standard for comparison against synthesized TiO_2 films. Experimentally a water droplet (~5 µm) was placed

onto the Activ TiO_2 coated glass substrate and irradiated with different wavelengths of UV light, UVC light (280 nm – 100 nm) or UVA light (400 nm – 315 nm), while monitoring the shape of the droplet (CA) as a function of UV irradiation. Initial tests conducted on Activ films showed an increase hydrophilicity during irradiation, where the shape of the water droplet flattens or CA becomes smaller, see Figure 1-4a. Furthermore, oxygen appears to facilitate this process as a sacrificial electron acceptor delaying the electron-hole recombination mechanism, see Figure 1-4b. Equally important was the fact that the authors showed the efficiency of TiO_2, under UV irradiation, to decompose an organic compound (stearic acid) within the water droplet in just a few minutes. Altogether, the above examples of self-cleaning smart materials illustrate the control of the self-cleaning mechanism strictly by surface roughness, *e.g.* lotus leaf, or through a combination of a rough semiconductor surface with photolysis.

Photofunctional Materials

Materials capable of responding to light are one of the most promising classes of smart materials. Obvious advantages with these materials are the fact that they are activated by light which has the following characteristics: free (natural light), easily tunable, an unlimited energy source, can be distributed remotely, and typically does not interfere with other components within the exposed material. Key components of these photofunctional smart materials are photoresponsive molecules. Of particular interest are photoresponsive molecules that exhibit mobility upon absorption of light. These molecules perform unique and specific molecular motions prearranged by their chemical structure and their surrounding matrix. Characterization of photoinduced molecular mobility have been described basically by three common chemical

events: 1) photodimerization (*e.g.* coumarins); 2) intramolecular photoinduced bond formation (*e.g.* spiro-pyrans); and 3) photoisomerization (*e.g.* azobenzene).[5]

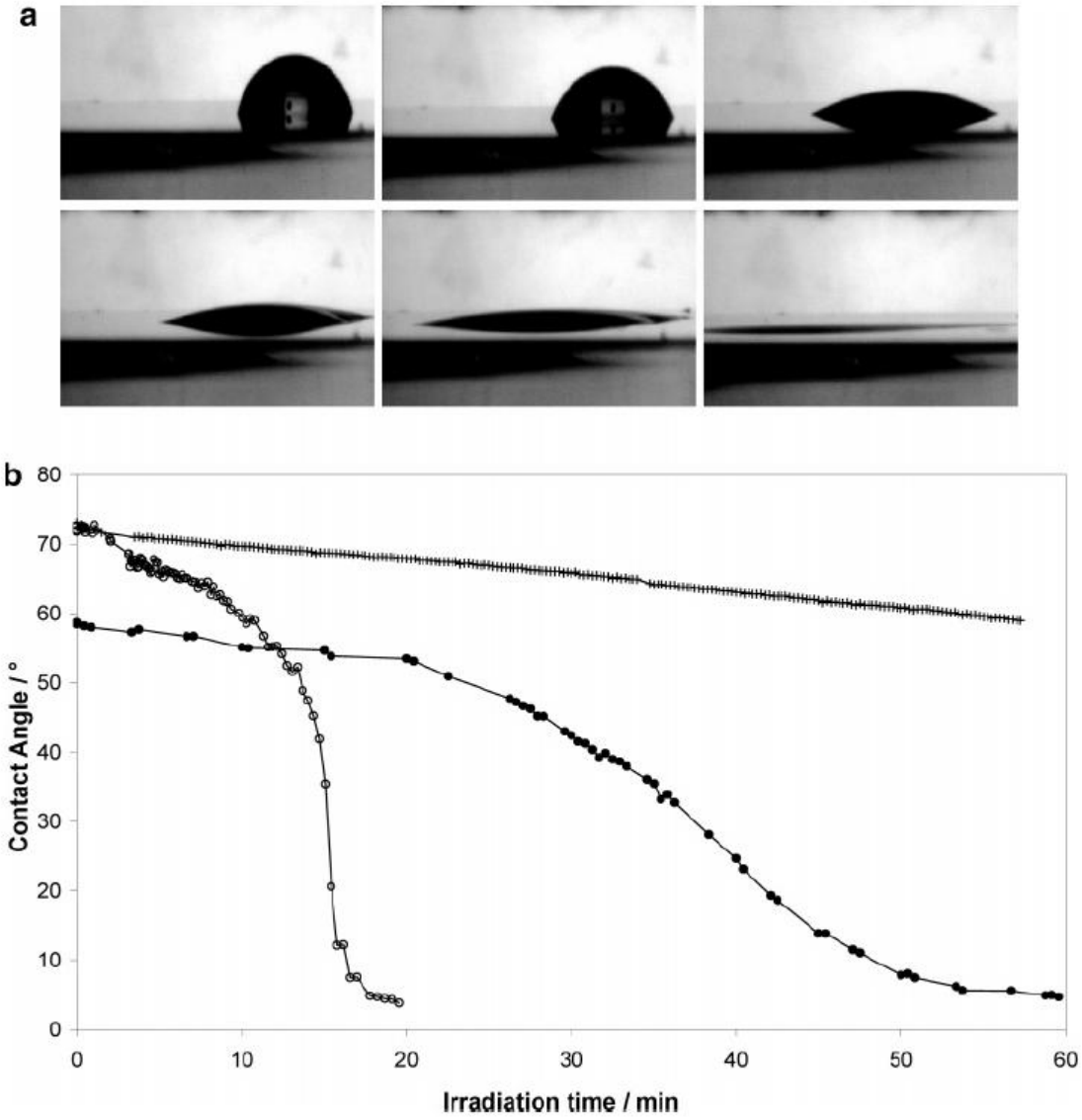

Figure 1-4. a) CCTV images of water droplets on Activ taken in situ during UV irradiation. $CA_{initial}$ = 69°, CA_{final} = ~0°. (b) CA versus irradiation time profiles recorded using Activ sample irradiated from above in water-saturated oxygen atmosphere and either UVC (○) or UVA (●) light, or in a water-saturated N_2-only atmosphere with UVC light (+). Adapted with permission from ref 22. Copyright 2007 American Chemical Society.

When these photoresponsive molecules are engineered to couple their light activated motion coherently within a host matrix or on the surface of a substrate they can provide reliable mechanical devices such as a nanoscale motors.[23, 24] One very versatile photomechanical molecule is azobenzene due to its clean and efficient photochemistry, strong absorption properties, and reliability. Azo (— N=N—) containing compounds are well known for their ability to isomerize from a thermodynamically favored *trans* configuration to a less stable *cis* configuration upon absorption of a photon in the UV and/or visible portions of the spectrum. Shown in Figure 1-5 is the photoisomerization motion of an azobenzene molecule. The reverse photoisomerization of the azo containing compound (*cis* → *trans*) is dictated by ring-substitution and/or the surrounding environment with lifetimes as short as a few seconds to as long as 6 years when bulky substituent groups are added in conjunction with a surrounding solid matrix.[5,25] A unique example of a photoresponsive smart material containing azobenzene ligands was reported

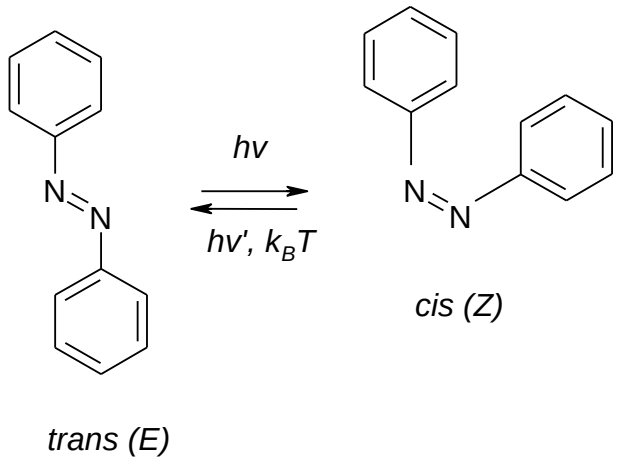

Figure 1-5. Photoisomerization of azobenzene. Azobenzene normally exists in the thermodynamically favored *trans* configuration. Upon absorption of a photon, by the *trans* absorption band, the molecule isomerizes to the less stable *cis* configuration. In the *cis* configuration, the molecule will relax back to the *trans* configuration with time or by heat and/or absorption of a photon in the *cis* absorption band.[5]

by Liu, *et al.* where they incorporated azobenzene ligands into the pore walls of a sol-gel synthesized mesoporous silica host, Figure 1-6.[26, 27] Upon irradiation with 365 nm light, the azobenzene ligands (predominately in the trans state) bend into the cis state, thus creating more space in the core of the pore with a estimated change in pore size of 6.8 Å.[26] Furthermore, mass transport studies were conducted with a membrane composed of this material where passage of probing molecules, of different sizes (269 $Å^3$ and 392 $Å^3$), were selectively controlled through the pore channels by alternating the channel size through the isomerization of the azobenzene ligands via UV irradiation.[27] Photoresponsive molecules are ideal candidates for smart materials given their robustness, energy efficiency, and versatility for incorporation into host matrices of varying forms making their potential unlimited for many modern and future applications.

Electroconductive Fibers

Electrically conductive fibers are another class of smart materials that have attracted significant awareness based on their ability to provide the following inherent properties: 1) conduct electricity; 2) high flexibility and light weight (as compared to metal wire); 3) electrostatic discharge; and 4) high frequency shielding.[28] Electroconductive fibers have been utilized in numerous applications including tethers for spacecraft and electrotextiles as wearable electronics for purposes of supporting military, security, and solar cell devices.[29, 30] In particular conductive fibers have been integrated into "Intelligent" systems such as wearable electronics for the ability to perform as sensors, actuators, and distributors of electrical current for support of higher end (*i.e.* intelligent materials) functions such as data processing and wireless communication.[28, 29] For example, in a review written by Coyle, *el at.* they described several

types of garments composed of conductive fibers utilized as piezoresistive sensors able to detect pressure changes induced by the wearer during physical movements induced by sports related

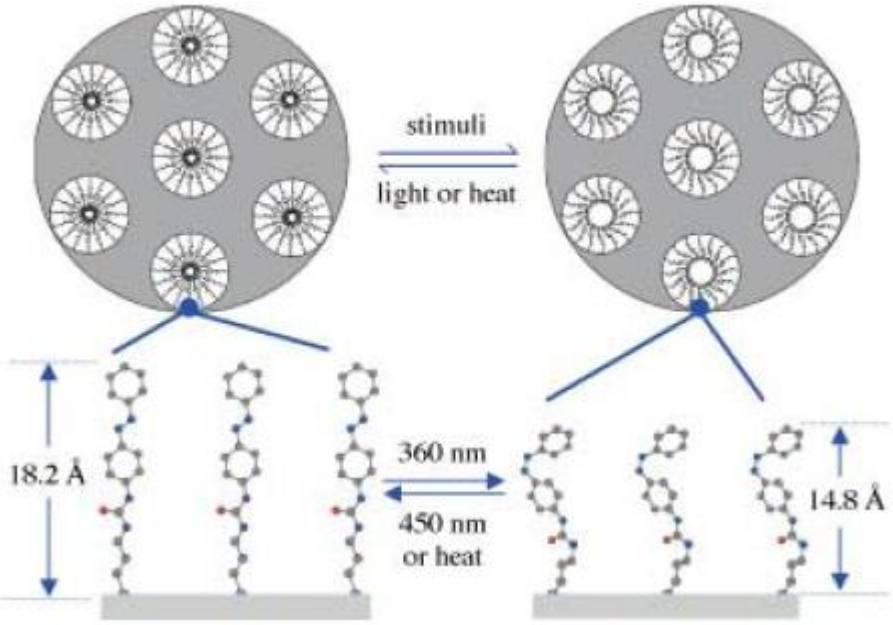

Figure 1-6. Photoresponsive nanocomposites prepared by Evaporation Induced Self Assembly (EISA). Atom labels: C: grey, O: red, N: dark blue, Si: blue, H atoms omitted. Adapted with permission from ref 26. Copyright 2003 Wiley-VCH Verlag GmbH & Co. KGaA.

activities (running, jumping, etc).[31] Also, some of these electroconductive garments are sensitive enough to detect electrical currents associated with the functionality of vital organs (heart) within the human body. The ability to provide continuous analysis of such vital processes within the human body can offer invaluable data for the understanding and treatment of post-operative patients. Conductive fibers come in many different forms such as metal wires, polymer fibers with imbedded conductive particles (metals, carbon, etc), surface metalized polymer fibers via chemical deposition (electroless and electrochemical), and inherently conductive polymers (ICP), *e.g.* polyacetylene, polypyrrole, polyaniline, and polythiophene.[29, 31-34] An example of a conductive fiber synthesized in our lab is shown in Figure 1-6. This particular fiber (Kevlar) was

coated (electroless) with a Ni layer before electrochemically depositing the final Au layer. The image shows well coated monofilaments with average conductivity values of 4.6 Scm^{-1} that exhibit only a 27% decrease in tensile strength after plating.[35] In addition, these high strength conductive fibers reached power output values as high as 9 W.

Unfortunately, drawbacks are inherent to some of the aforementioned types of electroconductive fibers, which eliminates their use for certain applications like wearable electronics. For example, metal wires are uncomfortable to wear, brittle, and lack the necessary flexibility for more active body movements.

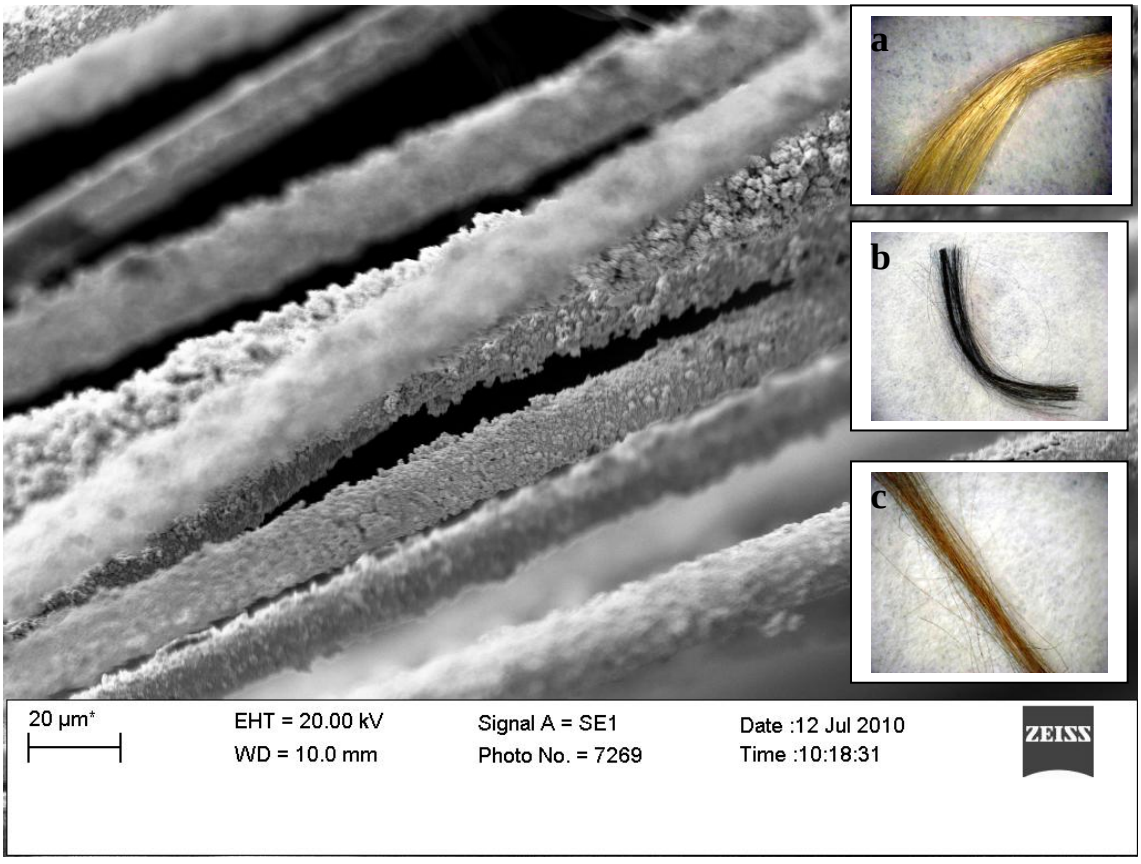

Figure 1-7. SEM image of kevlar monofilaments coated with Au (electrochemically). Inset: a) image of kevlar yarn before metallization steps; b) image of kevlar yarn after Ni deposition (electroless); and c) image of kevlar yarn after Au deposition (electrochemically).[35]

Also, ICPs and conductive fibers -via inclusion of conductive particles, do not fare well once laundered showing severe increases in resistivity.[36] Nevertheless, these fibers are able to conduct electricity and sense changes in their environment via piezoresistance and are ideal smart materials for inclusion into future intelligent systems (especially textiles) capable of sensing, actuating and processing information in response to an every changing external environment *i.e.* autonomous adaptation.

Conclusions

Since the discovery of stone over 2 million years ago, mankind has passionately pursued the development of such materials into tools in efforts to improve their every day lives. In the late 19th century, synthetic materials were discovered which possessed remarkable properties that could be applied to multiple areas of industry and technology. However, understanding how to combine the above mentioned materials into tools possessing multifunctional properties with responsive characteristics had not been realized. At present, existing smart materials posses unique structural properties (porosity, elasticity) and functions (actuator and/or sensor), but do not have the capability to operate autonomously within their environment, requiring direction (control) from an external source. Continued progress towards the evolution of smart materials into intelligent materials will require a greater understanding of biological systems at the molecular level with respect to their structural design and functional behavior. Knowledge gain from the aforementioned activities in conjunction with improvements in nanoengineering, renewable energy sources, and effective communication of scientific information will ultimately position scientist to make discoveries towards next generation materials that will propel mankind into the next era in the material age.

References

(1) Gandhi, M. V.; Thompson, B. S. *Smart Materials and Structures;* Chapman and Hall: London, 1992.

(2) Schwartz, M. *Encyclopedia of Smart Materials;* John Wiley and Sons: New York, NY, 2002. Vol. 1.

(3) Shakeri, C.; Noori, M. N.; Hou, Z. *Smart Materials and Structures a Review.* Materials for the New Millennium, Proceedings of the Material Engineering Conference, 4th, Washington D. C., Nov. 10-14, 1996, 2, 863.

(4) Yoshida, M.; Lahann, J. ACS Nano **2008**, 2, 1101-1107.

(5) Shahinpoor, M.; Schneider, H. *Intelligent Materials;* Royal Society of Chemistry: Cambridge, 2008.

(6) Kornbluh, R. *et al. Electroactive polymer (EAP) Actuators as Artificial Muscles: Reality, Potential and Challenges;* SPIE Press: Bellingham, 2004.

(7) Kumar, A.; Srivastava, A.; Galaev, T.; Mattiasson, B. *Prog. Polym. Sci.* **2007**, 32, 1205-1237.

(8) Zhang, H.; Han, J.; Yang, B. *Adv. Funct. Mater.* **2010**, 20, 1533-1550.

(9) Corriu, R.; Mehdi, A.; Reyé, C. *J. Organomet. Chem.* **2004**, 689, 4437-4450.

(10) Varadan, V. K. *Proc. SPIE* **2001**, 4591, 28-38.

(11) Garg, D.; Zikry, M.; Anderson, G.; *Smart Mater. Struct.* **2001**, 10, 610-623.

(12) Zielecka, M.; Bujnowska, E. *Prog. Org. Coat.* **2006**, 55, 160-167.

(13) Saito, H.; Takai, K.; Takazawa, H.; Yamauchi, G. *Mater. Sci. Res. Int.* **1997**, 3, 216-219.

(14) Lazar, M. A.; Tadvani, J. K.; Tung, W. S.; Lopez, L.; Daoud, N. A. *Innovations in thin Film Processing and Characterization* (ITFPC 2009). IOP Conference Series: Materials Science and Engineering 2010, 12, 1.

(15) Wong, C. P.; Xu, J.; Zhu, L.; Li, Y.; Sun, Y.; Lu, J. ; Dong, H. Proceedings of the IEEE CPMT Conference on High Density Microsystem Design, Packaging, and Failure Analysis, 7th, Shanghai, China, June 27 – 30, 2005, 149.

(16) Barthlott, W.; Ehler, N.; Raster- Eletronenmikroskopie der Epidermis- Oberflachen von Spermatophyten. Tropische und Subtropishe pflanzenwelt **1977**, 19, 1-110.

(17) Crick, R. C.; Parkin, I. P. *Chem. Eur. J.* **2010**, 16, 3568-3588.

(18) Xia, F.; Jiang, L. *Adv. Mater.* **2008**, 20, 2842-2858.

(19) Lim, H. S.; Kwak, D.; Lee, D. Y.; Lee, S. G.; Choi, K. *J. Am. Chem. Soc.* **2007**, 129, 4128-4129.

(20) Parkin, I. P.; Palgrave, R. G. *J. Mater. Chem.* **2005**, 15, 1689-1695.

(21) Linsebigler, A. L.; Lu, G.; Yates, J. T. *Chem. Rev.* **1995**, 95, 735-758.

(22) Mills, A.; Crow, M. *J. Phys. Chem. C* **2007**, 111, 6009-6016.

(23) Kang, H.; Liu, H.; Phillips, J. A.; Cao, Z.; Kim, Y.; Chen, Y.; Yang, Z.; Li, J.; Tan, W. *Nano Lett.* **2009**, 9, 2690-2696.

(24) Amabilino, D. B. *Chirality at the Nanoscale: Nanoparticles, Surfaces, Materials and more;* Wiley-VCH: Weinheim, 2009.

(25) Nagamani, S. A.; Nirikane, Y.; Tamaoki, N. *J. Org. Chem.* **2005**, 70, 9304-9313.

(26) Liu, N. ; Chen, Z. ; Dunphy, D. ; Jiang, Y. ; Assink, R.; Brinker, C. *Angew. Chem., Int. Ed.* **2003**, 42, 1731-1734.

(27) Liu, N.; Dunphy, D. R.; Atanassov, P.; Bunge, S. D.; Chen, Z.; Lopez, G. P.; Boyle, T. J.; Brinker, C. J. *Nano Lett.* **2004**, 4, 551-554.

(28) Tao, X. *Wearable Electronics and Photonics;* Woodhead publishing Limited: Cambridge, U. K., 2005.

(29) Westbrook, P.; Priniotakis, G. *Intelligent/smart materials and textiles: an overview;* Woodhead publishing Limited: Cambridge, U. K., 2005.

(30) Lorenzini, E.; Sanmartin, J. Electrodynamic Tethers in Space; *Scientific American* August **2004**, 50-57.

(31) Coyle, S.; Wu, Y.; Lau, K.; Rossi, D. D. ; Wallace, G. ; Diamond, D. D. *Smart Nanotextiles : A Review of Materials and Applications ;* MRS Bulletin, 2007, 32, 434.

(32) Mallory, G. O.; Hajdu, J. B., Eds.; *Electroless Plating*; AESF: Orlando, 1990.

(33) Vaia, R. A.; lee, J. W.; Wang, C.S.; Click, B.; Price, G. *Chem. Mater.* **1998**, 10, 2030-2032.

(34) Dong, H.; Fey, E.; Gandelman, A.; Jones, W. E. *Chem. Mater.* **2006**, 18, 2008-2011.

(35) Little, B.; Li, Y.; Cammarata, G.; Mills, G. *ACS Appl. Mater. Interfaces*, preparing for submission.

(36) Liu, X.: Chang, H.; Huck, W.; Zheng, Z. *ACS Appl. Mater. Interfaces* **2010**, 2, 529-535.

II. INVESTIGATION OF REACTIVE PEROXIDES IN SULPHONATED POLY(ETHER ETHERKETONE)/POLY(VINYL ALCOHOL) AQUEOUS POLYMER SOLUTIONS

Introduction

Photosensitive polymers are macromolecular materials that can utilize electromagnetic radiation as a source of energy for a variety of transformations. These materials were initially studied due to their ability to photoinitiate polymerizations,[1] but they can also serve as key components in holographic systems.[2] Numerous investigations have focused on photochromic polymers able to experience reversible property modifications when exposed to light including switching behavior,[3] structural alterations,[4] and conformational changes.[5] Polymers that exhibit light-induced reversible color changes are also known.[6,7] A different photosensitive macromolecular system is based on blends of poly(vinyl alcohol), PVA, and sulfonated poly(ether ether ketone), SPEEK.[8] Photolysis of the blends with 350 nm photons yields α-hydroxy radicals from SPEEK; optical and EPR data have confirmed the identity of the photoproducts. These observations can be rationalized on the basis of the known photochemistry of benzophenone (BP) molecules.[9] Illumination of BP produces a triplet (n, π*) excited state able to abstract an H-atom from alcohols, forming a α-hydroxy radical of BP (known as a benzophenyl ketyl (BPK) radical). The α-hydroxy radical of the alcohol that is simultaneously formed can reduce another BP molecule generating a second BPK radical. Thus, absorption of one photon can yield up to two BPK radicals in solutions of BP.

A similar process explains the radical formation in the polymer system where BP groups of SPEEK act as sensitizers whereas PVA functions as the H-atom donor. The overall photochemical process in SPEEK/PVA blends is summarized by the reaction:

$$2\{R'RC=O\}_z + h\nu + \{CH_2CHOH\}_y \rightarrow 2\{R'RC\bullet OH\}_z + \{CH_2C=O\}_y \quad (2\text{-}1)$$

where $\{R'RC=O\}_z$ represents SPEEK, $\{CH_2CHOH\}_y$ corresponds to PVA, $\{R'RC\bullet OH\}_z$ corresponds to the α-hydroxy radical of SPEEK and $\{CH_2C=O\}_y$ represents an oxidized PVA molecule. Since both SPEEK and PVA are water soluble, casting methods together with crosslinking procedures made possible the preparation of optically transparent films of the blends. Thus, both aqueous solutions and thin films can serve as matrices to study reactions of photogenerated SPEEK radicals. These radicals are strong reducing agents in solution with an estimated oxidation potential of about ¯1.3 V.[8b] Indeed, BPK radicals of SPEEK are able to reduce a variety of metal ions forming nanometer-sized metallic particles in both liquid and solid matrices.[8] Polymeric BPK radicals decay in air-free solutions via second-order recombination step with a rate constant of 290 M^{-1} s^{-1}, resulting in long lifetimes of about 30-40 min.[8b] In contrast, analogous α-hydroxy radicals of PVA decay with rate constants of 1-7 x 10^9 M^{-1} s^{-1} in water.[10] Electrostatic repulsions between the negatively charged SPEEK chains hinder reactive collisions between the polymeric radicals, increasing their lifetime. Another contributing factor is the slow radical diffusion in SPEEK/PVA solutions because their high PVA concentrations results in a four fold viscosity increase as compared with that of water.

SPEEK radicals exhibit lifetimes of several hours when photogenerated inside films free of O_2 and persist for about 30 min when formed under air.[8a] Reaction of typical α-hydroxy radicals (such as $(CH_3)_2C\bullet OH$) with oxygen in water is essentially diffusion controlled with k = 4 x 10^9 M^{-1} s^{-1}.[11] In contrast, SPEEK radicals react with oxygen in films with an apparent first-order rate constant of k_2 = 1 x 10^{-3} s^{-1} probably due to the low O_2 mobility in PVA,[12] which is the solvent

in the solid matrices. Scavenging of SPEEK radicals by oxygen in the polymer films has been represented by:[8a]

$$\{R'RC\bullet OH\}_z + O_2 \rightarrow \{R'RC(OH)OO\bullet\}_z \qquad (2\text{-}2)$$

which results in an organic peroxyl radical. The proposed formation of peroxyl radicals seems logical given that reaction of PVA radicals with O_2 in solution yields analogous radical intermediates that subsequently decay via elimination of $HO_2\bullet/\bullet O_2^-$.[13] Both of the latter radicals form H_2O_2 through disproportionation reactions.[14]

Hence, photolysis of SPEEK/PVA films and solutions in the presence of O_2 is expected to yield H_2O_2. Support for such expectation is provided by earlier studies that reported generation of the peroxide by illumination of air-saturated aqueous solutions containing BP or derivatives of the ketone.[15-17] Reduction of chemicals adsorbed on the surface of films by SPEEK radicals, in competition with the H_2O_2 formation process, seemed possible given the long lifetime of the radicals when photogenerated in the solid matrices under air. Strongly reducing radicals are known to initiate transformations of halocarbons.[18] Complete degradation of these materials occurs in systems were the radicals are formed in the presence of H_2O_2, suggesting a synergistic action of both reactive chemicals.[19] This means that adsorption of chemicals on SPEEK/PVA films would render them susceptible to degradation initiated via a combined attack of polymer radicals and peroxide molecules.

Considerable interest exists presently in protective clothing that chemically inactivate toxic compounds and pathogens.[20] An example of such materials are “self-cleaning fabrics” containing enzymes able to degrade organophosphorus compounds.[21] A relevant fact is that

recent investigations demonstrated that methods based on H_2O_2 are highly effective for the decontamination of several chemical warfare agents.[22] Also, polymer films containing chemically bonded BP molecules have been reported to exhibit antibacterial properties under illumination.[23] Qualitative tests indicated that BPK radicals and H_2O_2 were generated during photolysis and the bactericidal activity was correlated to these reactive species. Thus, films of SPEEK/PVA seem to exhibit properties relevant for the realization of "self-cleaning surfaces", in which the photogenerated reactive radicals and peroxide would act as agents for the degradation of undesired materials present on the solid surface.

Reported here are kinetic data pertaining to the H_2O_2 formation in illuminated aqueous solutions containing SPEEK and PVA. Such studies were preferred since methods for the quantification of $[H_2O_2]$ in solution are well established, and also because liquid phase reactions are less constrained by diffusion restrictions that exist in the solid state. In fact, mechanistic knowledge gained in solution investigations was considered crucial to understand the H_2O_2 photogeneration in polymer films that is currently being explored. The kinetics of H_2O_2 formation data is controlled by the photochemical excitation of the polymeric BP groups, not by the chemistry of the radical intermediates.

Experimental

Poly(vinyl alcohol), 99+% hydrolyzed with an average molar mass of 8.9-9.8 x 10^4 g/mol as well as ammonium molybdate (VI) tetrahydrate were obtained from Aldrich. Poly(ether etherketone) (PEEK) with an average molar mass of 4.5 x 10^4 g/mol was a gift from Victrex, Inc and served as a precursor of SPEEK. Hydrogen peroxide (30% v/v) was acquired from Fisher Scientific and potassium hydrogen phthalate was from Matheson Coleman and Bell. All

solutions were prepared with purified water obtained through an ion-exchange resin deionizer (US filter service). Preparation of SPEEK as well as of solutions containing this polymer and PVA followed the procedures described in previous studies.[8]

Illuminations used modified Milton Roy # 33-17-80 optical test tubes able to withstand the low temperatures (77 K) of the degassing processes.[6,8] Unless otherwise stated, the optical tubes containing air-saturated solutions were sealed with rubber septa for photolysis experiments. Gas-tight syringes from Hamilton enabled extraction of samples from photolyzed solutions. A freeze-pump-thaw method was utilized to eliminate oxygen from SPEEK/PVA solutions. The vessels were back-filled with Ar to maintain a pressure of one atmosphere. Optical data was collected on a Shimadzu UV-Vis 2501PC spectrophotometer. Photolysis experiments were carried out inside a Rayonet 100 circular illuminator that generated photons with $\lambda = 350 \pm 15$ nm by means of 16 RPR-3500A lamps; the light intensity (I_0) was determined using the Aberchrome 540 actinometer.[24] Uniform illumination of the optical tubes was achieved by positioning them at the center and mid-height of the cavity inside the Rayonet, where the temperature was constant at 29 °C. All other measurements were conducted at room temperature and each photochemical experiment was performed at least twice. Determinations of $[H^+]$ employed a Radiometer PHM95 pH/ion meter in conjunction with an Accumet pH electrode.

Oxygen consumption was followed using a Hansatech Oxygraph instrument equipped with a S1 Electrode Disc (Clark polarographic sensor). For these experiments the vessel containing the polarographic sensor was filled with SPEEK/PVA solutions immediately after their illumination inside the Rayonet. The top of this vessel was covered but not closed completely because sealing this container with a septum increases the internal air pressure, which augments the amount of O_2 dissolved in solution. Since the vessel was not sealed, the lowest

oxygen reading was taken to be the O_2 concentration present in the solution. Calibrations were conducted using non-illuminated SPEEK/PVA samples. Detection of hydrogen peroxide was conducted via the molybdenum-triiodide method using an extinction coefficient of $\varepsilon = 2.64 \times 10^4$ M^{-1} cm^{-1}.[25] This procedure employs a solution containing 0.398 M KI, 1.7×10^{-4} M ammonium molybdate, and 0.06 M NaOH together with another consisting of 0.098 M potassium biphthalate. Equal amounts of the two solutions were mixed under stirring inside 1 cm quartz optical cells, followed by addition of a small aliquot of photolyzed sample and deionized water to yield a total volume of 3 mL. This method enabled to carry out kinetic runs using low volumes of SPEEK/PVA solutions. Quantifications of $[H_2O_2]$ via the I_3^- procedure exhibited a typical error of 10% in water but deviations of 30% were observed in SPEEK/PVA solutions.

Results and Discussion

Exposure to 350 nm photons of air-saturated solutions containing 0.36 M PVA and 0.018 M SPEEK (both molarities are expressed in terms of the monomer units) yielded no color change of the liquids. This contrasts with the results obtained with degassed solutions, where an optical signal centered at λ_{max} = 565 nm corresponding to the SPEEK radical (or SPEEK•) is promptly detected.[8] Analysis of the photolyzed solutions for H_2O_2 using the method described above yielded yellow solutions due to the formation of I_3^- ions. Shown in Figure 2-1 are optical spectra resulting from exposure of illuminated solutions to the iodide-molybdate reagent. An absorbance centered at λ_{max} = 370 nm is observed that increases in intensity as illumination progresses. This signal is shifted to longer wavelengths as compared with the absorption of I_3^- in water that exhibits a maximum at 350 nm.[25] However, red-shifts of the triiodide spectrum and decreases in the ε value occur when alcohols are added to aqueous solutions of I_3^-.[26]

Consequently, the shift in the λ_{max} value depicted in Figure 2-1 can be understood considering the very large [PVA] present in the polymer solutions. The data of Figure 1 clearly demonstrates that peroxide is formed upon photolysis of SPEEK/PVA solutions containing air. Repeated attempts to determine the extinction coefficient of I_3^- in the polymer solutions yielded results equal to or lower by 20% than the well known value in water, $\varepsilon = 2.64 \times 10^4\ M^{-1}\ cm^{-1}$.[25] Given such erratic results all calculations of $[H_2O_2]$ in polymer solutions used the ε value obtained in H_2O. This method underestimated the efficiency of the photoreaction, meaning that the reported quantum yields of H_2O_2 generation represent lower limits.

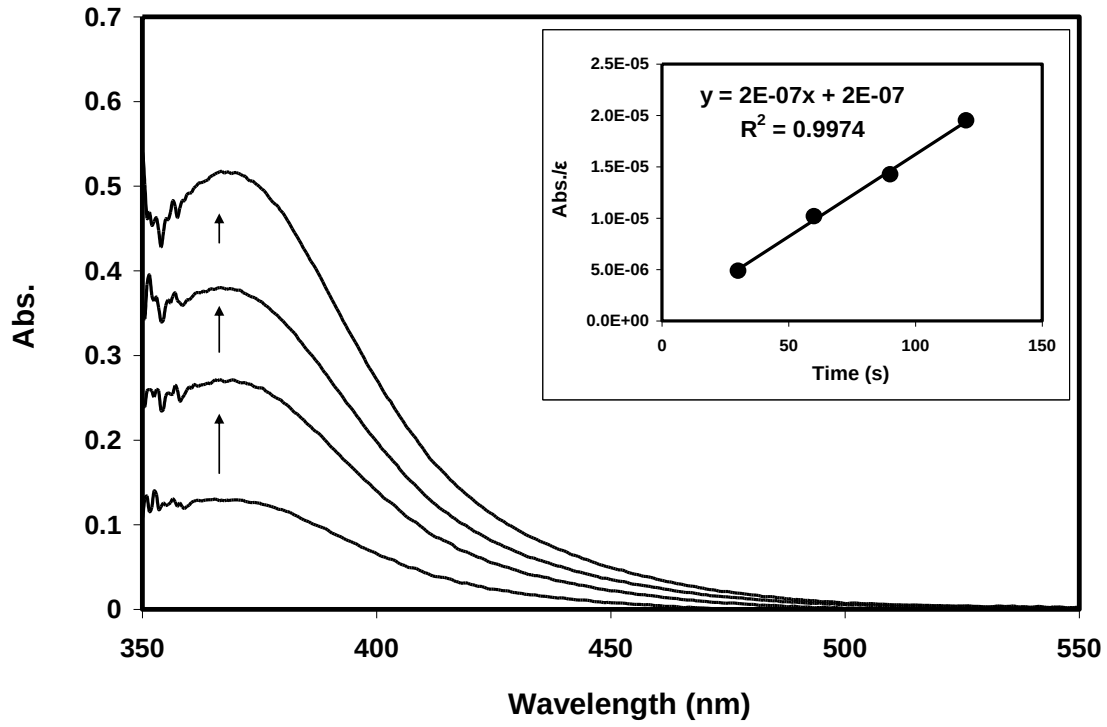

Figure 2-1. Optical spectra obtained after analysis with the iodide-molybdate method on air-saturated solutions at pH 7 containing 0.018 M SPEEK and 0.36 M PVA photolyzed in a closed vessel. Bottom to top: samples irradiated with 350 nm light, $I_0 = 4.9 \times 10^{-5}$ M(hν)/s, for 30 s, 60 s, 90 s and 120 s. Inset: plot of absorbance at 370 nm divided by ε as a function of irradiation time.

As shown in the inset of Figure 2-1 the absorbance at 370 nm varies in a linear fashion for short illumination times. While H_2O_2 reacts fast with I^-, organic peroxides oxidize iodide much slower resulting in a delayed formation of I_3^-.[25] No slow formation of the optical signal from I_3^- was noticed, meaning that stable organic peroxide species are not produced upon illumination of SPEEK/PVA solutions. This, in turn, implies that H_2O_2 is formed quickly after the decay of the peroxyl radical resulting from reaction 2-2.

Experiments were performed in order to establish the relationship between the rates of H_2O_2 formation and of O_2 consumed. For this purpose, an aliquot of the photolyzed sample was immediately analyzed for $[O_2]$ and the peroxide concentration was determined simultaneously. Results of these measurements are shown in Figure 2-2. According to the polarographic results

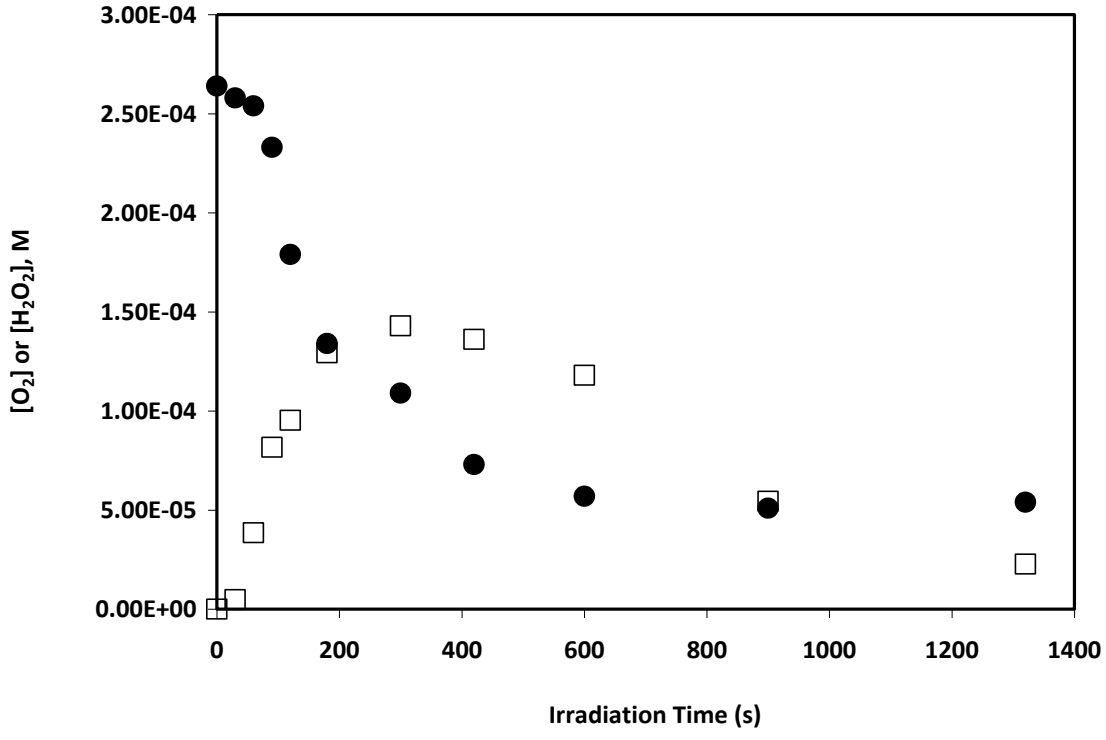

Figure 2-2. Plot of the concentrations of O_2 (●) and H_2O_2 (□) as a function of irradiation time. The aqueous air-saturated solutions containing 0.36 M PVA and 0.018 M SPEEK at pH 7 were illuminated in an open vessel with 350 nm light, $I_0 = 1.6 \times 10^{-5}$ M(hν)/s.

the saturation concentration of O_2 in neutral SPEEK/PVA solutions is 0.27 mM, close to the value obtained in water. Formation of peroxide occurs with an initial rate of $r_i = 2.7 \times 10^{-7}$ M/s whereas the r_i value for O_2 consumption amounts to 2×10^{-7} M/s. In addition both $[H_2O_2]$ and $[O_2]$ reach a value close to one half of the initial oxygen concentration at about 190 s of photolysis. The results indicate that O_2 reduction and H_2O_2 formation take place in a synchronous fashion and confirm that no stable organic peroxides are formed as intermediates. After 200 s the rates of both processes decrease and a maximum in $[H_2O_2]$ is reached at about 300 s, after which consumption of peroxide takes place. These findings clearly indicate that reduction of the peroxide by SPEEK• starts competing with reaction 2-2 once $[H_2O_2]$ becomes close to $[O_2]$.

The data shown in Figure 2-2 seems to indicate that a slight delay of about 70 s occurs during the decay of $[O_2]$. This phenomenon originates because of the low sensitivity of the polarographic sensor to small $[O_2]$ changes and also because of oxygen diffusion into the vessel where the measurements take place. Small air leaks into the photolyzed solutions are inevitable given that the vessel was not sealed, which results in an artificial delay in the oxygen consumption. To confirm this interpretation an experiment was performed in which the polarographic vessel containing an SPEEK/PVA solution under air was placed inside the Rayonet and irradiated, the results are presented in Figure 2-3. Reduction of oxygen starts as soon as the light exposure is started and progresses initially in a linear fashion with time but the rate of O_2 decay decreases after about 2700 s. Also, an increase in $[O_2]$ occurs after photolysis is stopped, supporting the interpretation that the delay in oxygen reduction noticed in Figure 2-2 results from small air leaks. Shown in Figure 2-4 is the initial data collected when the polarographic cell containing an air-saturated SPEEK/PVA solution was place and irradiated

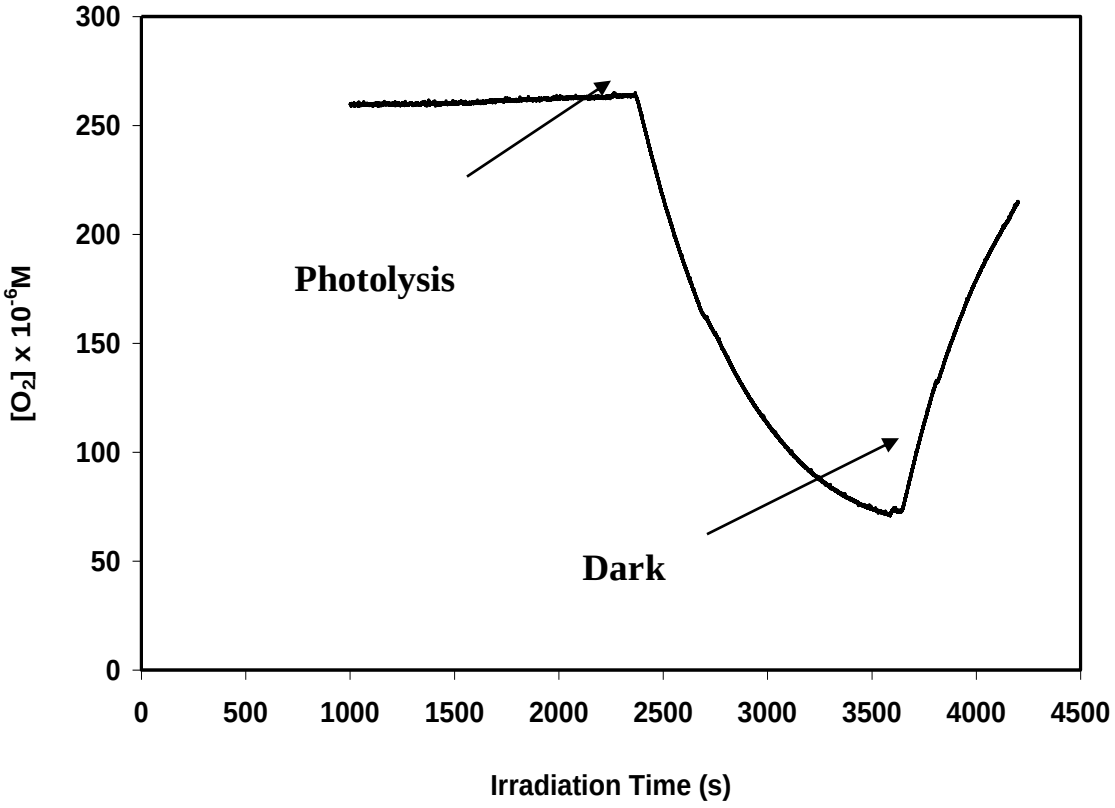

Figure 2-3. Evolution of $[O_2]$ during an experiment in which the polarographic cell containing 1 mL of an air-saturated solution with 0.018 M SPEEK and 0.36 M PVA at pH 7 was placed inside the Rayonet and irradiated continuously with 350 nm photons, $I_0 = 3.01 \times 10^{-5}$ M(hν)/s.

inside the illuminator. Under these conditions the initial rate of oxygen consumption amounts to 4×10^{-7} M/s and is twice the r_i value derived from the data of Figure 2-2 because a two times higher light intensity was used in the experiment of Figure 2-4. Depicted in Figure 2-5 are kinetic data collected at short times when air-saturated SPEEK/PVA solutions were exposed to different light intensities. In all cases $[H_2O_2]$ increased linearly with time with initial quantum yields of peroxide formation, $\phi_i(H_2O_2)$, ranging between 0.021 and 0.017. The fact that $\phi_i(H_2O_2)$ was fairly constant at all light intensities means that the rate of peroxide formation is first-order with respect to I_0. Benzophenone molecules are known to generate singlet oxygen $^1O_2$ via quenching of their triplet (n, π^*) excited state by triplet oxygen.[9] Therefore, experiments were

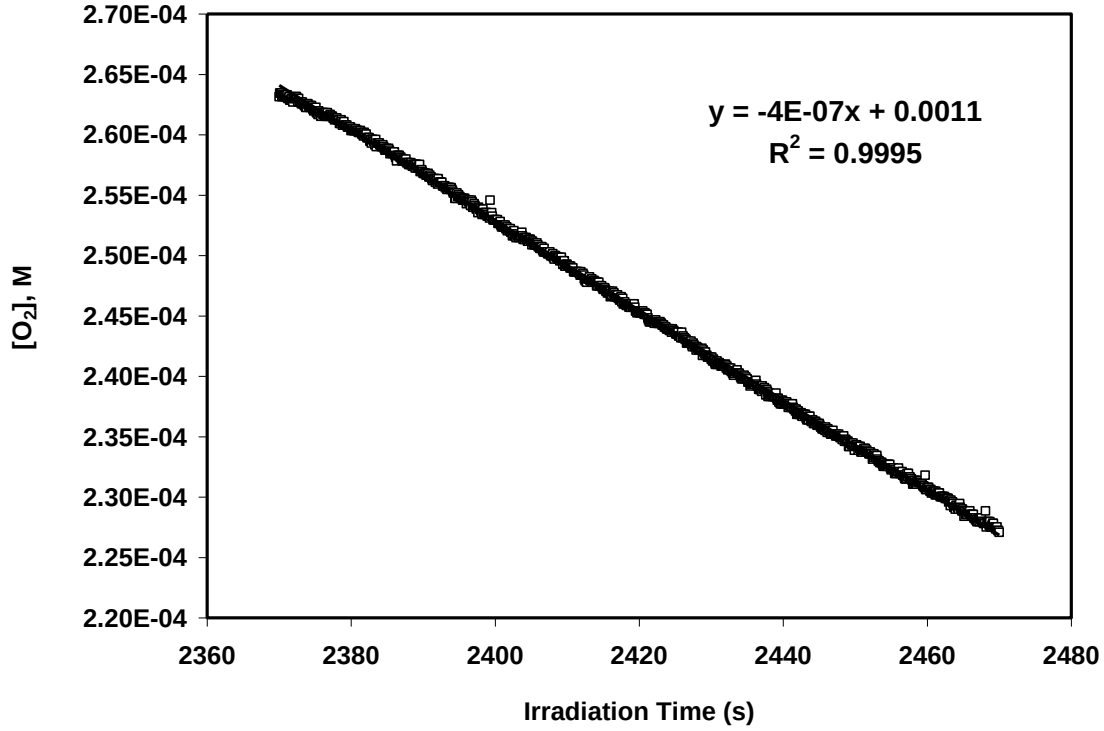

Figure 2-4. Initial decay of $[O_2]$ during the experiment in which the polarographic cell containing 1 mL of an air-saturated solution with 0.018 M SPEEK and 0.36 M PVA at pH 7 was placed inside the Rayonet and irradiated continuously with 350 nm photons, $I_0 = 3.01 \times 10^{-5}$ M(hν)/s.

performed to ascertain if the formation of H_2O_2 originated from chemical reactions initiated by $^1O_2$. A priori involvement of singlet oxygen in the photogeneration of H_2O_2 seemed unlikely given that water deactivates $^1O_2$ in a few μs via physical quenching.[27] Quantification of $[^1O_2]$ in aqueous solutions can be accomplished by a method based on the reaction of singlet oxygen with I^- to form triiodide ions.[28] The data of Figure 2-6 shows that $[^1O_2]$ increased linearly at short irradiation times for solutions containing 5.8×10^{-4} M SPEEK with and without PVA, but deviations from this behavior were noticed as the illumination progressed. Because of the low concentration of SPEEK employed in these experiments only half of the photon flux entering the optical cell was absorbed by the polyketone ($\varepsilon_{350} = 900\ M^{-1}\ cm^{-1}$).[8b] After correcting for the

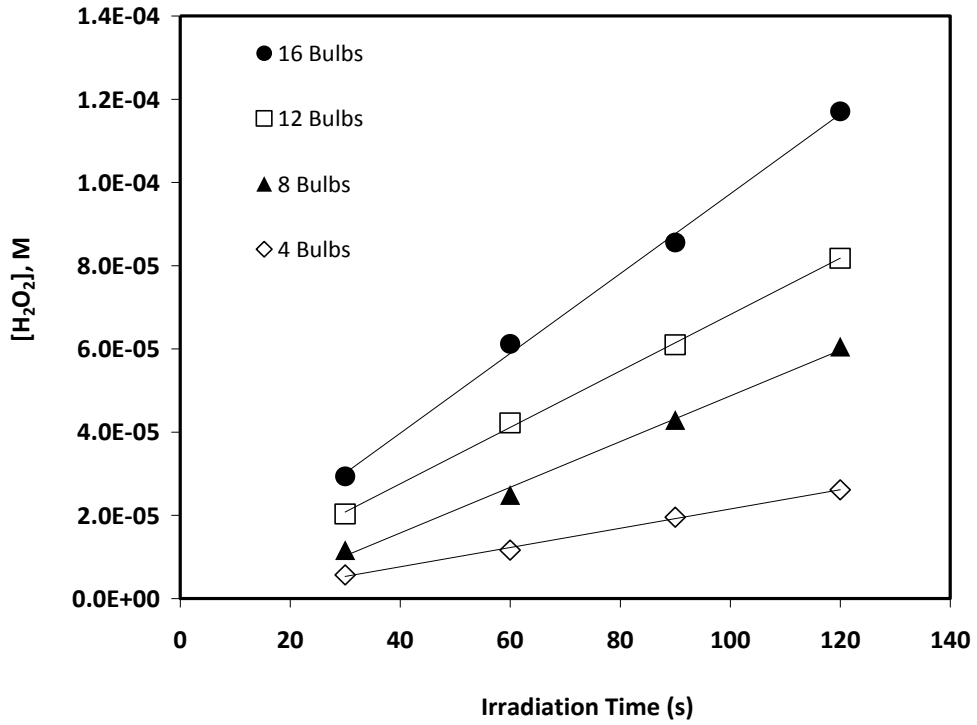

Figure 2-5. Plots of $[H_2O_2]$ versus irradiation time at different light intensities obtained from photolysis with 350 nm light of air-saturated solutions containing 0.018 M SPEEK and 0.36 M PVA at pH 7 in a closed system.

lower photon absorption by SPEEK, initial quantum yields for the $^1O_2$ formation of 5×10^{-4} and 1.1×10^{-3} result for the experiments with and without PVA, respectively. The presence of PVA decreases the efficiency of $^1O_2$ generation because the polyol competes with O_2 for the photogenerated triplet states of SPEEK, ^{3}{SPEEK}*. At any rate, the initial quantum yields of $^1O_2$ formation are 10 to 20 times lower than the $\phi_i(H_2O_2)$ values derived from Figure 2-5, indicating that singlet oxygen plays no significant role in the photoreduction of O_2.

Shown in Figure 2-7 is the evolution of $[H_2O_2]$ over longer periods of illumination. In all cases the solutions were not stirred in order to gain insight about the mechanism of peroxide formation under conditions that mimic somewhat the photochemical reactions taking place on

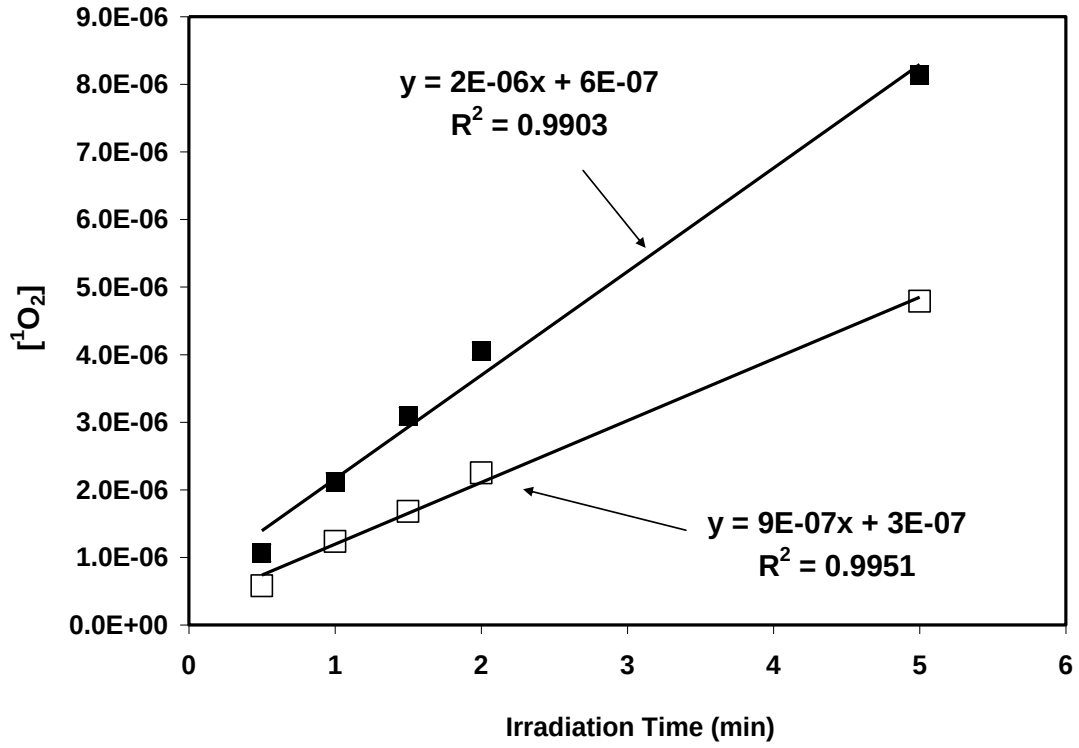

Figure 2-6. Evolution of $[^1O_2]$ with irradiation time measured for air-saturated solutions at pH 6 containing 0.398 M KI and 5.8 x 10^{-4} M SPEEK with 0.012 M PVA, λ_{max} = 362 nm (□) and without PVA, λ_{max} = 367 nm (■). Photolysis were performed on 1 cm optical cells using an intensity of 350 nm photons equal to 3.1 x 10^{-5} M(hν)/s.

film surfaces. A surprising observation is that the evolution of $[H_2O_2]$ as a function of time at constant I_0 is very similar for both solutions that are open to air and those that are not. The fact that the r_i values of peroxide formation are identical is not unexpected given that the initial oxygen concentrations are the same for both systems. In contrast to the observations, solutions exposed to air throughout the illumination were anticipated to display a maximum $[H_2O_2]$ different from that of closed systems. The assumption was that replenishment of consumed O_2 would be faster in solutions open to air than in closed systems. Also, the rate of peroxide consumption at longer exposure times measured in an open system (1.0 x 10^{-7} Ms^{-1}) is only 40% lower than the value obtained for closed solutions (1.7 x 10^{-7} Ms^{-1}). Continuous

exposure to air was anticipated to delay the consumption of peroxide significantly and to eventually yield a steady state concentration of oxygen where the rates of O_2 consumption and of

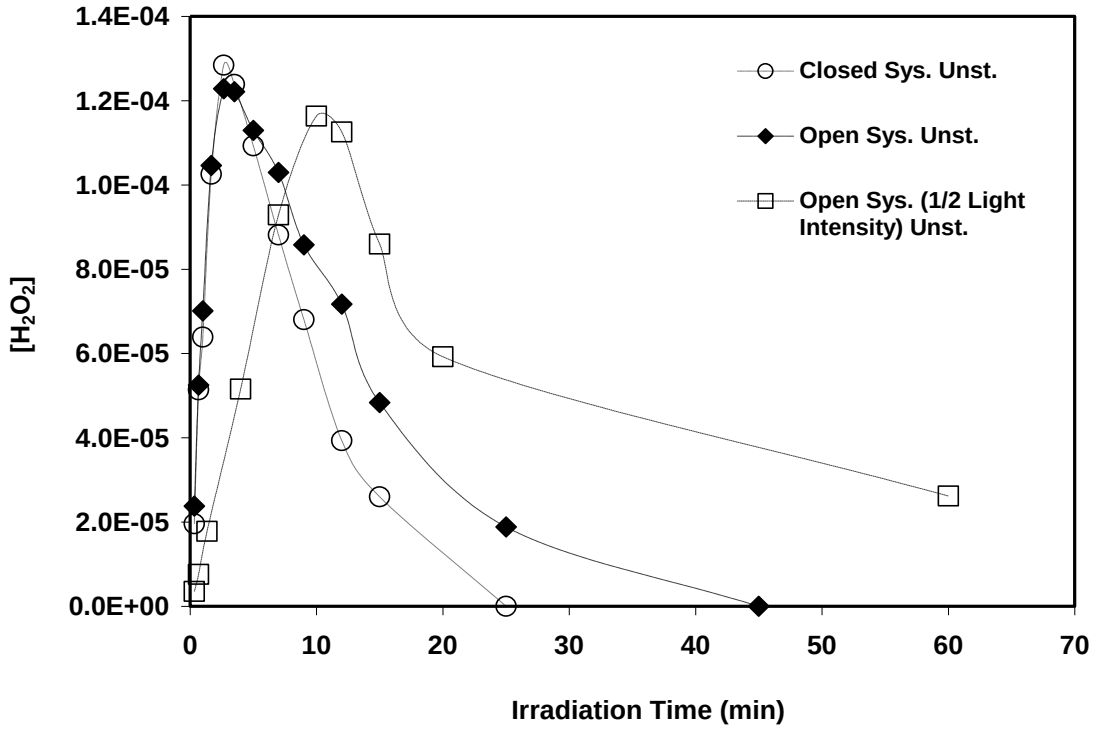

Figure 2-7. Plot of $[H_2O_2]$ versus irradiation time determined using air-saturated aqueous solutions in closed and opened vessels containing 0.018 M SPEEK and 0.36 M PVA at pH 7. Illumination with 350 nm photons in closed system unstirred (♦) and open system unstirred (⊖), $I_0 = 4.2 \times 10^{-5}$ M(hν)/s. Photolysis of an open system at one half the light unstirred (⊟) with $I_0 = 1.9 \times 10^{-5}$ M(hν)/s. Lines between data points are not fits, but are present as a guide.

gas diffusion into the solution would equal. Obviously, such situation was not possible in the case of closed systems. However, the data of Figure 2-7 indicates that diffusion of O_2 from the gas phase is unable to compete with the speed of the oxygen reduction process at high light intensities. This results in a complete consumption of H_2O_2 at long illumination times in both systems. Hence, once $[O_2]$ decreases substantially and the instantaneous radical concentration surpasses that of oxygen, any molecules of the gas diffusing into the solution are reduced fast to

H_2O_2 and the resulting H_2O_2 is also transformed promptly to water. Under those conditions light acts in a way similar to degassing the solutions, where oxygen is quickly reduced to H_2O before the gas can diffuse into the bulk of the liquid phase.

Support for this interpretation is provided by the kinetic data gathered from a solution open to air using half the light intensity. Under these conditions, not only is the initial rate of peroxide formation 83 % smaller (1.7×10^{-7} Ms^{-1}), but the maximum [H_2O_2] occurs at longer times and the decay of the peroxide is never complete within the illumination periods employed in these experiments. Although the proposed explanation is able to rationalize the findings presented in Figure 2-7, stirring the solutions during photolysis yields some surprising data. Namely, [H_2O_2] continued to increase up to 0.17 mM and then leveled off when solutions in open systems illumination were stirred using high light intensities. Photolysis under stirring of closed systems containing air, or of a stirred closed system but saturated with O_2 exhibited a continuous increase in peroxide concentration up to a value of 0.3 mM. However, the value of r_i was the same in all cases including the high intensity experiments of Figure 2-7.

The fact that r_i remains unchanged means that zero-order conditions prevail in all these experiments because at the beginning of the photoreactions [O_2] >> [SPEEK•] and the BPK radicals are generated at a constant rate. Given that under such conditions enough oxygen is available to scavenge all the photogenerated radicals, the rate of peroxide formation is controlled by the rate of SPEEK• formation and is unaffected by stirring. A higher maximum in [H_2O_2] occurs in open systems because agitating the solutions improves mass transfer. The larger maxima noticed in stirred but closed systems either saturated with air of with O_2 seems puzzling. However, measurements on the air pressure in tubes sealed with rubber septa yielded interesting results. One set of determinations consisted of equilibrating against atmospheric pressure the

plunger a gas-tight syringe pierced through the septa. In the other set the vessel containing the polarographic sensor was sealed with septa. Gas pressures ranging between 2 and 2.6 atm were

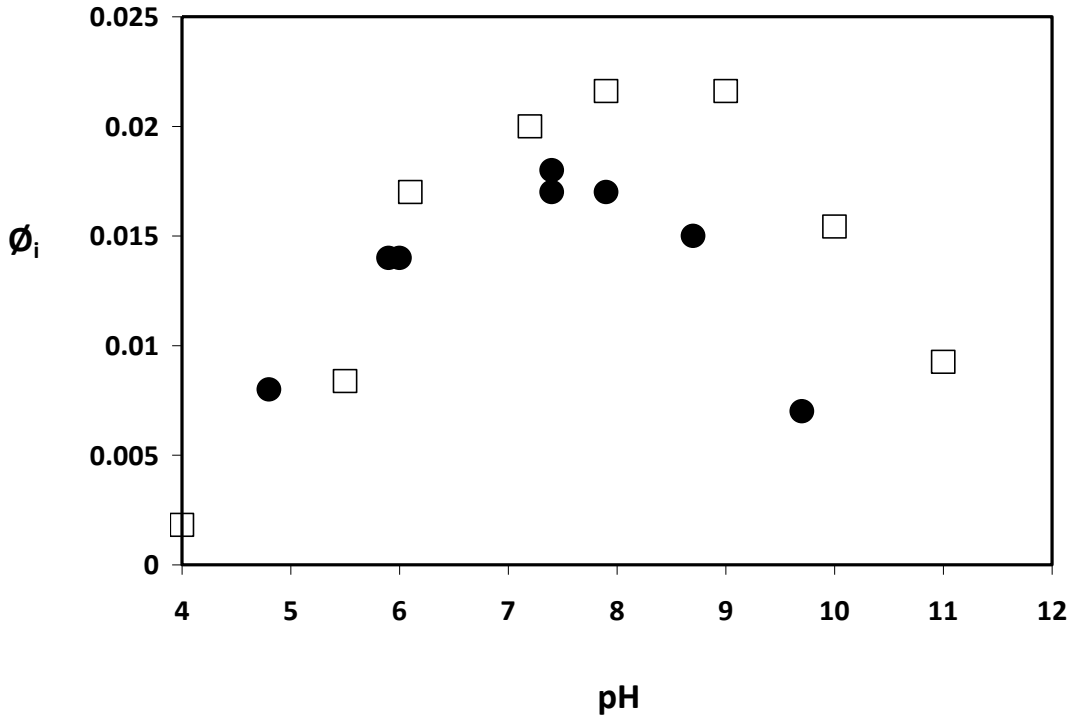

Figure 2-8. Dependence of $Ø_i(H_2O_2)$ (□) and $Ø_i$(SPEEK•) (●) on the solution pH. $Ø_i(H_2O_2)$ determinations were carried using air-saturated solutions containing 0.018 M SPEEK and 0.36 M PVA stirred in closed systems. $Ø_i$(SPEEK•) values were obtained from similar solutions that were degassed but not stirred. Photolysis with 350 nm light, $I_0 = 5.3 \times 10^{-5}$ M(hν)/s.

determined, meaning that $[O_2]$ similar to that of solutions saturated with oxygen were prevalent in closed systems containing air. The higher concentrations of oxygen present in the closed, air-saturated systems enabled O_2 to outcompete H_2O_2 for SPEEK•.

Illustrated in Figure 2-8 is the dependence of $\phi_i(H_2O_2)$ on solution pH showing that the O_2 photoreduction was most efficient between pH values of 8 and 9. Included in this figure are initial quantum yields for the formation of polymer radicals, ϕ_i(SPEEK•) that were obtained in

unstirred experiments to prevent as much as possible stirring-induced radical decay via dimerization/disproportionation.[8b] Photogeneration of SPEEK• was most efficient at pH = 7.3 and the resulting quantum yield agrees well with the value reported before (0.02) for neutral solutions. Formation of the radicals seemed less effective as $[H^+]$ or $[OH^-]$ increased. The lower efficiency of formation of the polymer radicals in acid solutions is not surprising given that the triplet excited state of BP is known to be quenched by H^+.[29] Thus, a similar quenching of ^{3}{SPEEK}* may explain the lower ϕ_i(SPEEK•) observed in acid solutions. On the other hand, the BPK radical of benzophenone deprotonates in basic solution with $pK_a = 9.2$ yielding a radical anion that exhibits an absorption maximum at 630 nm.[30] Dimerization of BP α-hydroxy radicals is fastest when both the neutral and the anion radicals combine. A similar process may take place in basic solutions of SPEEK/PVA given that at pH > 10 the optical signal of SPEEK• weakened and a new absorption centered at about 610 nm emerged. Fast combination between the SPEEK neutral and anion radicals may be the reason for the low ϕ_i(SPEEK•) values measured in basic solutions.

Analysis of the data shown in Figure 2-8 reveals that $\phi_i(H_2O_2) > \phi_i$(SPEEK•) in most cases, a result that seems impossible given that 2 SPEEK radicals are needed for the reduction of one O_2 molecule to form H_2O_2. However, as was indicated before,[8b] the ϕ_i(SPEEK•) values obtained during steady state experiments represent only lower limits of the true quantum yields of polymer radical formation due to the fact that these reactive species are decaying during such determinations. Of interest here is the fact that the quantum yield for the formation of SPEEK triplet states, $\phi(^3${SPEEK}*), amounts to 0.04. Considering that two SPEEK• are expected to form per every ^{3}{SPEEK}, then the maximum possible value for $\phi_i(H_2O_2)$ is 0.04, whereas the highest peroxide quantum yield reported in Figure 2-8 is close to 0.021. Consequently, only

about 50% of the photogenerated SPEEK radicals are reducing O_2. Support for this conclusion is provided by results from studies of SPEEK• reactions by Ag+ ions, which can scavenge about 80%

of the photogenerated polymer radicals.[8b]

Generation of H_2O_2 via free radicals usually involves $HO_2\bullet/\bullet O_2^-$ as intermediates and the formation process is controlled by the disproportionation of the peroxyl species.[14] The disproportionation involving one $HO_2\bullet$ and one $\bullet O_2$ is fastest and reaches a maximum rate at pH = 4.8, which is the pKa for $HO_2\bullet$. Inspection of Figure 2-8 reveals that $\phi_i(H_2O_2)$ reaches maximum values at pH > 4.9, meaning that the photogeneration of peroxide in SPEEK/PVA solutions is not governed by the reaction kinetics of the peroxyl radicals. This analysis supports the notion that the photochemical process that generates the SPEEK• radicals controls the rate of H_2O_2 formation. The following mechanism is consistent with the experimental results:

$$\{R'RC=O\}_z + h\nu + \{CH_2CHOH\}_y \rightarrow \{R'RC\bullet OH\}_z + \{CH_2C\bullet OH\}_y \quad (2\text{-}3)$$

$$\{R'RC=O\}_z + \{CH_2C\bullet OH\}_y \rightarrow \{R'RC\bullet OH\}_z + \{CH_2C=O\}_y \quad (2\text{-}4)$$

$$\{R'RC\bullet OH\}_z + O_2 \rightarrow \{R'RC(OH)OO\bullet\}_z \quad (2\text{-}5)$$

$$\{R'RC(OH)OO\bullet\}_z \rightarrow \{R'RC=O\}_z + HO_2\bullet \quad (2\text{-}6)$$

$$HO_2\bullet \leftrightarrows H^+ + \bullet O_2^- \quad (2\text{-}7)$$

$$HO_2\bullet + H^+ + \bullet O_2^- \rightarrow H_2O_2 + O_2 \quad (2\text{-}8)$$

Reaction 2-5 is identical to reaction 2-2.

Examination of the results presented in Figures 2-2 and 2-7 reveals that a maximum in the peroxide concentration usually occurs when $[H_2O_2] = [O_2] = ½\,[O_2]_0$, where $[O_2]_0$ is the initial

oxygen concentration. Based on these results the logical conclusion is that at the time the maximum takes place, rate(O_2 consumption) = rate(H_2O_2 consumption)

The obvious conclusion is that k(O_2 consumption) = k(H_2O_2 consumption), but this is incorrect. For instance, in the case of $(CH_3)_2C\bullet OH$, the α-hydroxy radical derived from 2-propanol,[11]

$k\{(CH_3)_2C\bullet OH + O_2\} = 4 \times 10^9\ M^{-1}\ s^{-1}$

$k\{(CH_3)_2C\bullet OH + H_2O_2\} = 5 \times 10^5\ M^{-1}\ s^{-1}$

Although the SPEEK radical is expected to react slower than $(CH_3)_2C\bullet OH$, a logical assumption is that the differences in reactivity would be similar for both radicals. In addition, reduction of H_2O_2 by α-hydroxy radicals can lead to chain reactions.[6a]

Considering the much lower rate constant for the reduction of H_2O_2 by $(CH_3)_2C\bullet OH$ than the reaction with oxygen, an obvious path that would lead to equal rates of oxygen and peroxide consumptions involves a radical chain process. The following mechanism can describe qualitatively such chain reaction:

$$\{R'RC\bullet OH\}_z + H_2O_2 \rightarrow \{R'RC=O\}_z + \bullet OH + H_2O \qquad (2\text{-}9)$$

$$\bullet OH + \{CH_2CHOH\}_y \rightarrow H_2O + \{CH_2C\bullet OH\}_y \qquad (2\text{-}10)$$

and

$$\{R'RC=O\}_z + \{CH_2C\bullet OH\}_y \rightarrow \{R'RC\bullet OH\}_z + \{CH_2C=O\}_y \qquad (2\text{-}4)$$

Evidence in favor of such mechanism was obtained via photolysis, in a sealed vessel, of a degassed SPEEK/PVA solution containing 0.1 mM H_2O_2. A short illumination generated a

small amount (several μM) of SPEEK radicals that initiated the chain process via reaction 2-9. The net result was complete consumption of the peroxide in about 15 min and optical measurements showed that a constant [SPEEK•] persisted during this process.

Conclusions

The results gathered in the present investigation demonstrate that H_2O_2 is generated in solutions of SPEEK/PVA that contained air. Formation of the peroxide occurs in a synchronous fashion with the consumption of oxygen. The kinetic data is consistent with a mechanism in which the rate-determining step is the photochemical process that generates the polymeric SPEEK radicals. Maximum rates of peroxide formation are obtained in neutral solutions, which suggest that efficient formation of H_2O_2 on the surface of SPEEK/PVA fibers is feasible. The decay of H_2O_2 that takes place at low oxygen concentrations in solution is not expected to occur in the case of the fibers due to the high and constant [O_2] that prevail on the surface of these polymeric materials.

References

(1) Carlini, C.; Angiolini, L.; Caretti, D.; Corelli, E. *Polym. Advanced Technol.* **1996**, *7*, 379-384.

(2) Gu, C.; Xu, Y.; Liu, Y.; Pan, J. J.; Zhou, F.; He, H. *Optical Mater.* **2003**, *23*, 219-227.

(3) Tian, H.; Yang, S. *Chem. Soc. Rev.* **2004**, *33*, 85-97.

(4) Ercole, F.; Davies, T. P.; Evans, R. A. *Polym. Chem.* **2010**, *37*, 37-54.

(5) Irie, M.: Ikeda, T. In *Functional Monomers and Polymers*; Takemoto, K.; Ottenbrite, R. M.; Kamachi, M. Eds.; Marcel Dekker: New York, 1997; p. 65-116.

(6) (a) Malone, K.; Weaver, S.; Taylor, D.; Cheng, H.; Sarathy, K. P.; Mills, G. *J. Phys. Chem. B* **2002**, *106*, 7422-7431. (b) Weaver, S.; Taylor, D.; Gale, W.; Mills, G. *Langmuir* **1996**, *12*, 4618-4620.

(7) *Organic Photochromic and Thermochromic Compounds*; Crano, J; R. Guglielmetti, R., Eds.; Kluwer Academic/Plenum Publishers: New York, 1999; Vol. 2.

(8) (a) Korchev, A. S. ; Konovalova, T.; Cammarata, V.; Kispert, L.; Slaten, B. L.; Mills, G. *Langmuir* **2006**, *22*, 375-384. (b) Korchev, A. S.; Shulyak, T. S.; Slaten, B. L.; Gale, W. F.; Mills, G. *J. Phys. Chem. B* **2005**, *109*, 7733-7745. (c) Korchev, A. S.; Sartin, M.; Mills, G.; B. L. Slaten, B. L.; Gale, W. F. In *Clusters and Nano-Assemblies: Physical and Biological Systems*; Jena, P.; Khanna, S. N.; Rao, B. K.; Eds, World Scientific Publishing Co.: Singapore, 2005; 371-377. (d) Korchev, A. S.; Bozak, M. J.; Slaten, B. L.; Mills, G. *J. Am. Chem. Soc.* **2004**, *126*, 10-11.

(9) Gilbert, A.; Baggott, J. *Essentials of Molecular Photochemistry*; CRC Press: Boca Raton, 1991; Chapter 7.

(10) Ulanski, P.; Bothe, K.; Rosiak, J. M.; von Sonntag, C. *Macromol. Chem. Phys.* **1994**, *195*, 1443-1461.

(11) Neta, P.; Grodkowski, J.; Ross, A. B. *J. Phys. Chem. Ref. Data* **1996**, *25*, 709-1050.

(12) Lien, L.; Fellows, C. M.; Copeland, L.; Hawkett, B. S.; Gilbert, R, G. *Aust. J. Chem.* **2002**, *55*, 507.

(13) von Sonntag, C.; Bothe, E.; Ulanski, P.; Adhikary, A. *Radiat. Phys. Chem.* **1999**, *55*, 599-603.

(14) Bielski, B. H.; Cabelli, D. E.; Arudi, R. L.; Ross, A. B. *J. Phys. Chem. Ref. Data* **1985**, *14*, 1041-1100.

(15) Görner, H. *Photochem. Photobiol.* **2006**, *82*, 801-808.

(16) Radschuwelt, A.; Rüttinger, H.-H.; Nuhn, P.; Wohlrab, W.; Huschka, C. . *Photochem. Photobiol.* **2001**, *73*, 119-127.

(17) Pitts, Jr., J. N.; Letsinger, R. L.; Taylor, R. P.; Patterson, J. M.; Recktenwald, G.; Martin, R. B. *J. Am. Chem. Soc.* **1959**, *81*, 1068-1077.

(18) (a) Winkelmann, K.; Calhoun, R. L.; Mills, G. *J. Phys. Chem. A* **2006**, *110*, 13827-13835. (b) Calhoun, R. L.; Winkelmann, K.; Mills, G. *J. Phys. Chem. B* **2001**, *105*, 9739-9746. (c) Weaver, S.; Mills, G. *J. Phys. Chem.* **1997**, *101*, 3769-3775.

(19) Gonzalez, M. C.; Le Roux, G. C.; Rosso, J. A.; Braun, A. M. *Chemosphere* **2007**, *69*, 1238-1244.

(20) Schreuder-Gibson, H.; Truong, Q.; Walker, J. E.; Owens, J. R.; Wander, J. D.; Jones, Jr., W. E. MRS Bulletin 2003, 574-578.

(21) Singh, A.; Lee, Y.; Dressick, W. J. *Adv. Mater.* **2004**, *16*, 212-215.

(22) (a) Wagner, G. W.; Sorrick, D. C.; Procell, L. R.; Brickhouse, M. D.; Mcvey, I. F.; Schwartz, L. I. *Langmuir* **2007**, *23*, 1178-1186. (b) Wagner, G. W.; Yang, Y.-C. *Ind. Eng. Chem. Res.* **2002**, *41*, 1925-1928.

(23) (a) Hong, K. H.; Sun, G. *J. Appl. Polym. Sci.* **2009**, *112*, 2019-2026. (b) Hong, K. H.; Sun, G. *J. Appl. Polym. Sci.* **2008**, *109*, 3173-3179. (c) Hong, K. H.; Sun, G. *Polym. Eng. Sci.* **2007**, *47*, 1750-1755.

(24) Heller, H. G.; Langan, J. R. *J. Chem. Soc., Perkin Trans. 2* **1981**, 341-343.

(25) Kormann, C.; Bahnemann, D. W.; Hoffmann, M. R. *Environ. Sci. Technol.* **1988**, *22*, 798-806.

(26) Stefanic, I.; Asmus, K.-D.; Bonifacic, M. *Phys. Chem. Chem. Phys.* **2003**, *5*, 2783-2789.

(27) Wilkinson, F.; Brummer, J. G. *J. Phys. Chem. Ref. Data* **1981**, *10*, 809-999.

(28) Mosinger, J.; Mosinger, B. *Experientia* **1995**, *51*, 106-109.

(29) Ramseier, M.; Senn, P.; Wirz, J. *J. Phys. Chem. A* **2003**, *107*, 3305-3315.

(30) Beckett, A.; Porter, G. *Trans. Faraday Soc.* **1963**, *59*, 2038-2050.

III. PROBING REACTION MECHANISMS RELEVANT TO THE HIGH ENERGY CHEMISTRY OF NITROMETHANE

Introduction

Energetic materials (EM) able to modify their sensitization to initiation via some type of external stimulus (light, temperature, electric field) are attractive as explosives containing additional safety features. For example, this type of explosive could be remotely deactivated if the munition was in enemy hands or if left behind in the battle field, thus eliminating the need to transport or disarm the EM before departing an active military zone. In most military applications, initiation of EM is induced by a high impact shock wave that compresses and heats molecules within the EM, thus priming the molecular environment for fast thermal decomposition. In general, the shock wave is the "trigger", which begins the initiation of the EM towards detonation. Detonation or detonation fronts are created due to the rapid release of exothermic energy at supersonic speeds, which accelerate and overtake the initial propagating shock front within the medium.[1] Initiations of explosives, more specifically explosive molecules, follow a chain decomposition reaction believed to begin with bond dissociation (induced by the high pressure of the shock wave) and ultimately followed by hot gaseous byproducts (CO_2, H_2O, N_2, CO, etc.)[2]. Ultimately, control over the sensitivity of munitions is a real concern for the handler as well as how the material has to be stored, thus the ability to modify the sensitivity of an explosive is very important.

For detonation of heterogeneous liquids, the shock wave enters the EM and adiabatically compresses voids (bubbles, hollow glass beads, polymer foams) filled with entrapped gases causing areas of local heating, so called "hot spots". For heterogeneous solids, hot spots are

thought to be formed through mechanical or electrical disruption (friction, shear, distortion, pile-up, etc) of localized voids. These hot spots reach extreme temperatures capable of inducing thermal decomposition of neighboring molecules that can expand/coalesce into a propagating wave of hot gases and pressure. This propagating wave can become a deflagration (fast burning) wave traveling at subsonic speeds or a detonation wave (shock wave that is chemically driven) traveling at supersonic speeds. Ultimately this detonation wave overcomes the original shock wave and amplifies the thermal decomposition reaction of energetic molecules to the point of extreme temperatures and pressures resulting in an explosion. It is worthy to note that the detonation mechanism for heterogeneous liquids has been reported to follow a somewhat different path, albeit similar to the above description, where hot spot formation is generated at pre-shocked cavities impacted by a jet stream, which then rapidly undergo adiabatic compression forming a detonation wave propagating to an explosion.[3] Nonetheless, hot spots play a critical role in the initiation thresholds (*i.e.* sensitivity) of EM.

Of particular interest to this work are sensitized liquid EM such as nitromethane, CH_3NO_2. Sensitization of such EM typically involves the addition of a powder or fine particulate material that is used to create voids that aid in the initiation or propagation of the detonation wave. For CH_3NO_2, sensitizers such as active EM (RDX, ammonium nitrate) or non-active materials (aluminum, copper, fumed silica, boron carbide, air bubbles, hollow microballoons, etc.) can be added to induce detonation at lower pressures and temperatures than what is required in neat CH_3NO_2.[4, 5, 6] Earlier studies reported that sensitization of liquid EM, in the presence of gas-filled cavities, required hot spots within the diameter range of 0.1 μm to 10 μm in order to achieve ignition.[7] However, others report that hot spots can be much smaller as long as they are able to initiate the thermal decomposition of just a few neighboring molecules under adiabatic

compression.[8] Nonetheless, many mechanisms have been proposed for the formation of hot spots and their sequential steps in initiating an EM. The reason that multiple mechanisms have been reported for the same fundamental sensitization event is due in part to the difficulty in measuring the reaction mechanism under high strain rates (within the shock wave) as well as the fact that different techniques (experimental set-up, measurement conditions) employed to investigate this phenomenon are not easily comparable *e.g.* thermal sensitization by temperature/laser irradiation, compression by a shockwave, etc. Additionally, recent observations on the detonation mechanisms governing EM by Ramaswamy suggests that coalescence of many smaller "reactions" sites is an alternative pathway for hot spot formation.[9] In the previous work, the author describes the formation of micron scale hot spots originating from reactions sites on the nanometer scale (submicron). Their findings suggest that hot spots begin when adjacent molecules are triggered (compressed by a shock wave, irradiated with a laser) into decomposition at the atomic/molecular level. From this point, hot byproducts of the decomposing molecules swiftly migrate into nanometer reaction sites along interfaces (solid-liquid, solid-gas, and liquid-gas). Finally, coalescence of the reaction sites into micron size hot spots are generated leading to sensitization. Given this mechanism for hot spot formation and many others, a need for novel experimental designs are required to unravel evidence that might support or dismiss these models and provide greater insight and understanding to this phenomenon.

Conclusive evidence for the model proposed by Ramaswamy for hot spot formation is still lacking given that none of the previously employed EM can clearly distinguish between conventional hot spot formation and the coalescence mechanisms for hot spot formation. Liquid homogenous EM, which do not contain voids, are well suited to test the occurrence of the

coalescence mechanism. The challenge is to produce a system where reaction sites are possible only along liquid-gas interfaces originating from bubbles dispersed in the fluid phase, yet the fusion of the bubbles must be suppressed to prevent their thermodynamically favored growth. Therefore, stable dispersions of nanometer-sized gas bubbles in liquid explosives are required to verify experimentally the coalescence mechanism. Meeting these requirements has proven to be difficult mainly due to the inability to embed and sustain nanometer size gas bubbles in a liquid EM.

In this work we proposed that photoresponsive nanoporous (PN) materials, shown below, would be an ideal system to test the coalescence mechanism. As mentioned above, CH_3NO_2 is considered a safe industrial solvent used in many applications, however it can be readily detonated when μm size gas bubbles are added as sensitizing agents to facilitate hot spots formation.[3, 5] The central idea in this work is to use PN materials as the sensitizing agent for CH_3NO_2 via the mechanism involving coalescence of reaction sites.

In accordance to hot spot theory, sensitization of CH_3NO_2 with the addition of this photoresponsive material could be switch between a coalesced void state (pores filled with CH_3NO_2) to a non-sensitizing state (voids empty) by exposure to light. Such materials have been made as films consisting of a ~260 nm thick mesoporous silica framework possessing interconnected pores with an diameter of 3.2 nm, separated by 2.4 nm thick SiO_2 walls.[10] Attached to the pore walls are azobenzene ligands that undergo *trans*-to-*cis*-isomerization upon exposure to 350-360 nm photons; the reverse reaction occurs with heat or under illumination with $\lambda > 420$ nm.

Shown in Figure 3-1 (from ref. 10a) is a cross-sectional representation of the pores before and after the photoisomerization takes place. As depicted on the left of Fig. 3-1, interaction of

aromatic groups of azobenzene ligands in the *trans* configuration creates a central "channel". Photoisomerization to the *cis* form of the azobenzene ligand increases the diameter (by ~0.4 nm) of the central channel; this change is highlighted on the right-side of Fig. 3-1.

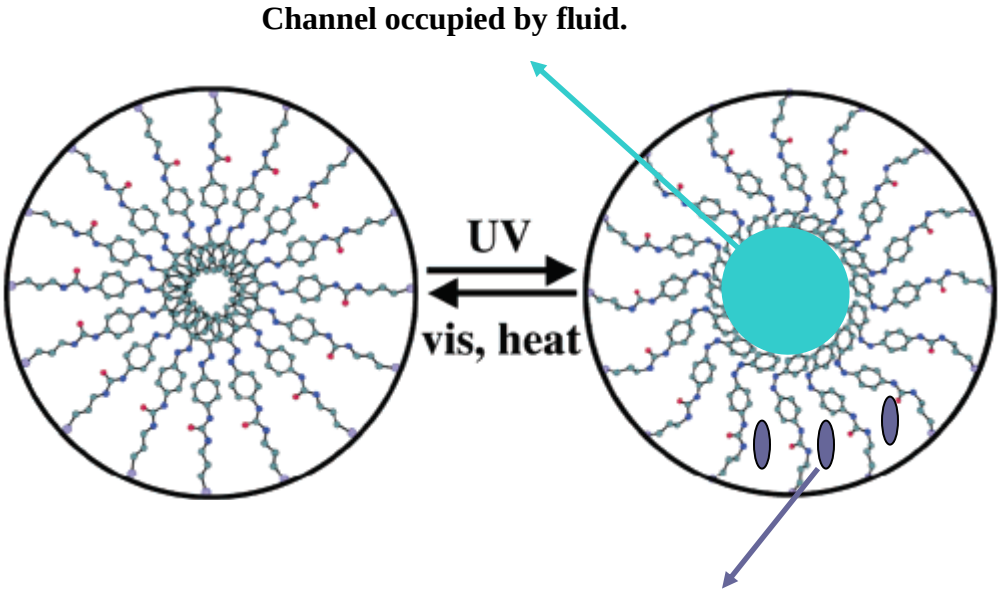

Figure 3-1. Left side: representation of the azobenzene ligands in the *trans* configuration; changes resulting from isomerization to the *cis* form are shown on the right side. Adapted with permission from ref 10a. Copyright 2004 American Chemical Society.

Chronoamperometric data suggest that water moves across PN "membranes" upon exposure to UV photons, but hardly any liquid flows in the absence of light.[10a] Thus, light provides the energy to induce a pumping action resulting from photoisomerization of the azobenzene ligands that increases significantly the flow of liquid through the PN materials. Motion of liquids is very inefficient in narrow pores because, according to the Hagen-Poiseuille law, the flow of Newtonian fluids along cylindrical tubes scales with the 4th power of the tube radius.[11] Flow of H_2O across photolyzed films seemed to occur mainly along the central "channel" defined in Fig.

3-1 (highlighted aqua circle) by the end groups of the azobenzene ligands.[10a] Also, since the distance separating azobenzene ligands at the pore wall is very short (~1 nm),[10b] small air pockets may form between the chromophore molecules. Highlighted on the right side of Fig. 3-1 (purple ovals) is a region where formation of air pockets is probable. Because it is unlikely that much liquid will flow in that region of the pores, the air pockets formed on the SiO_2 walls are anticipated to be fairly stable.

The close proximity of liquid CH_3NO_2 and gas pockets suggests that PN systems are unique materials that will enable formation of hot spots exclusively via coalescence of reaction sites.[9] Conventional hot spot formation (via cavity collapse/jet streaming or adiabatic gas compression) is not feasible since the pore diameters are < 100 nm, and also because the liquid will occupy part of the internal volume. Sensitization is expected to occur when dispersions of the nanoporous materials in liquid CH_3NO_2 are subjected to conditions that trigger initiation.[5]

In order to test the coalesce theory with the above mentioned PN material and ultimately engineer this material as a reversible sensitizing agent for a homogeneous liquid explosive, initial efforts were allocated to expand on the work of Liu *et al.* for purposes of selecting the best candidate for sensitization testing. Presented in this work are the results for the synthesis and characterization of PN films and powders of varying pore morphology, ligand mobility, and particle structure. PN films were studied initially given the inability to suspend PN powders in liquid CH_3NO_2, thus making continuous/subsequent measurements on the same sample impractical. Investigations into the pore structure and mass transport performance of PN films in the presence/absence of CH_3NO_2 while subjected to UV-Vis irradiation will be presented and discussed. PN powders will be evaluated and discussed with respect to their inherent properties (pore morphology, ligand mobility, and particle size and shape) and their potential as an effective

sensitizer. Information obtained on the structure and/or dynamics of these PN materials in the absence/presence of CH_3NO_2 are critical for future sensitivity measurements.

Background

Studies on EM entrapped in porous materials was conducted by Spitzer *et al.* by inclusion of nanometer size RDX particles in a porous matrix composed of Cr_2O_3.[12] Results from these studies showed that the transition from deflagration to detonation was dependent on the continuity of the explosive phase in the host matrix. Furthermore, the sensitivity and combustion rate for these energetic nanocomposites was dictated by the ratio of loaded RDX nanoparticles to the available surface area within the host matrix. More specifically, greater sensitivity was witnessed (even higher than pure RDX microparticles) when the host matrix was loaded between 60 - 80% RDX. This observation was attributed to the close proximity of neighboring decomposing EM particles able to propagate swiftly throughout the host matrix. Results from this study could be evidence of the coalesce mechanism. However, the porosity of the host matrix was defined as the space between neighboring Cr_2O_3 nanorods (mean diameter of 17.6 nm) contained within micron sized particles (~27 nm). This free space was enclosed between neighboring nanorods, thus complete inter-pore-connectivity was most likely not obtainable in this composite and would be necessary to validate the coalesce mechanism. Nonetheless, this work is of interest to the findings of this study. If PN materials are successful in sensitizing NM they could be applied to the aforementioned work to further the study of sensitization and combustion rates of entrapped solid EM, except the host matrix (PN material) would possess greater pore structure and inter-pore-connectivity.

Sensitization studies on CH_3NO_2 in the presence of micron sized solid silica particles (1-4 μm & 40 μm) showed that hot spot formation is generated at the interface of the external surface from impedance mismatches induced from the entering shockwave.[13] Studies for this work also demonstrated that hot spot formation via cavity collapse of hollow glass bubbles (38-45 μm diameter) were more effective as a sensitizing agent than solid silica particles. In addition, correlations between the inter-particle spacings of the different size particles showed that smaller particles of equal loading weights induced detonation at lower pressures as compared to larger particles of the same loading weight. This suggests that sensitization studies with PN particles dispersed in CH_3NO_2 should be as small as possible in order to increase the ratio of pore surface area to external particle surface. The reason is that hot spot formation via shock impedance mismatch between the particle surface and the surrounding liquid could participate in the sensitization event and prevent accurate measurements for the detonation of CH_3NO_2 dictated solely by cavity collapse. Shock impedance mismatch arises at the interface at two materials with different densities such as solids and liquids. Partial reflection of the shockwave from the solid into the liquid increases the fluid pressure at the boundary, resulting in hot spots. While this mechanism may be less significant than cavity collapse of pores, hot spots formation can result in liquids containing dispersed solids through shock impedance mismatch. Also, shorter inter-particle spacings can be achieved with smaller particles with lower concentrations as compared to those needed for larger particles.

PN materials used here were synthesized following the sol-gel technique - evaporation-induced surfactant directed self assembly (EISA).[10] In the EISA approach, inorganic precursors and a structure directing agent (SDA) are combined in a solution wherein favorable conditions are achieved (*i.e.*, composition, stoichiometry, inhibiting agent or polymerization catalyst, aging

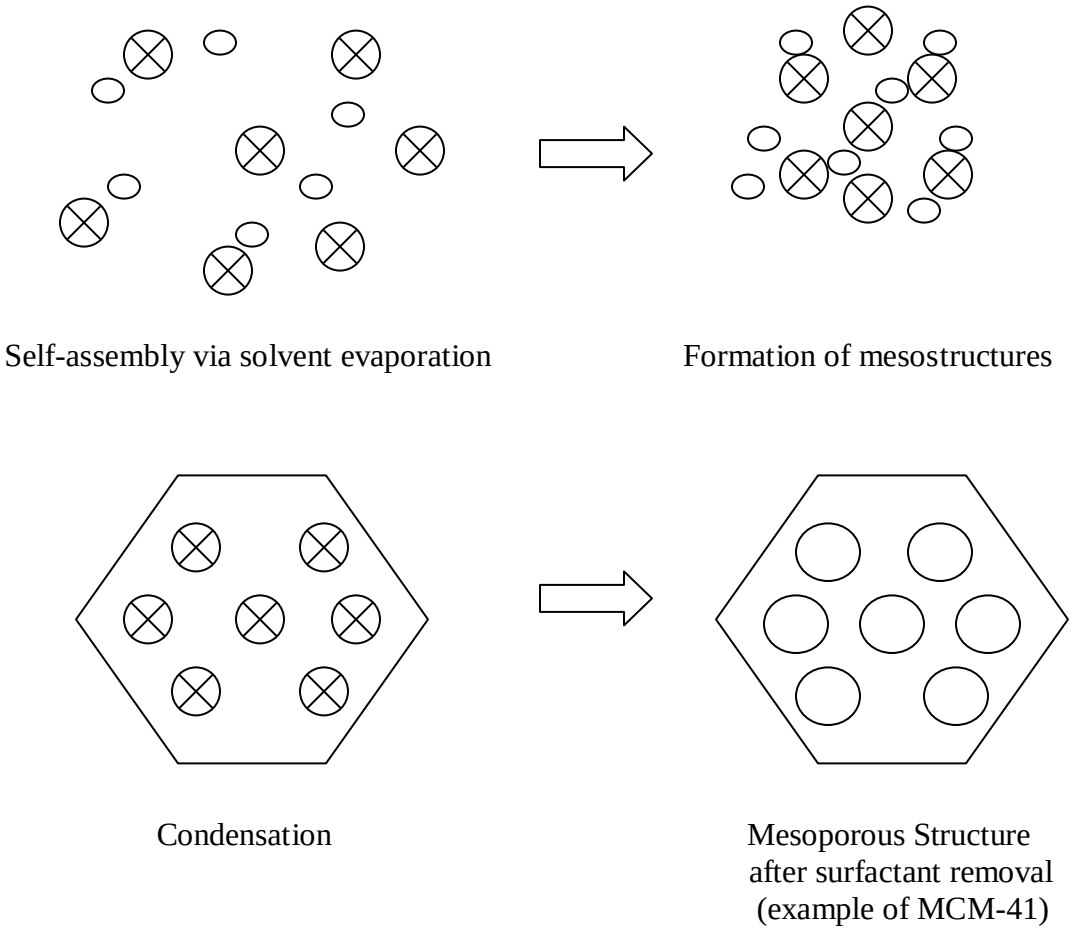

Figure 3-2. General EISA process for the formation of mesoporous materials (films and powders). From the top (left to right): micelles (⊕) and inorganic precursors (○) self-assemble during the initial evaporation phase followed by formation of mesostructures. From the bottom (left to right): solidification of the liquid mesophase via polymerization of the surrounding siloxane network followed by surfactant removal, from the mesopores, leaving behind the final mesoporous structure.

time, evaporation rate, etc.) for designing mesoporous materials with specific properties (pore size, pore morphology, ligands within the pore walls, etc).[14] As presented in Figure 3-2, the EISA process precedes in three steps; 1) solvent evaporation 2) mesostructuration and 3) condensation. After components are homogenously dispersed in a solution, solvent evaporation initiates the self-assembly of structure directing agents (*i.e.* surfactants) into spherical micelles.

When the concentration of the surfactant increases upon evaporation of the solvents, micelles begin to form if the SDA concentration is below the critical micelle concentration (CMC). After formation of micelles, inorganic precursors and other parts (mediator ions, modified siloxane ligands, etc., if added) will begin to surround and/or embed themselves into the micelles to form highly ordered structures; this step is known as mesostructuring. From this point, condensation is induced via heat, evaporation, pH, etc., which solidifies the inorganic precursors into a silica matrix around the micelles, thereby securing the mesostructural frame. Afterwards, the material is exposed to high heat and/or acidic baths in order to remove the surfactants from the mesopores leaving behind an open mesoporous material with high structural order. The overall transformation can be summarized as polycondensation of inorganic precursors that are surrounding ordered micelles in a crystal like mesostructure. The most prominent factors that influence EISA processes are the ratio of surfactant to inorganic precursor, the chemical nature of the inorganic precursor (sol-gel conditions), and the relative humidity influence during solvent evaporation.[15, 16]

Experimental

Materials: Brij 56, tetraethyl orthosilicate (TEOS), and triethoxysilypropyl isocyanate (95%) were purchased from Aldrich. Nitromethane (98.5%), MCM-41, MSU-H, and HMS were purchased from Sigma Aldrich. Mica was from Axim Mica, ruby mica), HCl was from Fisher, ethanol (99.98%) was from Pharmco-AAPER, and 4-phenylaniline (95%) was obtained from TCI America. All materials were used as received without further purification.

Synthesis of TSUA: 4-(3-triethoxysilypropyl-uriedo)azobenzene (TSUA) was synthesized in accordance with reference 17.

Sol-gel synthesis procedure: dip coated and spin coated films were made from a sol-gel composition following procedures in reference 10b. For example, Brij 56 (0.27 g) and TSUA (0.26 g) were dissolved in CH_3CH_2OH (6 mL) which contained TEOS (1.08 mL). After addition of HCl (0.5 mL, 0.1 M) the solution was sonicated for 3 min and aged for 30 min before depositing on substrates. Mica substrates were cleaned in a 1 M solution of HCl in CH_3CH_2OH for 30 min before utilization as a substrate for deposition. Spin coated films were deposited on a clean mica substrate at 1600 rpm for 30s. Dip coated films were deposited at a rate of ~1 cm/min on a clean mica substrate. After deposition, films were treated to remove the surfactant in accordance with reference 10b.

Mesoporous powders were made from the previous described sol-gel solution with slight modifications: Sol1-2 was synthesized starting with the aforementioned sol-gel solution with the addition of 25 mL of deionized water and 4 mL of ethanol (overall pH ~ 2.8). Sol1-3 was synthesized with the sol-gel solution with the addition 10 mL of 0.1 M HCl in deionized water (overall pH ~ 1.6). Both mixtures were placed in 250 mL polypropylene bottles with caps loosen (to allow for evaporation) and stirred for 5 days in the dark in a semi-controlled surrounding. After 5 days of stirring, solutions were left standing for 1 month then processed to remove the surfactant in accordance with reference 10b.

FT-IR: Fourier transform infrared (FTIR) spectra of the samples were obtained in the transmission mode from KBr samples pressed into pellets, on a Shimadzu IR-Prestige 21 spectrometer at a resolution of 4 cm^{-1}.

ATR: ATR spectra were recorded on the Mattson RS-1 with Harrick Twin Parallel Mirror Reflection Variable Angle ATR accessory. Germanium ATR crystals were used as substrates and were cleaned by plasma etching for 30 min under air. Spectra were recorded on a Mattson

RS-1 FTIR spectrometer with a Harrick variable angle ATR accessory using twin parallel mirror reflection. Germanium ATR crystals (single pass parallel piped, 50 mm X 10 mm X 2 mm) were used as internal reflection elements. The background spectra were recorded with the Ge crystal contacting nitrogen gas in the absence of sample. All of the IR data were collected at a spectral resolution of 4 cm^{-1} with 500 co-added sample scans using a high D* MCT-A detector with N_2 purge of the sample compartment.

NMR: H^1 nuclear magnetic resonance measurements (NMR) were made at 400.18 MHz with a Bruker NMR spectrometer. TSUA was dissolved in deuterated dimethyl sulfoxide.

UV-Vis Spectroscopy: Optical densities were measured on a Shimadzu UV-Vis PC2501 spectrophotometer with a resolution of 1 nm. Illuminated films and powders were positioning at mid-height inside a Rayonet that generated photons with $\lambda = 350$ nm ± 15 nm (16 RPR-3500A lamps) or $\lambda = 420$ nm ± 10 nm (16 RPR-4190 lamps).

Diffuse Reflectance Measurements: Optical spectra were recorded in diffuse reflectance mode using a Kubelka-Munk transform with a Shimadzu UV-Vis PC2501 spectrophotometer. Samples were diluted with $BaSO_4$ powder and pressed into the sample holder.

XRD: X-ray diffractograms (XRD patterns) were recorded between the scan range of $2\theta = 1.5$ and 7^o using a Cu radiation source (Cu Kα, $\lambda = 1.54178$ Å) on a Rigaku Miniflex diffractometer.

Single Crystal XRD: Crystals suitable for single crystal XRD of TSUA were grown from hexane at room temperature. A single crystal was mounted on a glass fiber with paratone-n oil. Unit cell data was collected and was determined to be the previously reported structure. Data was collected at 173 K on a Bruker Apex Single Crystal Diffractometer using the SMART software package.

Nitrogen Absorption Measurements: Nitrogen adsorption measurements were performed using an ASAP 2020 (Micrometrics, Inc.) volumetric analyzer at -196°C with ultra high purity nitrogen gas. All samples were degassed under vacuum at 100°C for 3 h prior to measurement. Adsorption parameters for the samples were determined from the collected nitrogen adsorption data. The specific surface area (SBET) was calculated using the BET method in the relative pressure range of 0.05 to 0.2.[18] The single point pore volume (*Vsp*) was calculated from the adsorption isotherm at a relative pressure of 0.98. Pore size distributions (PSDs) were calculated from the adsorption branches of nitrogen adsorption-desorption isotherms using the improved KJS method[19], calibrated for cylindrical pores in the range from 1-50 nm. The pore width (*wKJS*) was obtained at the maximum of the PSD curve. Total pore volume (*VT*) and micropore volume (*Vmi*) were evaluated by integration of the PSD curve (up to ~3 nm for micropore volume).

Transmission electron microscopy (TEM): images were acquired using a FEI Titan field-emission microscope operating at 300 kV. Samples were prepared by suspending the powders in hexanes via mild sonication and drop drying the suspension onto a 200 mesh Cu grid coated with an ultrathin holey carbon film.

Scanning electron microscopy images (SEM): images were acquired using a FEI Quanta field-emission microscope. Samples were prepared by drop drying a suspension of the powders in acetone onto an aluminum stub. To minimize the effects of charging all samples were covered with an atomic layer of carbon.

Results and Discussion

PN films and powders were composed from an EISA process outlined in reference 10b, with some modifications for powders. This method utilizes an inorganic precursor tetraethyl

orthosilicate (TEOS) combined with a azobenzene modified silane ligand (4-(3-triethoxysilypropyl-uriedo)azobenzene –TSUA) as a co-surfactant, in the presence of a structure directing agent (Brij56, $C_{20}H_{42}O_5$) mixed in an homogenous acidic CH_3CH_2OH / H_2O solution (pH = 2).

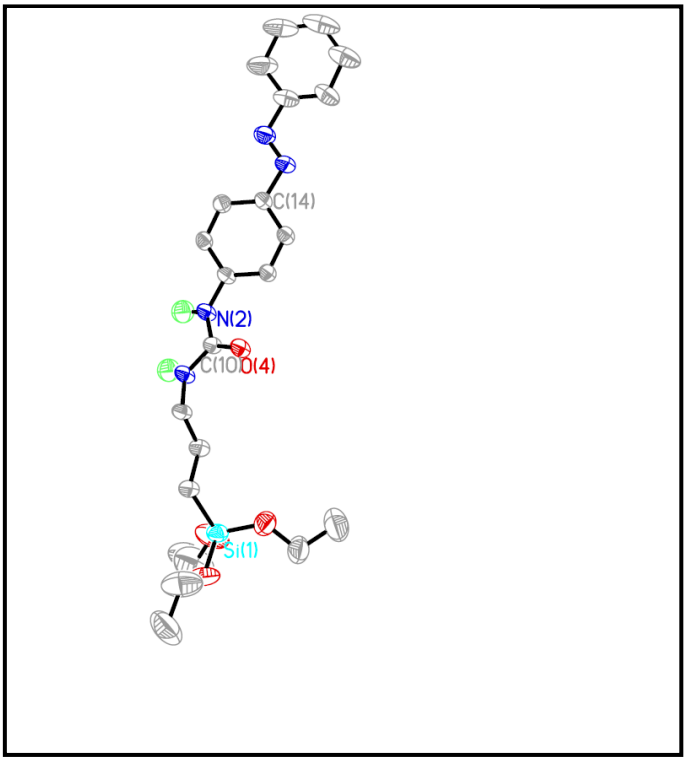

Figure 3-3. Asymmetric unit for 4-(-3-triethoxysilylpropyl-uriedo)azobenzene (TSUA) in hexane. C (grey), O (red), H (green), N (blue) and Si (aqua). Unit cell constants a = 15.538(**15.430**), b = 9.245(**9.247**), and c = 18.482(**18.504**); for comparison, unit cell constants in bold face are included from reference 17.

In this EISA process, micelles are formed containing TSUA molecules aligned in an ordered position due to hydrophobic/hydrophilic forces. The silicic acid groups of TSUA settle next to the hydrolyzed TEOS moieties (exterior micelle wall) and the hydrophobic propylureidoazobenzene groups of TSUA are driven inward by the hydrophobic micelle core.

Developing PN materials for future sensitization testing requires many steps. They include: 1) synthesis and confirmation of TSUA; 2) confirmation of TSUA photoisomerization; 3) characterization of pore morphology; 4) confirmation of ligand mobility; 5) spectral identification of TSUA in CH_3NO_2; 5) mass transport control of CH_3NO_2; 6) inclusion/retention of CH_3NO_2; and 7) ligand mobility at longer wavelengths. Each of these steps will be discussed in the following sections.

Confirmation of the Synthesis of TSUA

Structural conformation for the synthesis of TSUA was determined by single crystal XRD, melting point, FT-IR and NMR. Shown in Figure 3-3, is the crystal structure for TSUA in hexane validated by single crystal XRD with unit cell constants similar to that reported by Liu *et al.*, which was crystallized in acetone.[17] Melting point was detected on a Mel-Temp instrument (open air) which gave an average reading of 129.8 ˚C as compared to 127.5 ˚C from reference 17, which utilized thermogravimetric analysis (TGA), in argon, to determine the melting point.

Three characteristic vibrational bands were identified in TSUA via FT-IR spectroscopy indicative to the –NH-CO-NH- urea group: ν = 3346 cm^{-1} (NH stretch), 1651 cm^{-1} and 1560 cm^{-1} (amide I and II stretches). The previous vibrational bands were not witnessed in 4-phenylaniline (starting product), which showed vibrational bands for a free NH_2 group: ν = 3464 cm^{-1} (Ar-NH_2, antisym.), 3381 cm^{-1} (sym.), and 1618 cm^{-1} (Ar-NH_2 scissors).[20] Confirmation of these vibrational bands for the urea groups shows binding of triethoxysilypropyl isocyanate to 4-phenyazoaniline, scheme 3-1. H^1 NMR spectroscopy of TSUA in deuterated dimethyl sulfoxide (d^6-DMSO) show similar peaks to those reported by Lui *et al*., Table 3-1.[17] However, the exact multiplicity of the three proton NMR peaks in the range of 7.58 ppm to 7.45 ppm was not distinguishable due to a high degree of overlap and *J-J* coupling in these range.

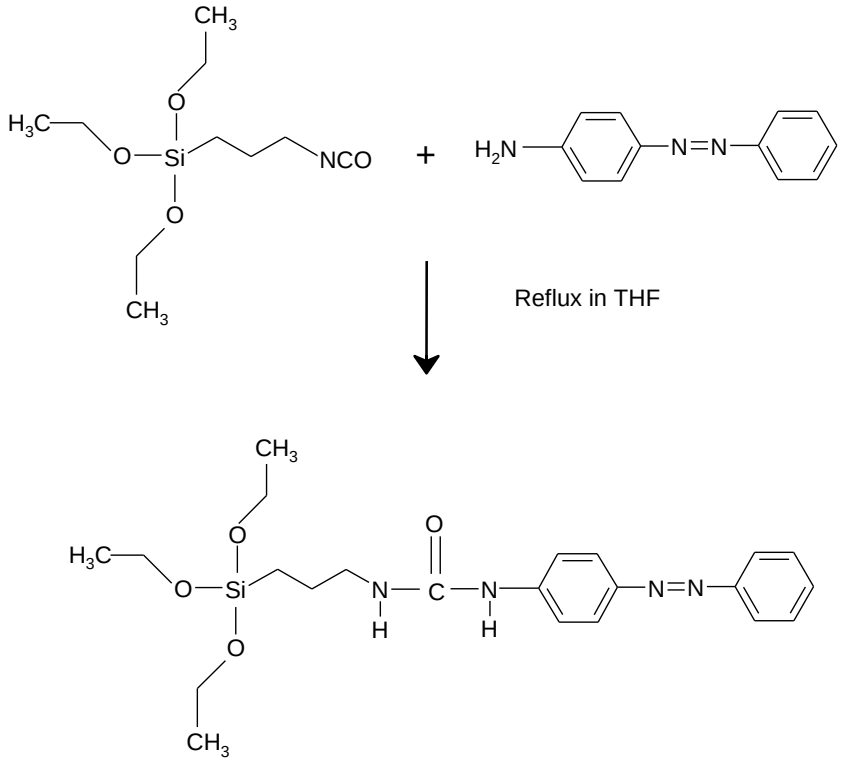

Scheme 3-1. Synthesis of TSUA.

Photoisomerization of TSUA in ethanol (ligand mobility)

Photoisomerization of synthesized TSUA ligand was measured with UV-Vis spectroscopy. Figure 3-4 shows a UV-Vis spectra of TSUA in ethanol under different exposure times to 350 nm light, visible light (room light), and heat. The *trans* configuration of the azobenzene ligand absorbs at λ_{max} = 364 nm (π-π*) and the *cis* configuration at λ_{max} = 340 nm and λ_{max} = 444 nm (n-π*) respectively, see Figure 3-4. The initial spectrum of TSUA in ethanol shows a large absorption band at 364 nm, signifying that the azobenzene ligand is predominantly present in the thermally stable *trans* configuration. After 1 minute of irradiation with 350 nm light, the azobenzene ligand has converted completely (100% starting from spectrum a) from the predominately *trans* state to the *cis* state. Complete conversion into the *cis* configuration was

Table 3-1. Proton NMR spectrum data of TSUA in deuterated DMSO.

Group	Proton Shift (ppm)*	Proton Shift (ppm)
urea H close to aryl, 1H	8.86(s)	8.9 (s)
^{3}J(H,H), the other urea H, 1H	6.32(t)	6.3(t)
^{3}J(H,H), aryl H, 4H	7.79(d)	7.8(d)
^{3}J(H,H), aryl H, 2H	7.58(d)	M
^{3}J(H,H), aryl H, 2H	7.51(t)	M
^{3}J(H,H), aryl H, 1H	7.45(t)	M
-NCH_2-, 2H	3.06(m)	3.1(q)
-CCH_2C-, 2H	1.47(m)	1.5 (se.)
^{3}J(H,H), -CH_2Si-, 2H	0.53(t)	0.5(t)
^{3}J(H,H), -OCH_2, 6H	3.70(q)	3.7(q)
^{3}J(H,H), -CH_3, 9H	1.10(t)	1.2(t)

s = singlet; d = doublet; t = triplet; q = quartet; se = sextet; m = multiplex. *NMR data from reference 17.

noticeable since an additional 10 minutes of irradiation (350 nm) left the spectrum unchanged, Figure 3-4b & c. Reverse isomerization (*cis – trans*) was observed after exposure to room light at different time intervals (spectra d, c, f, & g). Thermal reverse isomerization was obtainable as well after 5 min of heating at 100 $^{\circ}$C in the absence of light (spectrum h). Furthermore, under dark storage at room temperature for 16 hr, the TSUA ligand relaxed back to the more thermodynamically favored *trans* configuration surpassing the maximum absorption (364 nm) of the starting spectrum, (spectra i & a in Figure 3-4).

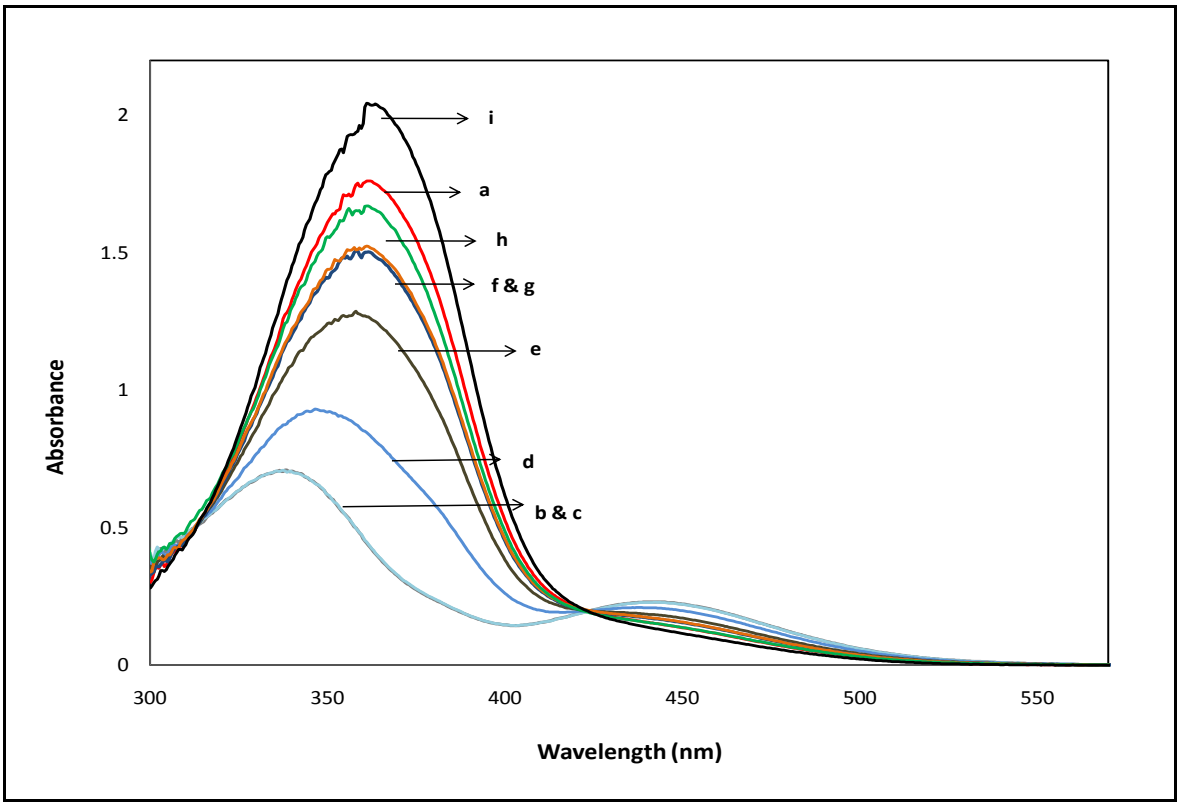

Figure 3-4. UV/Vis absorption spectra of a) TSUA in EtOH (28 µg mL^{-1}); b, c) after UV irradiation of (a) for 1 and 10 min; d, e, f, g) after room light exposure of (c) 3, 10, 40 min and 1 hr; h) after heating for 5 minutes at 100 ˚C; i) no light for 16 hr, respectively.

Evaluation and Characterization of Pore Morphology

Mesoporous materials were synthesized following the sol-gel technique outlined in reference 10a & b. Pore morphology was verified using XRD, BET, SEM, and TEM. Figures 3-5 thru 3-10 show the results of the aforementioned techniques for mesoporous standards (purchased from Sigma-Aldrich) and that of the synthesized films and powders. Standard mesoporous materials MCM-41, MSU-H, and HMS were analyzed for comparison against synthesized samples as well as confirmation of the evaluation methods. Shown in Figure 3-5 (top) is the XRD pattern for 1D-hexagonal pores. Conformation of the structure was verified by fitting a powder diffraction file of MCM-41 onto the sample XRD pattern, Figure 3-5 (top), inset. TEM images of MCM-41

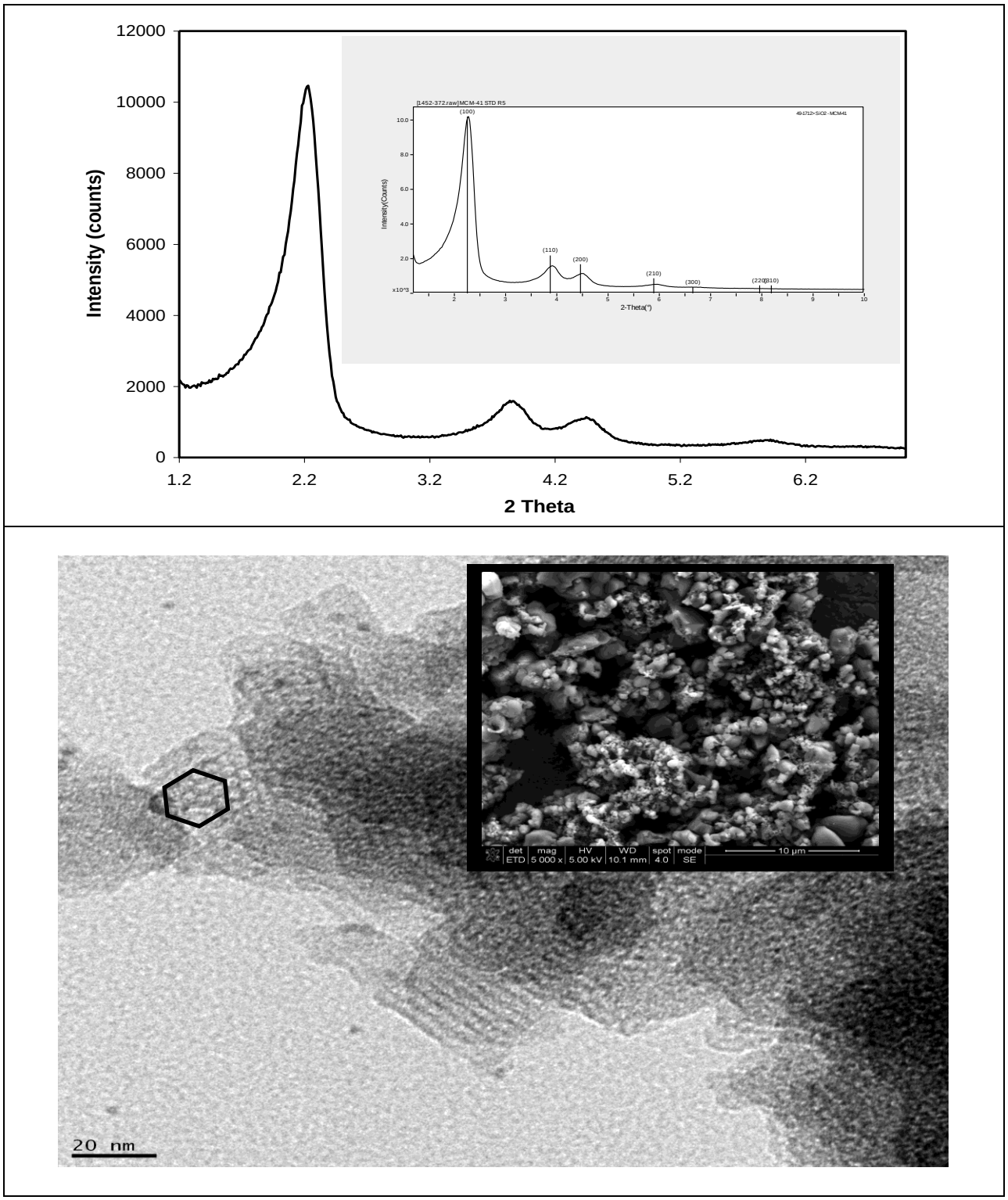

Figure 3-5. **(**Top to bottom**)** XRD pattern of MCM-41 powder (1D-hexagonal). Inset: XRD pattern of MCM-41 powder with indexed Powder Diffraction File (PDF). (Bottom) TEM image of MCM-41 powder. Outline (far left) shows the 1D-hexagonal structure for the pores. Inset: SEM image of MCM-41 powder.

show 1D-hexagonal pores with a pore diameter of ~2.86 nm, which is within the range provided by the manufacturer (2.3 – 2.7 nm), Figure 3-5 (bottom). Surface morphology and particle size was also visible via SEM showing small clustered particles within the range of 0.31 to 4.4 μm with irregular surfaces. MSU-H (2D-hexagonal) shows an X-ray diffraction pattern with a peak around $2\theta = 1.77^{o}$, Figure 3-4. SEM images show 2D-hexagonal tubes (~diameter 238 nm) protruding from all angles from the sample, Figure 3-6 inset. A broader XRD pattern was observed for HMS with a peak at $2\theta = 1.84^{o}$ along with SEM images showing small spherical particles (0.154 μm) clustered together into much larger aggregated masses on the order of a few microns (12.5 μm), Figure 3-7 and inset. Figure 3-8 (top) shows a broad XRD pattern for Sol1-2 powder with a peak around $2\theta = 1.47^{o}$. TEM images show channels/tubes shaped in a helical fashion with diameters of 10 nm, Figure 3-8 left inset; channels with other shapes (straight and irregular) were also observed, data not shown. SEM images show elongated particles within the range of 30 – 100 μm long with a jagged surface structure, as shown in Figure 3-8 right inset. BET measurements yielded a pore diameter of only 2.6 nm with a surface area of 107 m^2/g, and a pore volume of 0.07 cm^3/g, Table 3-2. Pore diameters are slightly smaller than what was expected (3.2 nm) as compared to PN films made by Liu *et al.*[10a, b]

However, given the estimated length of the TSUA ligand (~1.82 nm) in the *trans* position surrounding the central pore channel and the assumption that most of the pore's surface is covered by this ligand (see Figure 3-1), then the pore width could be as large as 6.2 nm, (5.6 nm in the *cis* position). Yet the actual pore size is probably somewhat less than calculated given that there is space between neighboring ligands that the absorbing molecule (N_2) can occupy.[10b] A low surface area and pore volume is also expected given that a good portion of the pore surface is covered by the azobenzene ligands as compared to empty pores, which show higher surface

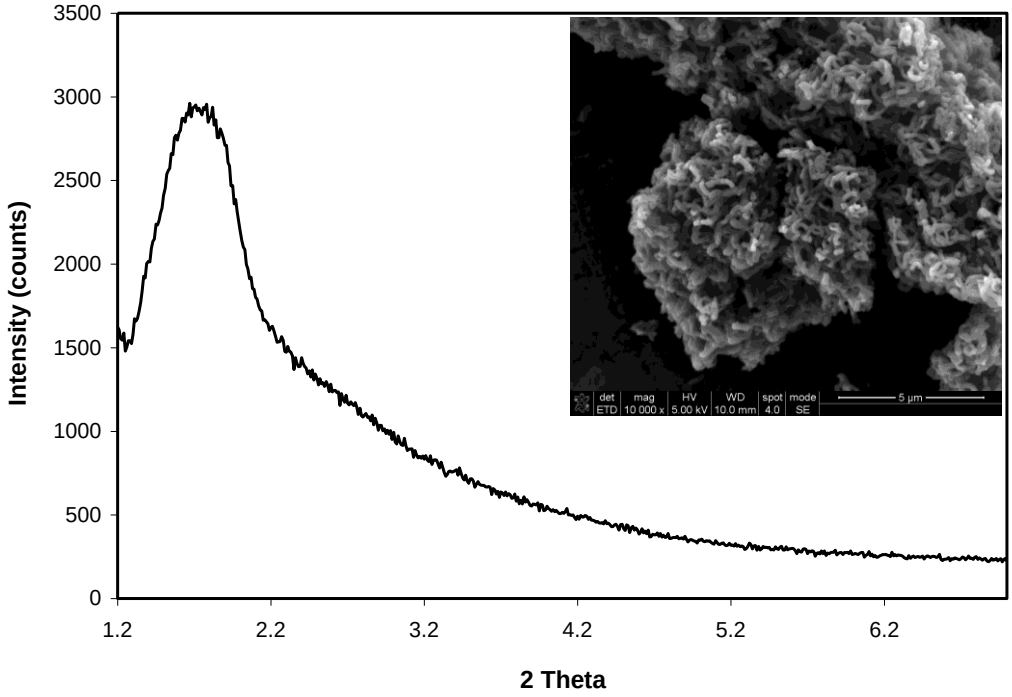

Figure 3-6. XRD pattern of MSU-H powder (2D-hexagonal). Inset: SEM image of MSU-H powder.

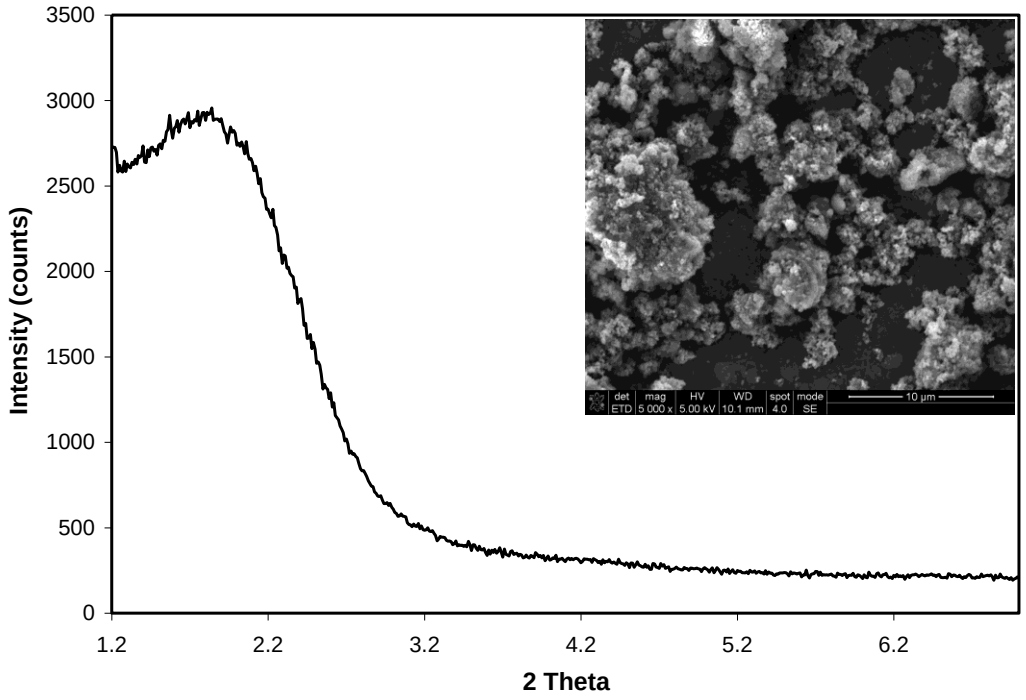

Figure 3-7. XRD pattern of HMS powder (wormhole); Inset: SEM image of HMS powder.

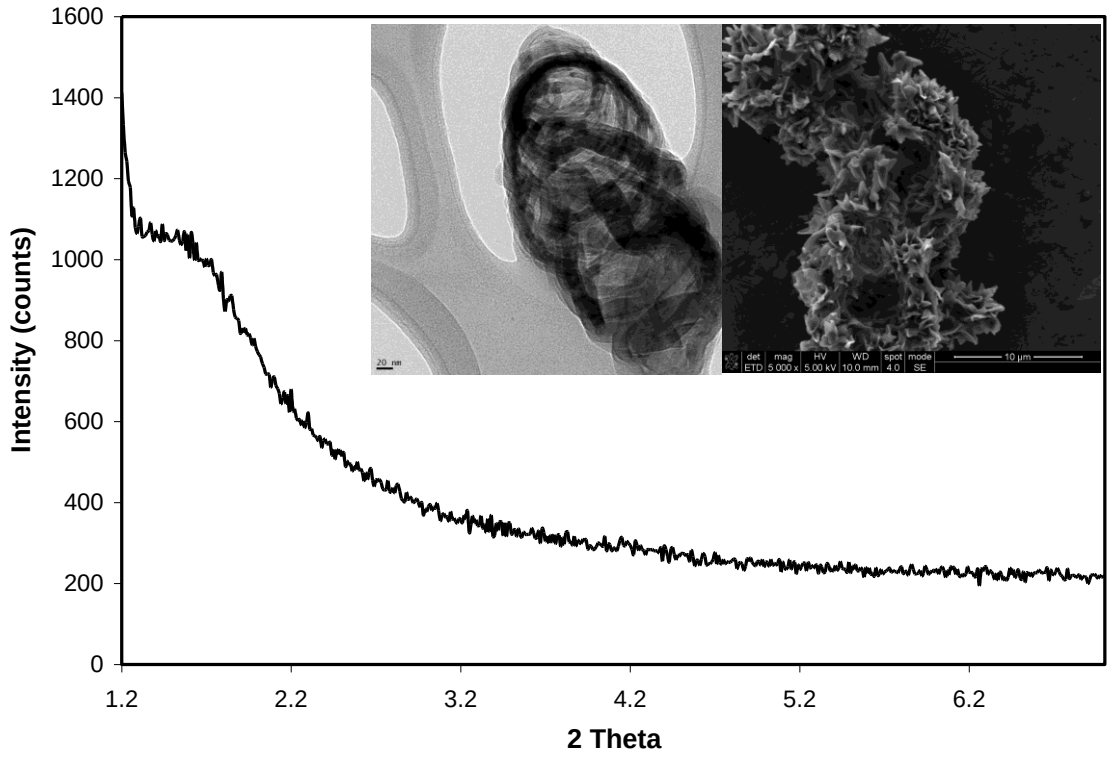

Figure 3-8. XRD pattern of Sol1-2 Powder. Inset (left to right) TEM and SEM image of Sol1-2 powder.

area and pore volume values such as the standards, Table 3-2. Sol1-3 powder shows a sharper XRD peak at $2\theta = 1.85^{o}$ as compared to the XRD of Sol1-2, shown in Figure 3-9 (top). SEM images show spherical particles a few microns (3.85 μm) in size along with larger aggregated irregular shaped particles on the order of 40 μm, Figure 3-9 inset (top). Also, observed via SEM were needle like particles (12.4 X 4.1 μm in size) that resemble crystals, data not shown. Sol1-3 particles (aggregates) show similar surface features to that of the HMS standard, Figures 3-7 and 3-9 insets. Further evidence that the pores are structured similar to that of HMS are TEM images, which show disordered tubes, ~12.5 nm in diameter, arranged in a wormhole like manner indicative of HMS like mesoporous materials, shown in Figure 3-9 (bottom). However, TEM images of HMS need to be performed to verify the exact pore structure for Sol1-3. BET analysis

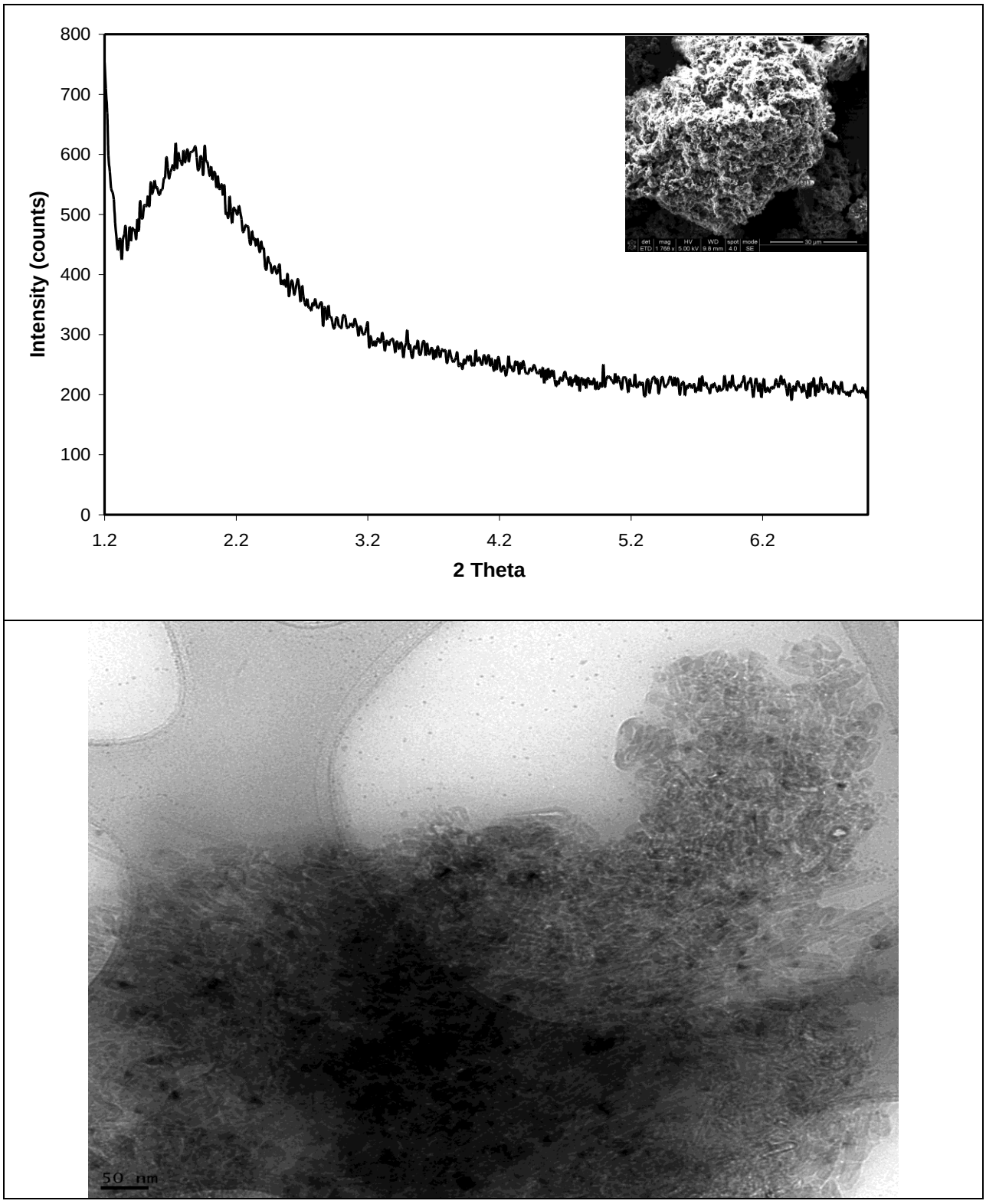

Figure 3-9. XRD pattern of Sol1-3 Powder. Inset: SEM image of Sol1-3 powder. (Bottom) TEM image of Sol1-3 powder showing wormhole like channels.

Table 3-2. Physical properties for mesoporous materials.

Sample	**Pore Width (nm)**	**Pore Volume (cm^3/g)**	**Surface Area (m^2/g)**	**Pore Structure**
MCM-41	2.3 – 2.7	0.98	1000	1D-hexagonal
MSU-H	7.1	0.91	750	large 2D-hexagonal
HMS	3.9	1.76	910	2D-hexagonal (disordered/wormhole)
Sol1-2 Powder	2.6	0.07	107	unknown
Sol1-3 Powder	2.5	0.12	108	*2D hexagonal (disordered)

* Based on TEM images.

estimates a pore width of 2.5 nm with a surface area of 108 m^2/g and a pore volume of 0.12 cm^3/g. Pore width, surface area, and pore volume are lower than expected and/or as compared to standards for the same reasons as explained previously. It has been reported that sol-gel mixtures with high water to silicate ratios take much longer to gel, thus allowing more time for micelles to form into structured/order shapes as observed in the TEM images for Sol1-2, Figure 3-8 (left inset).[20] However, materials made with lower ratios of TEOS to water (Sol1-3) gel much faster, thus impeding micelles from forming more ordered structures and alternatively yielding aggregated spherical particles, see Figure 3-9 (SEM image).

Mica substrates dip coated in the sol gel solution show a homogenous coating of the PN film onto the exposed mica surface, Figure 3-10 (top) inset. Sharp peaks at $2\theta = 1.97$ and 3.35 degrees in the XRD pattern demonstrate the high order of the enclosed pore structure, Figure 3-8

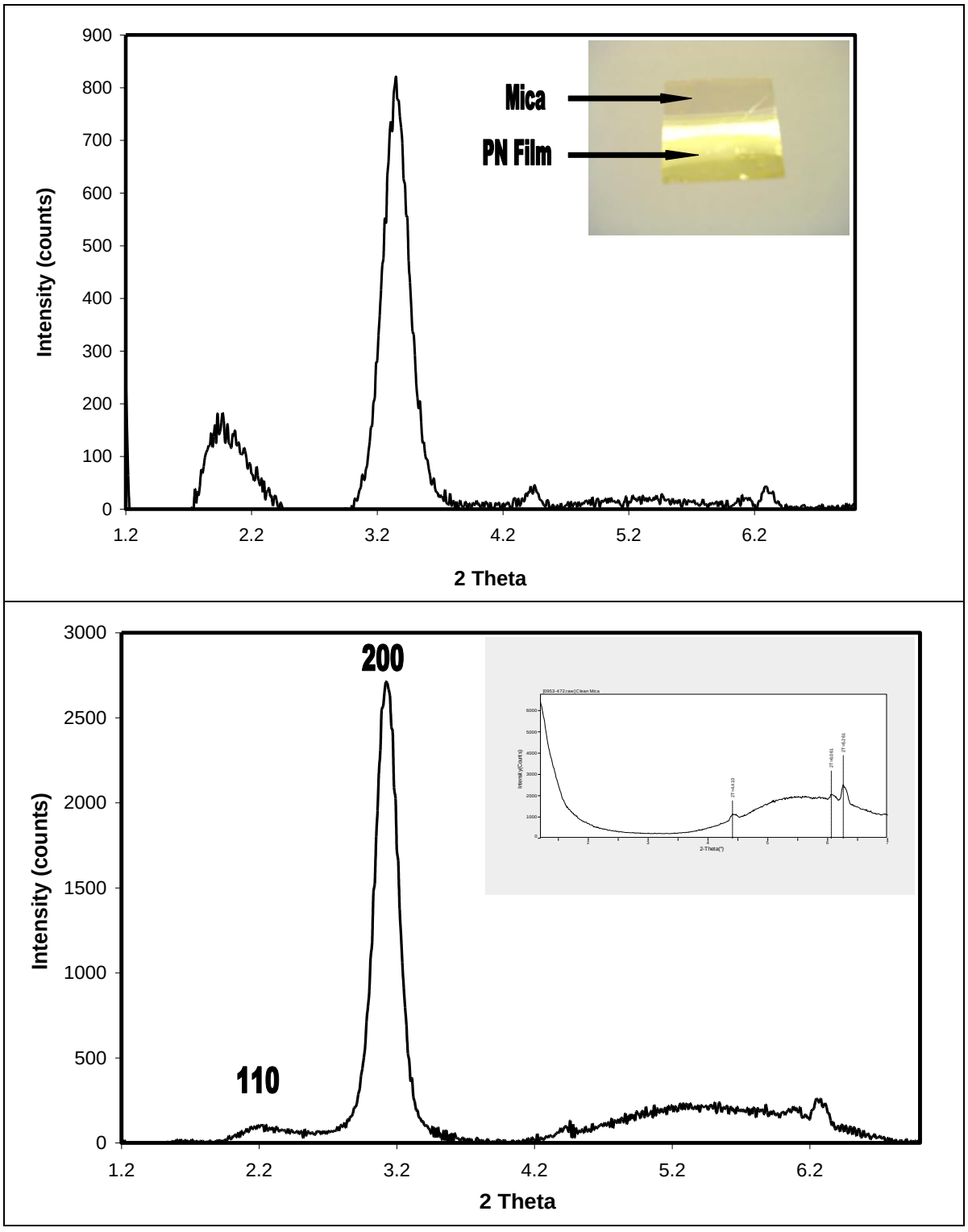

Figure 3-10. **(**Top to bottom**)** XRD pattern of a PN film dip coated onto mica. Inset: PN film dip coated unto a mica substrate. (Bottom) XRD pattern of a PN film spin coated onto mica with reflections at 3.98 nm (d_{110}) and 2.82 nm (d_{200}). Inset: XRD pattern of clean mica with diffraction peaks at $2\theta = 4.41$, 6.06, and 6.26 degrees.

(top). Peaks at $2\theta = 4.41$, 6.06, and 6.26 degrees in both XRD patterns for dip coated and spin coated films on mica are associated with the mica substrate, see Figure 3-10 (bottom) inset. Attempts to index the X-ray diffraction peaks for the dip coated films were unsuccessful. Spin coated films show a more intense XRD pattern with sharp peaks at $2\theta = 2.22^{o}$ (d = 3.977 nm) and 3.13^{o} (d = 2.820 nm), Figure 3-10 (bottom). Indexing of these peaks with the Bravais lattice fitting guide contained in the Rigaku software program, JADE, leads to a bcc structure with the first reflection as 110 and the second as 200 with a unit cell dimension of a = 5.63 nm (d_{200} = 2.82 nm), Figure 3-10 (bottom). Films made by Liu *et. al* showed reflections at 2.85 nm (d_{200}) and 1.4 nm (d_{400}), that were interpreted as corresponding to a bcc pore structure indexed as belonging to the Im3m space group with a unit cell dimension of a = 5.7 nm (d_{200} = 2.85 nm).[10a, b] Absence of the 400 reflection in the XRD pattern in Figure 3-10 (bottom) is understandable given that this peak would be visible at around $2\theta = 6.4^{o}$, which falls in the range of peaks associated with the mica substrate. Also this peak was very weak in the reference XRD pattern provided by reference 10b. The 110 reflection in Figure 3-8 (bottom) was not visible in the XRD pattern provided by Liu *et al.*, however it was detected with 2D grazing incidence small angle X-ray scattering (GI-SAXS) and electron diffraction.[10a, b]

Ligand Mobility for PN Powders and Films

Photoisomerization of the TSUA ligand within solid samples in the form of powders and films were monitored with UV-Vis spectroscopy (films) and in diffuse reflectance mode (powders), Figure 3-11. Powders and films show similar photochemical behavior for *trans – cis* isomerization under exposure to 350 nm light with that of TSUA in ethanol. In particular, spin coated films show the largest change in absorption during photolysis with 350 nm light, as

compared to dip coated films and powders, Figure 3-11(d). Furthermore, all samples relaxed back to the their predominately *trans* ($_p$*trans*) configuration after standing in the dark for 24 hrs; spin coated films converted back to their initial state ($_p$*trans*) in only a few hours, Figure 3-11(d). Sol1-3 (powder) showed a more resolved spectra at λ_{max} = 360 nm as compared to Sol1-2, Figure 3-11b compared to 3-11a.

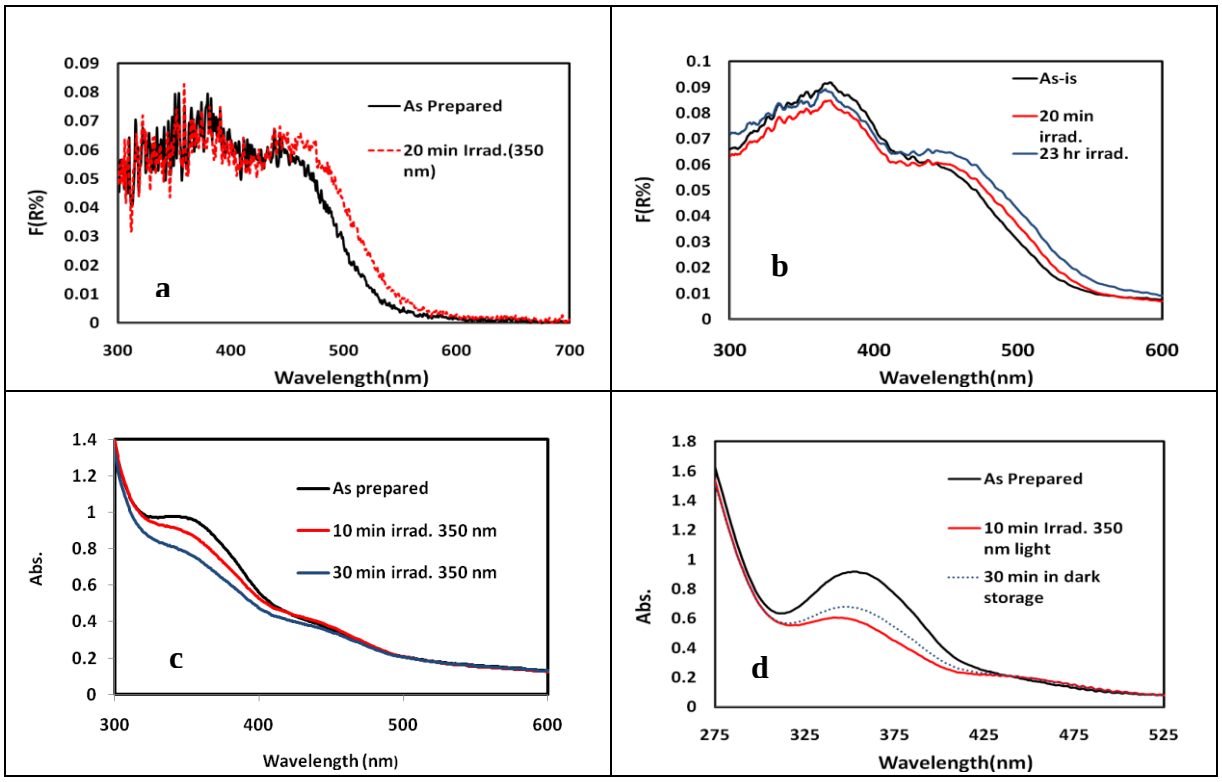

Figure 3-11. UV-Vis spectra (diffuse reflectance mode) of PN powders: a) Sol1-2 and b) Sol1-3. UV-Vis spectra of PN films synthesized via dip coated (c) or spin coated (d) onto mica.

The distorted spectrum of Sol1-2 most likely implies a smaller amount of the TSUA ligand is present in the pores as compared to Sol1-3. This is suggested given that 2~3 times more PN material had to be mixed with the dispersant ($BaSO_4$) to obtain a reflectance spectrum close to that of Sol1-3. Also, this particular sol-gel solution showed poor miscibility during mixing of the

sol-gel solution, which could have limited the number of the TSUA ligands able to enter the micelles.

UV-Vis Spectroscopy of TSUA in the Presence of CH_3NO_2

UV-Vis spectroscopy of TSUA/ethanol/NM solutions were conducted to identify key spectral shifts for the TSUA ligand (*trans* and *cis* configurations) in the presence of NM. As shown in Figure 3-12, curve a, TSUA in ethanol predominately in the *trans*

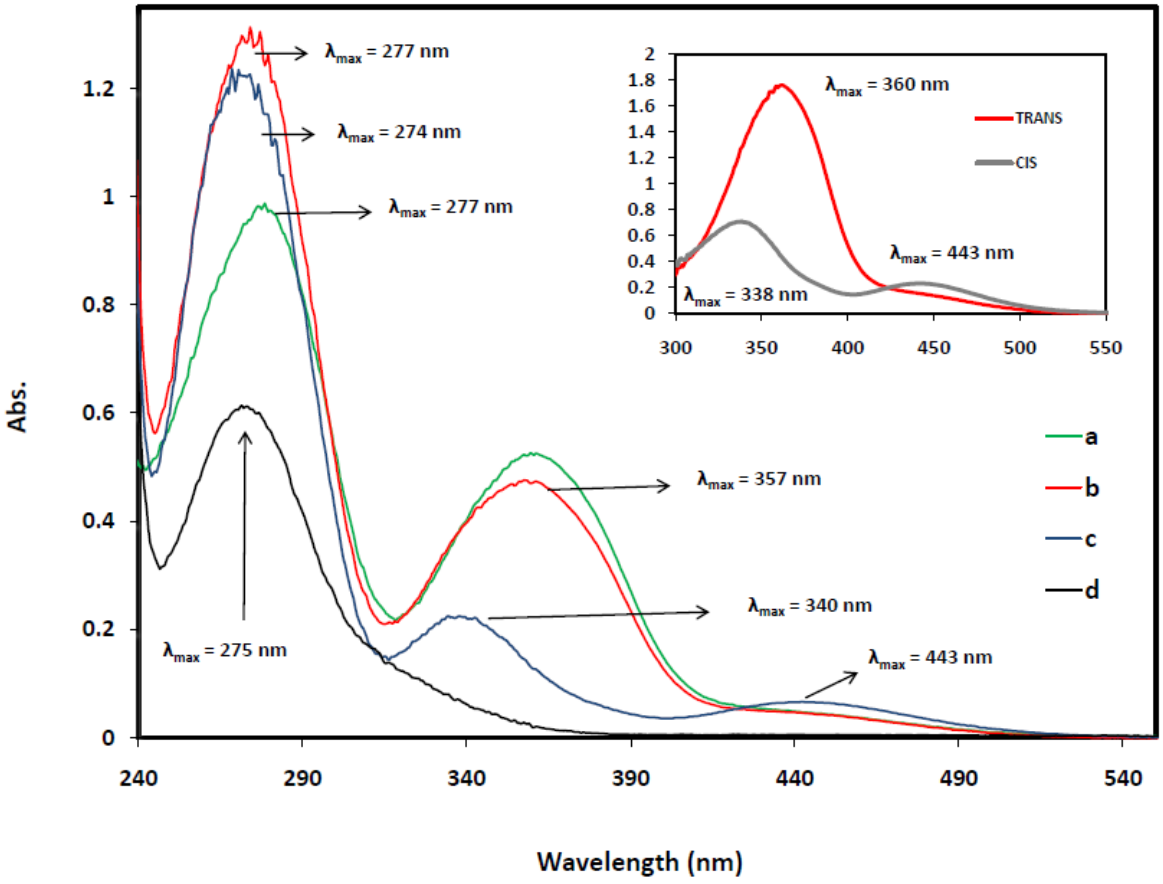

Figure 3-12. a) UV-Vis spectrum of TSUA in ethanol ($_p$*trans*); b) TSUA in ethanol with nitromethane; c) after 2 min of irradiation of (b) with 350 nm photons (predominately *cis* - $_p$*cis*); d) nitromethane in ethanol. Inset: UV-Vis spectrum of TSUA/ethanol, $_p$*trans* (λ_{max} = 360 nm); Later solution after 1 min of illumination with 350 nm photons, $_p$*cis* (λ_{max} = 443 nm and λ_{max} = 338 nm).

configuration with peaks at λ_{max} = 360 nm and 277 nm. Figure 3-10, inset, was obtained after 1 min of illumination of curve a with 350 nm photons showing peaks at λ_{max} = 338 nm and 443 nm, confirming isomerization to the *cis* configuration.

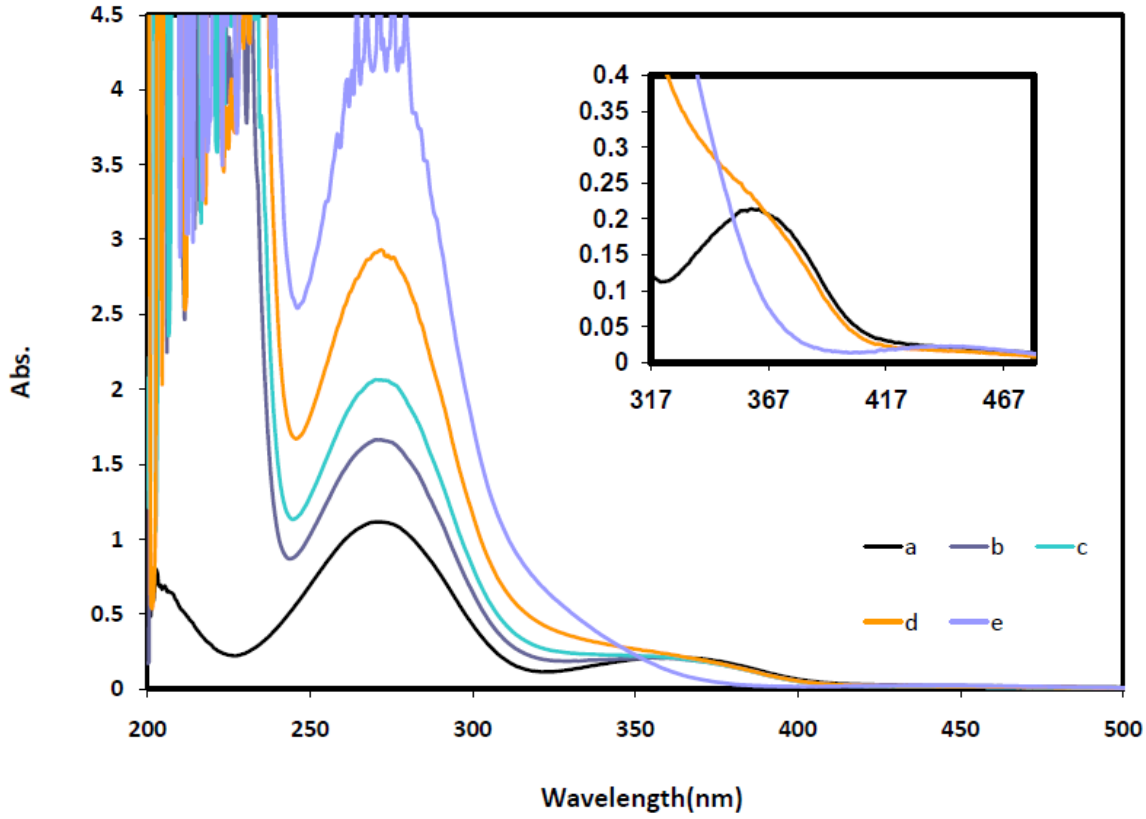

Figure 3-13. a) UV-Vis spectrum of TSUA in ethanol ($_p$*trans*); b, c, & d) after addition of NM to reach molarities of: 0.03 M, 0.11 M, and 0.2 M, respectfully; e) photoylsis of (e) with 350 nm light for 3 min ($_p$*cis*). Inset: UV-Vis spectra of (a), (b), and (c) between the wavelength ranges of 317 nm thru 467 nm.

Depicted in Figure 3-12 curve b is a spectrum of a TSUA/ethanol solution after addition of 0.4 mL of NM. Signals characteristic of the *trans* configuration (peak maxima at 357 nm and 274 nm) are observed as compared to TSUA/ethanol (λ_{max} = 360 and 277 nm). The data shows that in the presence of CH_3NO_2 TSUA ($_p$*trans*) undergoes a slight decrease in absorption and minor blue

shifts from 360 nm to 357 nm together with an increase in absorption and blue shift from 277 nm to 274 nm; compare curve a with curve b, Figure 3-12. On the other hand CH_3NO_2 shows a signal with λ_{max} = 272 nm, Figure 3-12 curve d. After 2 minutes of illumination with 350 nm photons of the TSUA solution in ethanol containing CH_3NO_2 isomerization of ($_p$*trans*) to the *cis* configuration takes place, Figure 3-12 curve c. Blue shifts at 338 nm to 335 nm and 274 to 271 nm were observed along with an increase in absorption intensity accompanying the latter shift; no spectral shift was noticed at λ_{max} = 443 nm.

Stronger solvent-like effects on the TSUA ligand in the *trans* position were observed at higher ratios of CH_3NO_2 to ethanol, see Figure 3-13 curves a thru d. At high NM concentrations the absorption by CH_3NO_2 with λ_{max} = 272 nm extends significantly to longer wavelengths. This NM absorption partially masks the optical signal of the ligand at 360 nm, which can now be detected only as a shoulder depicted in the inset of Figure 3-13. Upon photolysis with 350 nm light of solutions with the highest concentration of CH_3NO_2 in ethanol, the *cis* signal at λ_{max} = 335 nm is no longer identifiable as a distinct absorbance due to the contribution from CH_3NO_2, yet the *cis* signal at λ_{max} = 443 nm is still visible, Figure 3-13 inset.

Photochemical Control for the Mass Transport of CH_3NO_2: PN films

UV-Vis spectroscopy of spin coated PN films on mica (TSUA - $_p$*trans*) show a main peak maxima at 352 nm and, after irradiation with 350 nm light, two peaks at λ_{max} = 345 nm and λ_{max} = 444 nm for the *cis* configuration, Figure 3-14d. Immersion of the film in CH_3NO_2 for 7 h showed no changed in the optical spectrum (data not shown) suggesting that NM was not able to enter the pores within the films when the TSUA ligands existed preferentially in the $_p$*trans* configuration. Subsequently, the film was photolyzed with 350 nm photons for 14 h to produce

mainly ($_p$*cis*) and immersed in CH_3NO_2. Figure 3-14 shows the optical spectra as measured with immersion time in CH_3NO_2. Initially the TSUA ligand within the pores of the spin coated film relax back to the *trans* configuration from its photoinduced *cis* state at a rate of 0.002 O.D. $_{352\ nm}$ min^{-1} (2 h), Figure 3-14 curves a through e and inset. At longer immersion times in CH_3NO_2 the optical signal at 352 nm starts to decrease, then stabilize around 17 h, Figure 3-14 inset. This trend seems to suggest that small amounts of CH_3NO_2 are included within the pores of the films causing a slight decrease in the absorption at 352 nm, similar to the effect witnessed in Figure 3-12 curves a and b.

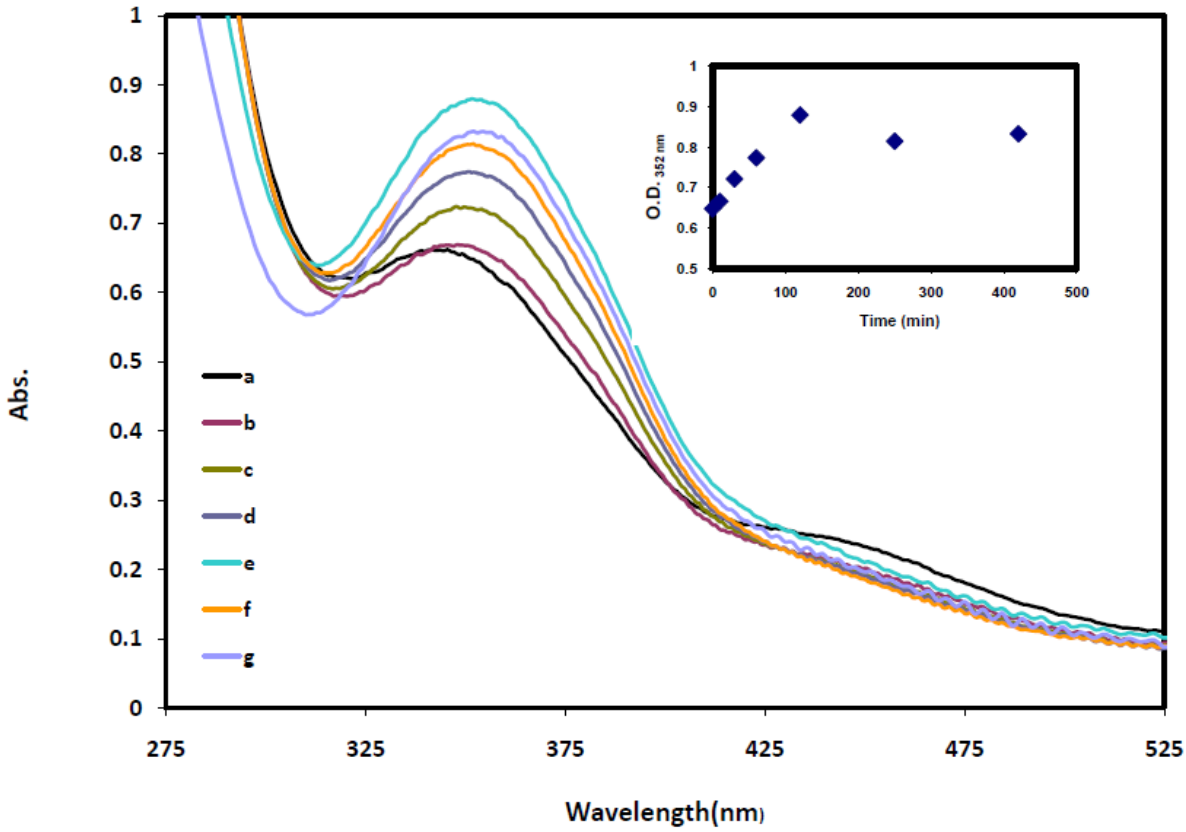

Figure 3-14. a) UV-Vis spectra of a spin coated film on mica after 14 h of irradiation with 350 nm light ($_p$*cis*); b, c, d, e, f, & g) after immersion in CH_3NO_2 for 10, 30, 60, 120, 250, and 420 minutes. Inset: plot of optical density at λ_{max} = 352 nm versus immersion time (min) in CH_3NO_2.

Subsequently the spin coated film in CH_3NO_2 was illuminated with 350 nm light and the optical signal at 352 nm decreased as expected, Figure 3-15 curves a and b. However, continued illumination at this wavelength shows a steady increase at 352 nm reaching a maximum absorption at 7 h at an initial rate of 0.002 O.D. $_{352\,nm}$ min^{-1}, Figure 3-15 curves b through e and inset. This unusual behavior of the ligand converting to the *trans* position instead of maintaining the *cis* position under illumination with 350 nm photons can be explained by an solvent-induced effect from CH_3NO_2 on the rates of isomerization from *cis* – *trans* or by formation of a charge-transfer complex.

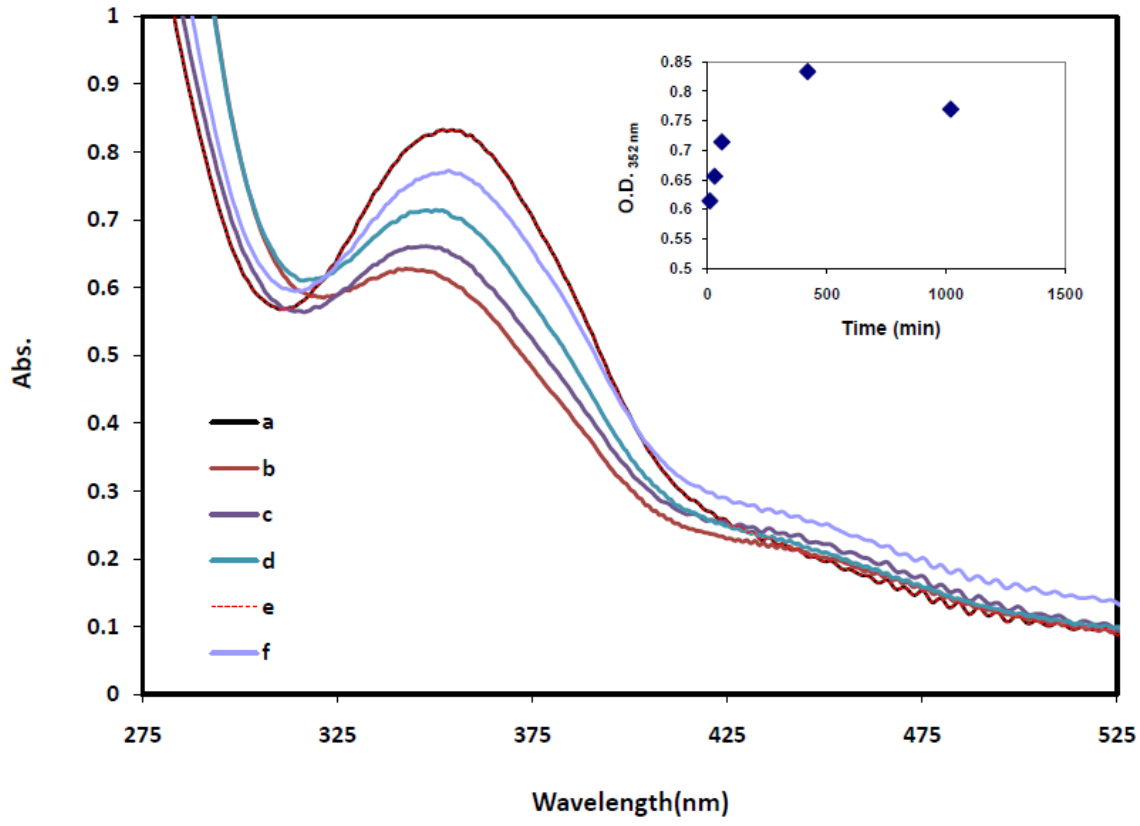

Figure 3-15. a) UV-Vis spectrum of a spin coated film on mica after 7 h immersion in NM; b, c, d, e, & f) after photolysis with 350 nm light while immersed in CH_3NO_2 for 10, 30, 120, 420, and 1020 minutes. Inset: plot of optical density at λ_{max} = 352 nm versus irradiation time (min) at 350 nm light while immersed in CH_3NO_2, starting from (b).

Azobenzene derivatives have been reported to incur significant solvents effects on their rates of isomerization from *cis* to *trans* in the presence of polar solvents by as much as a factor of 10^5.[22-24] Furthermore, at longer illumination times (17 h) the optical signal at 352 nm stabilizes suggesting that a photostationary point has been reached between the photoinduced *trans* - *cis* isomerization and that of the solvent induced *cis* - *trans* conversion, Figure 3-15 curve f and inset.

Inclusion/retention of CH_3NO_2 in PN Films

A "as prepared" spin coated film immersed in CH_3NO_2 under photolysis with 350 nm light for 15 h shows a noticeable shift in the optical signal at 352 nm, Figure 3-16 curves a and b, similar to effects witness at high CH_3NO_2 to ethanol ratios seen in Figure 3-13 curve a and d. This change in the optical spectrum strongly suggests that CH_3NO_2 has been loaded into the pores of the film. A similar experiment was performed with a dip coated film that was submersed in CH_3NO_2 and irradiated for 3 h with 350 nm photons then measured by ATR spectroscopy, Figure 3-17. IR signals (vibrations) for TSUA and nitromethane were identified; no signal for either compound was detectable before the inclusion of CH_3NO_2, again suggesting a solvent-like effect on the TSUA ligand in the presence of CH_3NO_2. The aforementioned spin coated film, loaded with CH_3NO_2, was removed from liquid NM and left to stand in the dark for 90 minutes, then measured with UV-Vis spectroscopy (data not shown). No noticeable change was detected in the optical spectrum for the spin coated film showing that the film had retained the CH_3NO_2 in the pores (data not shown). Experiments on dip coated films showed similar behavior with no change in the optical spectrum up to 5 days; only after placing the films in a vacuum oven under

heat (100 ^{o}C) does the optical spectrum appear similar to the 'as prepared" dip coated films before photolysis in CH_3NO_2 (data not shown).

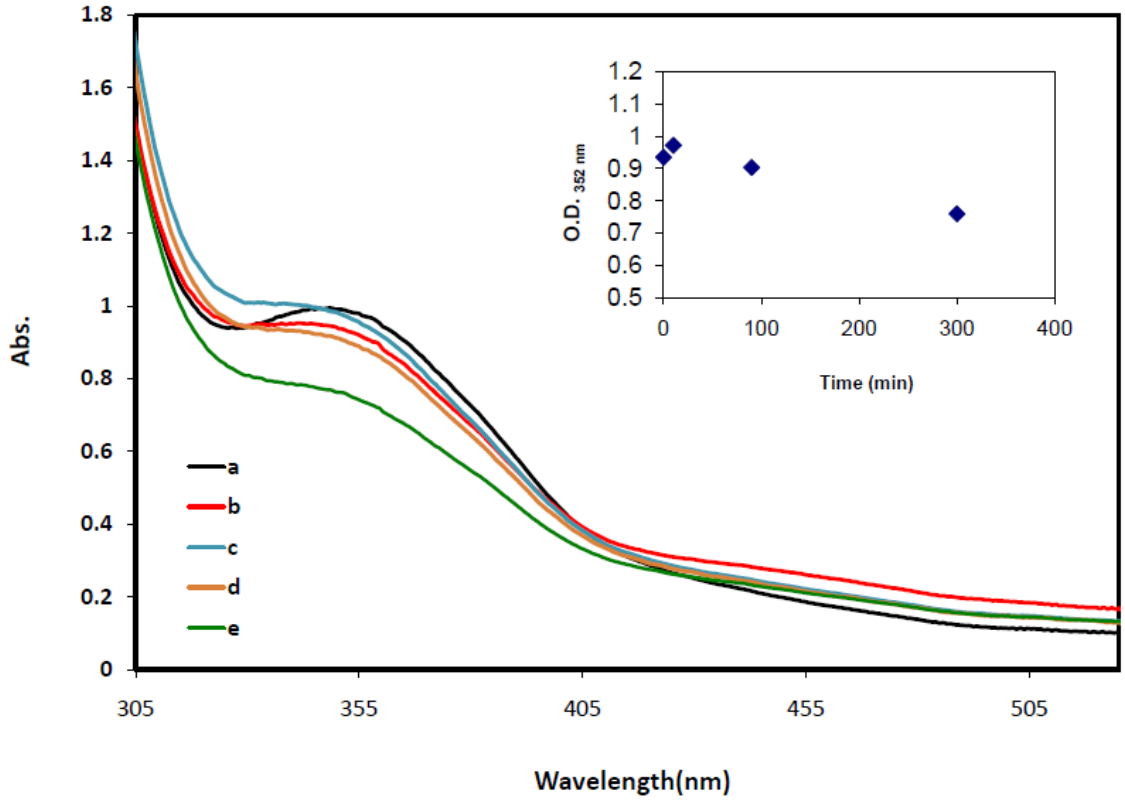

Figure 3-16. a) UV-Vis spectrum of a spin coated film on mica as prepared; b) after photolysis with 350 nm light while immersed in CH_3NO_2 for 15 h; c, d, & e) after irradiation of the film in air with 420 nm light. Inset: plot of optical density at λ_{max} = 352 nm versus irradiation time (min) with 420 nm light, starting with (b).

Ligand Mobility at Longer Wavelengths (420 nm) in the Presence of CH_3NO_2

A spin coated film loaded with CH_3NO_2 was illuminated with 420 nm light to monitor any ligand isomerization induced by irradiation at longer wavelengths, the results are presented in Figure 3-16 curves c, d, & e. Initial photolysis of the loaded spin coated films show an expected increase in absorption at 352 nm signifying that the remaining TSUA ligands in the *cis*

configuration isomerize to the *trans* state, Figure 3-16 curves a and b. However, at longer illumination times with 420 nm light the optical signal at 352 nm decreases (0.0007 O.D. $_{352\ nm}$ min^{-1}) indicating formation of the *cis* configuration, Figure 3-16, inset. This unexpected *trans* – *cis* isomerization path could be another solvent effect induced by CH_3NO_2 on the TSUA ligands existing within the pores of the films. The origin of the unexpected *trans* – *cis* isomerization reaction taking place under these conditions remains unclear. Nonetheless, this shows that the films can retain CH_3NO_2 for several hours if not days once removed from the liquid NM bath, and also that the azobenzene ligands are photoresponsive to longer wavelengths in the presence of CH_3NO_2.

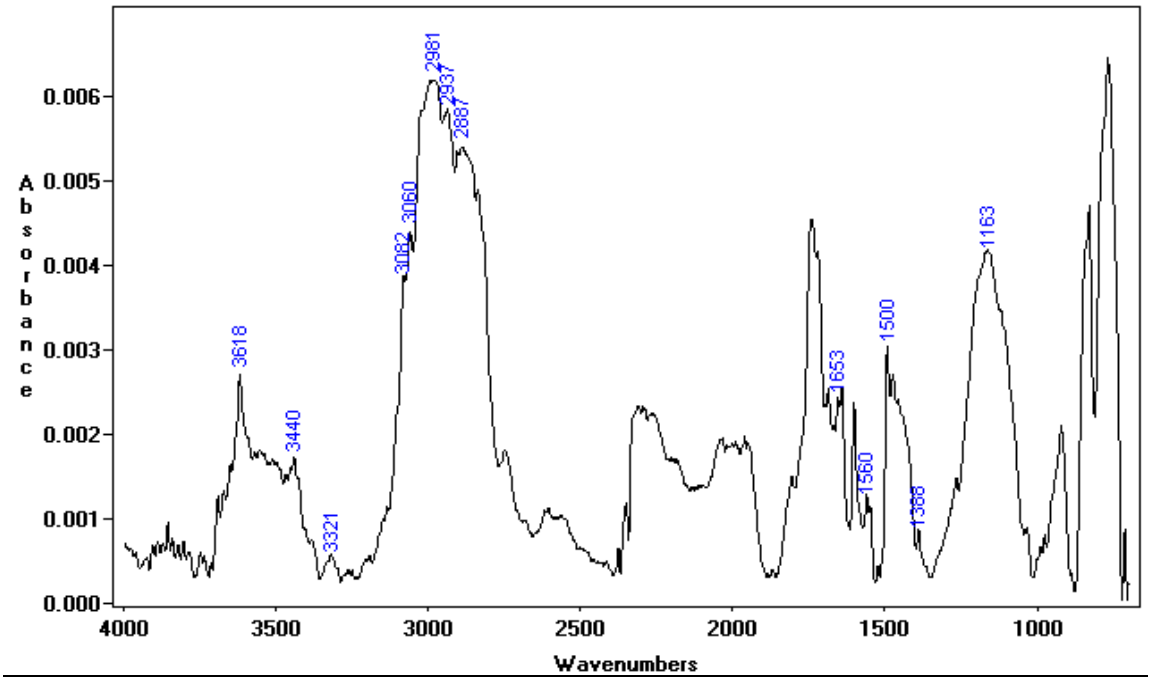

Figure 3-17. ATR spectrum of a photoresponsive nanoporous film dip coated onto a mica substrate that was immersed in CH_3NO_2 and then photolyzed with 350 nm photons for 3 h. Vibrations (cm^{-1}): Free alcohols or Si-O-H, $\nu_{R\text{-}OH}$ = 3618; TSUA, $\nu_{N\text{-}H}$ = 3440 & 3321; $\nu_{CH2\text{-}Ph}$ = 3082 & 3060; $\nu_{C\text{-}H}$ = 2981, 2937, & 2887; $\nu_{C=O}$ = 1653; $\nu_{C\text{-}C(AROMATIC)}$ = 1500; $\nu_{C=C(AROMATIC)}$ = 1163 Nitromethane, ν_{NO2} = 1560 & 1388.

Evaluation of Results for Sensitization Measurements

PN films (made via spin coating and dip coating) showed similar properties as those reported in reference 9a and 9b; spin coated films showed near identical properties. Mass transport control for the loading of CH_3NO_2 within the pore channels was observed under photolysis. In the absence of 350 nm light and when the ligands are in their more favorable *trans* position, inclusion of CH_3NO_2 within the pores of PN films was not witnessed. Furthermore, smaller amounts of CH_3NO_2 appear to flow into the pore channels at a much slower rate, as compared to illuminated PN films in CH_3NO_2, when the PN films are immersed in CH_3NO_2 and the ligands are initially in the *cis* position. In addition, ligands within the PN film's pores are photoresponsive to both wavelengths (λ = 350 and 420 nm) of light in the presence of CH_3NO_2. Retention/storage of CH_3NO_2 within the pores of films, once removed from solution, was observed for several hours. An unexpected observation was a solvent-like effect induced on the photoisomerization of the ligand in the presence of CH_3NO_2.

Results show that PN powders contain pore sizes of a few nanometers with disordered morphology, irregular particle size and shape; they appear to be less photoresponsive with respect to ligand photoisomerization as compared to PN films. Sol1-2 powder has poor ligand mobility as compared to Sol1-3 powder. At present, Sol1-3 appears more favorable for sensitization measurements based off its greater mobility of the TSUA ligand and higher yield of particles of similar size and shape containing pores with a similar morphology; albeit disordered (wormhole). Greater mobility of the TSUA ligand should translate into more effective filling of the central pore channels when immersed in CH_3NO_2. Particles of uniform size and shape are preferred because their regular features facilitate evaluation and modeling sensitization results. Similarly, uniform pore morphology should equate to reproducible mass transport properties

such as loading rates for the filling of CH_3NO_2 with in the pore channels. Sol1-3 powder, if administered as a sensitizing agent for CH_3NO_2 under standard conditions, will required that the additive particles are suspended in a CH_3NO_2 gel; increasing the viscosity of CH_3NO_2 is necessary or the particles will fall out of solution.[13] Ultimately, engineering of a truly dynamic sensitizing system will require that PN materials are freely suspended in CH_3NO_2 without the need of changing the viscosity of the solution (*i.e.* liquid → gel), which would hinder the pore filling process within the particles. Nanometer size PN particles would be ideal sensitizing additives for such a system, given that the ratio of unoccupied space (pore volume) to particle weight would be highest. Due to their lower density the particles are most likely to remain stabilized within liquid CH_3NO_2.

Conclusions

Results demonstrate a "lock and key" mechanism for loading CH_3NO_2 into the pore cavities via illumination with 350 nm photons for spin coated films on a mica substrate. In addition, loading of CH_3NO_2 can be performed in two ways: 1) photolysis of PN films immersed in CH_3NO_2; and 2) photolysis of PN films in air, followed by immersion in CH_3NO_2 for slower loading rates. However, illuminated films in the presence of CH_3NO_2 with 350 nm or 420 nm photons show reverse effects on the isomerization pathway which could present problems for control and/or selectivity of the ligand within the PN material for specific applications. Further investigations into this research should examine azobenzene derivatives that are less sensitive to polar solvents to gain greater control on the isomerization of the ligands in the presence of highly polar liquids. In addition, efforts to make free standing films (detached from the mica substrate)

should be pursued to verify mass transport results obtained in this study, which might be affected to some degree by the mica substrate.

At present, Sol1-3 powder seems reasonable for sensitization testing for the coalescence model. On the other hand, utilization of this material as an "on/off" safety switch will require a greater understanding of the solvent effects induced on the ligand in the presence of CH_3NO_2. Future efforts should be directed towards synthesizing smaller PN particles of uniform size with pore structure (bcc) similar to the one of spin coated films in efforts to correlate mass transport results for the inclusion of CH_3NO_2.

References

1) Fickett, W. *Am. J. Phys.* **1979**, 47, 1050-1059.

2) Tarver, C. M. *Shock Compression of Solids VI*; Springer-Verlag; New York City, NY: 2003, Chapter 10.

3) Milne, A. M.; Bourne, N. K. *AIP Conference Proceedings* 2001, 620 (*Shock Compression of Condensed Matter*, Part 2) pp. 914-917.

4) Engelke, R. *Phys. Fluids* **1983**, 26, 2420-2424.

5) Cartwright, M.; Lloyd-Roach, D.; Simpson, P. J. *J. Energy. Mat.* **2007**, 25, 111-127.

6) Zeman, S. *Struct. Bond* **2007**, 125, 195-271.

7) Field, J. E. *Acc. Chem. Res.* **1992**, 25, 489-496.

8) Borisenok, V. A.; Bel'skii, V. M. *Russ. J. Phys. Chem. B* **2008**, 2, 187-193.

9) Ramaswamy, A. L. *J. Energ. Mat.* **2006**, 24, 35-65.

10) a) Liu, N. G.; Dunphy, D. R.; Atanassov, P.; Bunge, S. D.; Chen, Z.; Lopez, G. P,; Boyle, T. J.; Brinker, C. J. *Nano Lett.* **2004**, *4*, 551-554. b) Liu, N. G.; Chen, Z.; Dunphy, D. R.; Jiang, B.; Assink, R. A.; Brinker, C. J. *Angew. Chem. Int. Ed.* **2003**, *42*, 1731-1734.

11) Reduner, E. *Nanoscopic Materials: Size-dependent Phenomena*; RSC Publishing, Cambridge, UK: 2006, chapters 6 and 7.

12) Spizer, D; Comet, M.; Baras, C.; Pichot, V. J. Phys. & Chem. of Solids **2010**, 71, 100-108.

13) Dattlebaum, D.; Sheffield, S.; Stahl, D.; Dattlebaum, A.; Trott, W.; Engelke, R. *Influence of Hot Spot Features on the Initiation Characteristics of Heterogeneous Nitromethane* (in press)

14) Sanchez, C.; Boissière, C.; Grosso, D.; Laberty, C. ; Nicole, L. *Chem. Mater.* **2008**, 20, 682-737.

15) Hoffmann, F.; Cornelius, M.; Morell, J.; Fröba, M. *Angew. Chem. Int. Ed.* **2006**, 45, 3216-3251.

16) Grosso, D. et al. *Adv. Funct. Mater.* **2004**, 14, 309-322.

17) Liu, N.; Dunphy, D. R.; Rodriguez, M. A.; Singer, S. Brinker, *J. Chem. Commun.* **2003**, 1144-1145.

18) Kruk, M.; Jaroniec, M. Chem. Mater. **2001**, 13, 3169-3183.

19) Jaroniec, M.; Solovyov, L. Langmuir **2006**, 22, 6757-6760.

20) Lin-Vien, D *et al. The handbook of Infrared and Raman Characteristic Frequencies of Organic Molecules*; Academic Press Inc, San Diego, CA: 1991, chapters 9 and 10.

21) Brinker, C. J. and Scherer, G. W. *Sol-Gel Science: The Physics and Chemistry of Sol-Gel Processing*; Academic Press, Inc., San Diego, CA: 1990, chapter 3.

22) Reichardt, C. *Solvent and Solvent Effects in Organic Chemistry*; VCH Publishers, New York, NY: 1988, chapter 5.

23) Wildes, P. D.; Pacifici, J. G.; Irick, G. I.: Whitten, D. G. J. Amer. Chem. Soc. **1971**, 2004-2008.

24) Schanze, K. S.; Mattox, T. F.; Whitten, D. G. *J. Org. Chem.* **1983**, 2808-2813.

IV. METALLIZATION OF HIGH STRENGTH FIBERS

Introduction

Polymer metallization is an area of intense activity due to the practical importance of the resulting materials. For instance, metallized polymer films play very significant roles in microelectronics, space and automotive technologies.[1] Metallization imparts useful properties to polymeric components of space vehicles and structures, including protection against degradation processes that can be severe in the harsh environment of low earth orbit.[2] In fact, material erosion together with electrostatic charging are problems that have hindered the realization of space tethers consisting of two masses connected via a flexible cable.[3] Tethers have long been considered promising propulsion systems and for specific applications the demands imposed on the physical properties of the flexible joining cables seem to be met by currently-available high strength fibers.[4] Interestingly, an earlier study showed that deposition of μm thick Cu/Ni coatings onto Kevlar® fibers, poly(p-phenylene terephthalamide), yielded conductive materials exhibiting good erosion resistance without affecting the mechanical strength of the polymer.[5] While these results suggested a route for achieving satisfactory tether materials based on the aramid fibers, the methodologies used for metal deposition remain unknown.

Metallized fibers have been of interest to the textile industry because of their practical use in heating and antibacterial garments,[5,6] and the appeal for such materials is increasing due to their relevance to "smart" textiles.[7] Intelligent textiles are those involving wearable electronic devices including processors and energy responsive fabrics,[8] but other possible technologies have been envisioned.[9,10] Conducting fibers for electromagnetic shielding were traditionally

obtained by means of metal vaporization and doping;[11] the former method has also yielded sensors based on metalized Kevlar monofilaments.[12] Electroless metal deposition has been frequently used to treat fibers due to the effectiveness of this procedure in the metallization of plastics.[13] This method has enabled preparation of conductive cotton fibers plated with Cu/Ni and also metallization of PBZT, poly(p-phenylenebenzobisthiazole), fibers with Ag.[14,15] Gold plating on polyacrylonitrile (PAN) fibers has been accomplished at room temperature with an electroless Au(I) thiosulfate bath.[16] Analogous procedures operating at higher temperatures enabled plating of polycarbonate fibers with Au, Cu and Ni.[17] Metallization of aramid fibers has been reported to occur after activating them with a combination of bases and Ag.[18]

Reported here are results from an investigation that employed electrochemical methods for metallization of Kevlar fibers with Au. The aim was to achieve reproducible metallization of Kevlar yarns because this material exhibits physical properties (such as tensile strength to weight ratio) suitable for some tether applications.[4] Selection of gold seemed logical given that this metal is not affected by the corrosive space environment.[2b] Several electrochemical and electroless plating procedures were tested, among them, recently proposed methods that are cyanide-free.[19] Metal plating utilized Ni coated fibers as electrodes that were prepared via conventional metallization procedures for plastics.[13] Electrochemical Au deposition by means of a thiosulfate bath yielded the best results, producing conductive yarns exhibiting significant mass increases, negligible loss of flexibility and modest decreases in fiber tensile strength.

Experimental

All chemicals were used as received from the manufacturers; deionized water obtained from a Barnstead D7401 purification system was employed to prepare all solutions. KCl, $CHCl_3$,

$SnCl_2 \bullet 2H_2O$, NH_4Cl, KOH and NH_4OH were supplied by Fischer whereas $NiCl_2 \bullet 6H_2O$, $Na_3Au(S_2O_3)_2 \bullet xH_2O$ and anhydrous citric acid were from Alfa. Aldrich supplied hexane, K_2PdCl_4 and $NaH_2PO_2 \bullet H_2O$; L-ascorbic acid was from J.T. Baker, CH_3OH was obtained from Aater, and Kevlar 49 yarn was provided by DuPont.

Experiments were conducted on samples of Kevlar yarn cut to lengths of 9 and 25 cm, then tied at one end with a knot to prevent the separation of the individual fibers. All Kevlar materials were rigorously cleaned via immersion in an ultrasonic bath containing first CH_3OH, then hexane and finally $CHCl_3$. In each of these steps the polymeric materials were exposed to ultrasound for 10 minutes and then air-dried. Metallization experiments for electroless coated yarn were performed in water-jacketed glass containers (25 cm in diameter, 15 cm depth), which allowed control of the reaction temperature. Electrochemically coated yarn was metallized in clean open containers (beakers, petri dish) at room temperature. After every chemical step described below, the resulting fibers were rinsed with deionized water and air-dried. Adhesion of coatings was tested via a 10 min exposure to ultrasound of treated yarn immersed in water to dislodge any metal not firmly bound to the fiber surface. Occasionally, the results were confirmed using the adhesive tape test.[20]

Pretreatment of the fiber surfaces involved first a 1 min immersion of clean fibers in an aqueous solution containing 1 g/L of $SnCl_2 \bullet 2H_2O$, followed by exposure to a solution containing 2 g/L of $PdCl_2$ and 0.84 g/L of KCl for the same amount of time. This two-step process lasted about 5 min The third pretreatment step consisted of electroless Ni plating, which was conducted by immersing the sensitized Kevlar fibers for 5 minutes in a nickel bath that contained 30 g/L $NiCl_2 \bullet 6H_2O$, 60 g/L citric acid, 10 g/L $NaH_2PO_2 \bullet H_2O$ and 50 g/L NH_4Cl. This solution exhibited a natural pH of 9 – 9.4 and plating took place at 60 ºC.

Electrochemical Au metallization occurred via polarization of Ni-coated fibers submersed in an Au bath containing 6.3 g/L $Na_3Au(S_2O_3)_2 \bullet xH_2O$, 19.8 g/L sodium L-ascorbate, 15.2 g/L citric acid and 11.2 g/L KOH. Alternatively, a commercial gold cyanide bath from SMC Inc. (of proprietary composition) was also employed, diluted by a factor of ten with water yielding best results. The fibers functioned as cathodes whereas the anode consisted of a Pt mesh wire and a saturated Ag/AgCl electrode served as the reference. Electrochemical depositions were controlled by means of a BAS CV-27 potentiostat. For comparison, a few experiments were conducted in which Ni-plated fibers were subsequently metallized with an electroless Au deposition procedure described in the literature.[16] In this method the Au bath consisted of a solution with 25.5 g/L $Na_3Au(S_2O_3)_2 \bullet xH_2O$, 19.8 g/L sodium L-ascorbate, 15.2 g/L citric acid and 11.2 g/L KOH. The reaction was carried out at room temperature and immersion times ranged from 3 – 30 minutes.

Coated fibers were characterized in terms of mass gain and conductivity. Mass changes were monitored throughout the coating steps with an analytical balance. The resistance of treated fibers was measured by means of the two-point method using a digital ohm-meter from IET Labs model LOM 4000; stretched samples were used to ensure consistency in the analysis. Power output for coated fibers was quantified on an electrochemistry workstation with a modified AFRDE4 Bi-Potentiostat (Pine Instrument Co.) set to galvanostatic mode with the output I-V curves plotted with a BAS X-Y recorder. The current was stepped ~ 5-10 mA/s while measuring both current passed and voltage dropped across the fiber. An Instron 1122-4400R test machine served to determine the tensile strength of coated and uncoated fibers. Surface morphology was examined with optical microscopy, scanning electron microscopy (SEM) and transmission electron microscopy (TEM). For fibers plated with electroless

methods, SEM measurements were performed on a Zeiss DSM 940 microscope equipped with an EDS detection system. Specimens were prepared by immobilizing yarn in plastic pipettes, followed by sectioning the fibers at the pipette tip with a knife and sputter-coating with Au to avoid charging effects. Yarn plated electrochemically was analyzed with a Zeiss EVO 50 VPSEM; these conducting materials needed no additional coating and specimens were prepared by pressing metallized fibers onto C-coated tape. TEM analysis was carried out on a Zeiss EM 10CR instrument using 95 nm thick slices of fibers prepared via microtoming. X-ray diffraction (XRD) measurements employed a Bruker Smart APEX CCD diffractometer using a Mo K(α) radiation, λ = 0.071 nm, or a Rigaku Miniflex instrument using Cu K(α) radiation, λ = 0.154 nm.

Results and Discussion

Metal deposition on yarns involves chemical transformations taking place on the fiber surface. Thus, the presence of impurities on the fiber surface was anticipated to affect the efficiency of the plating processes. Shown in Figure 4-1 is an SEM image of "as received" Kevlar fibers that were not subjected to cleaning. An average fiber diameter of 12 µm was estimated from this image. Figure 4-2 depicts an SEM image of fibers subjected to the cleaning procedure described above. The flattened and deformed fiber top ends resulted from the sectioning procedure used to prepare the samples. Comparison of the two images reveals that the cleaning procedure yields smooth fiber surfaces free of the contaminants (seen as irregular objects) that are observed in the case of "as received" yarns. A slight decrease in the average fiber diameter to 11.2 µm is noticeable after the cleaning step. Presented in Figure 4-3

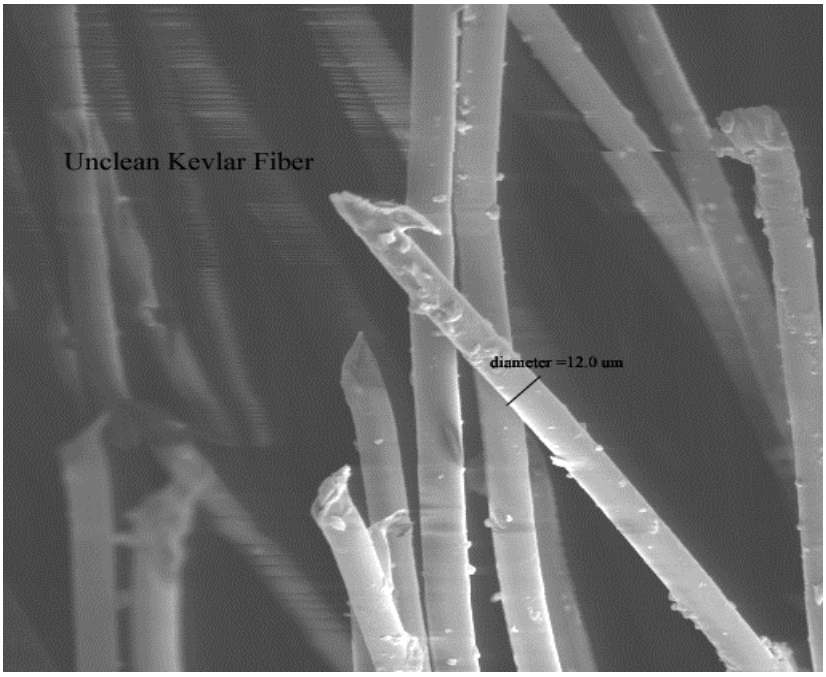

Figure 4-1. SEM image of sectioned “as received” Kevlar fibers.

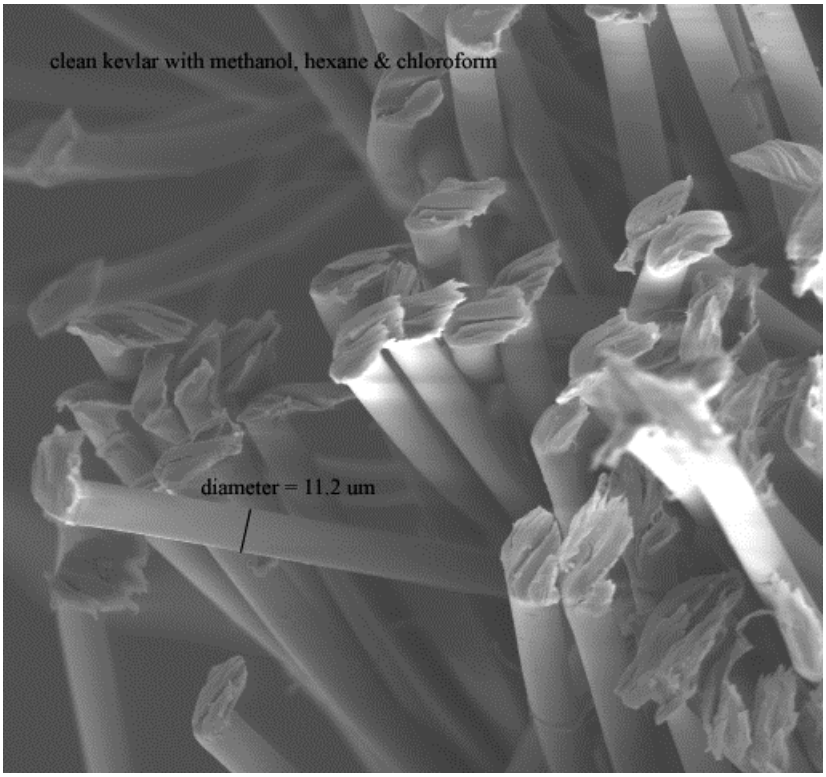

Figure 4-2. SEM image of clean Kevlar fibers after sectioning.

is the data obtained after exposing cleaned Kevlar fibers to Cu K(α) radiation. The intense peaks at 2θ values of 20.3 and 22.6 degrees agree well with the signals (20.6 and 22.8) reported previously,[21] which have been assigned to equatorial scattering of X-rays by the fiber material. Considering that the fibers were positioned perpendicular to the radiation beam, the predominance of signals originating from radial scattering of X-rays in our experiments is not surprising.

All metal depositions were performed with clean fibers in order to avoid the erratic and inefficient plating that resulted when impurities were not rigorously eliminated from the yarn surfaces.

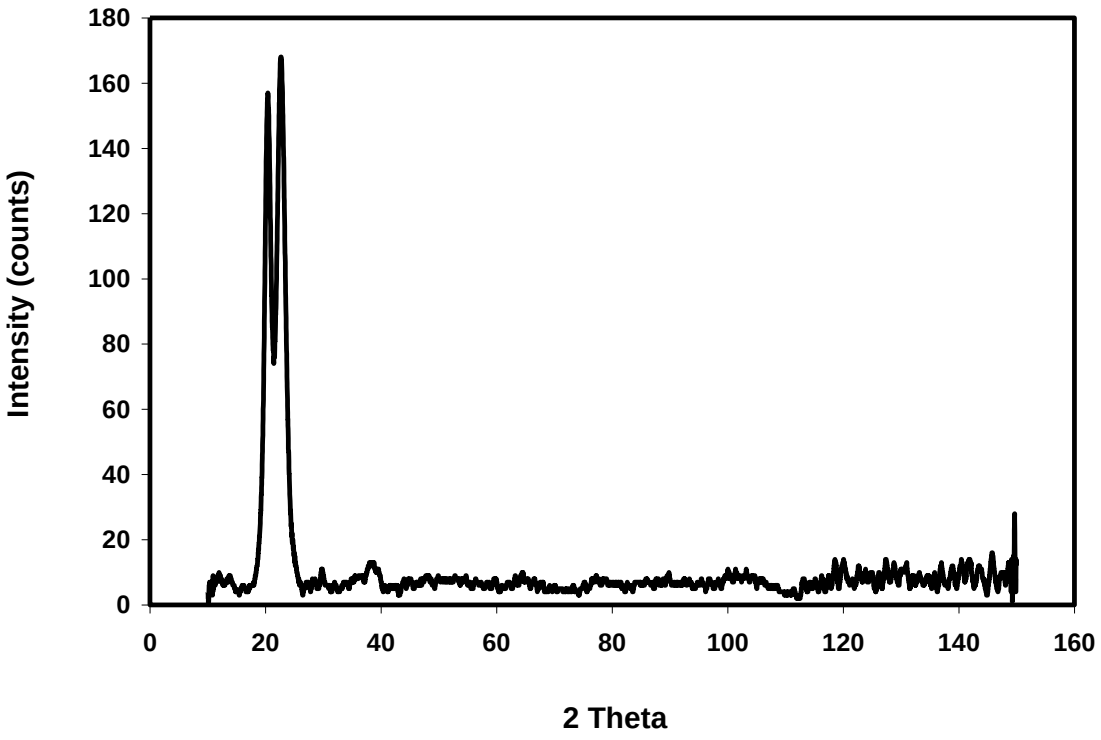

Figure 4-3. Diffractometer trace of clean Kevlar fibers exposed to Cu K(α) radiation.

Coated samples were selected for characterization and further treatment by examination of color changes since fibers coated with the Ni electroless method display a dark-gray coloration whereas Au coatings are bright red. Failed experiments were those producing non-uniform plating, or brittleness resulting in flaking of the metal coating. Polymeric materials such as Kevlar are devoid of surface groups able to bind metal ions and require pretreatment (surface activation) to create nucleation sites that enable metal attachment.[13] Surface activation is believed to involve binding of Sn(II) ions to the surface of the polymeric material, followed by deposition of Pd particles,

$$Sn^{2+} + Pd^{2+} \rightarrow Sn^{4+} + Pd \qquad (1)$$

Attempts to quantify gravimetrically the amounts of Sn and Pd present on the fiber surfaces were unsuccessful. Small Pd particles derived from this process are thought to catalyze the electroless Ni deposition since plating was successful only when the fibers were subjected to surface activation. Immersion of surface-pretreated Kevlar yarn into the Ni electroless bath for 5 min induced uniform darkening of the fibers together with evolution of numerous bubbles believed to be H_2 gas.[13] Removal of the bubbles from the fiber surface using glass rods promoted the plating process. Depicted in Figure 4-4 is an image of the resulting material; the coating is clearly noticeable particularly at the fiber tips. Significant damage to the coatings, including fracturing, was induced by the sectioning procedures employed during preparation of the SEM samples. On average, a single Ni plating step increases the fiber diameter to about 12 μm and the yarn mass by about 14% but larger changes occurred sporadically. EDS measurements conducted on plated fibers detected Ni together with low amounts of Sn and Pd.

While the coatings appear uniform in Figure 4-4, examination of longer fiber segments revealed the presence of uneven deposits and of places on the surface of the polymeric materials that remained uncoated.

Earlier metallization studies using electroless Ni baths containing hypophosphite ions have reported the formation of mixtures of materials including metallic nickel.[13] For this reason, the nature of the coatings was investigated by means of XRD.

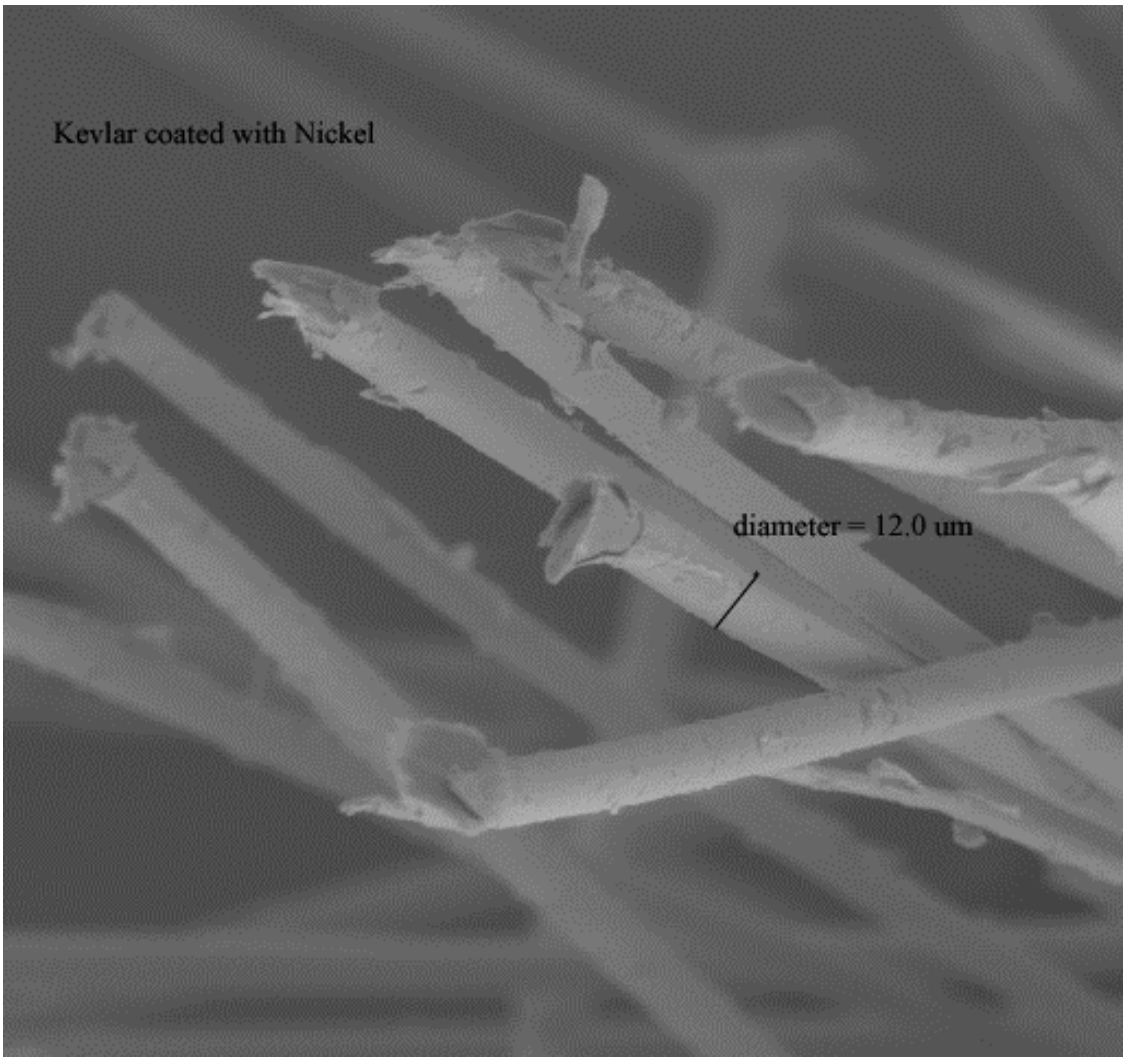

Figure 4-4. SEM image of sectioned Kevlar fibers coated with a single treatment of electroless Ni deposition.

Data represented with a continuous line in Figure 4-5 were obtained from fibers coated with the electroless Ni bath. Reflections at 2θ = 40, a "doublet" with maxima at 44.5 and 46.6 º, as well as signals at 68.2 and 82.1 degrees were detected together with the strong fiber signals at lower angles shown in Figure 4-3. Weaker peaks were also observed at 2θ = 86.4, 105.2, 119.7, and 125.2 degrees in Figure 4-5. The broken line in Figure 4-5 shows a pattern obtained after grinding coated fibers to a fine powder. Essentially the same reflections resulted in both cases, except that the low angle signals due to scattering from the fibers are absent in the powder case.

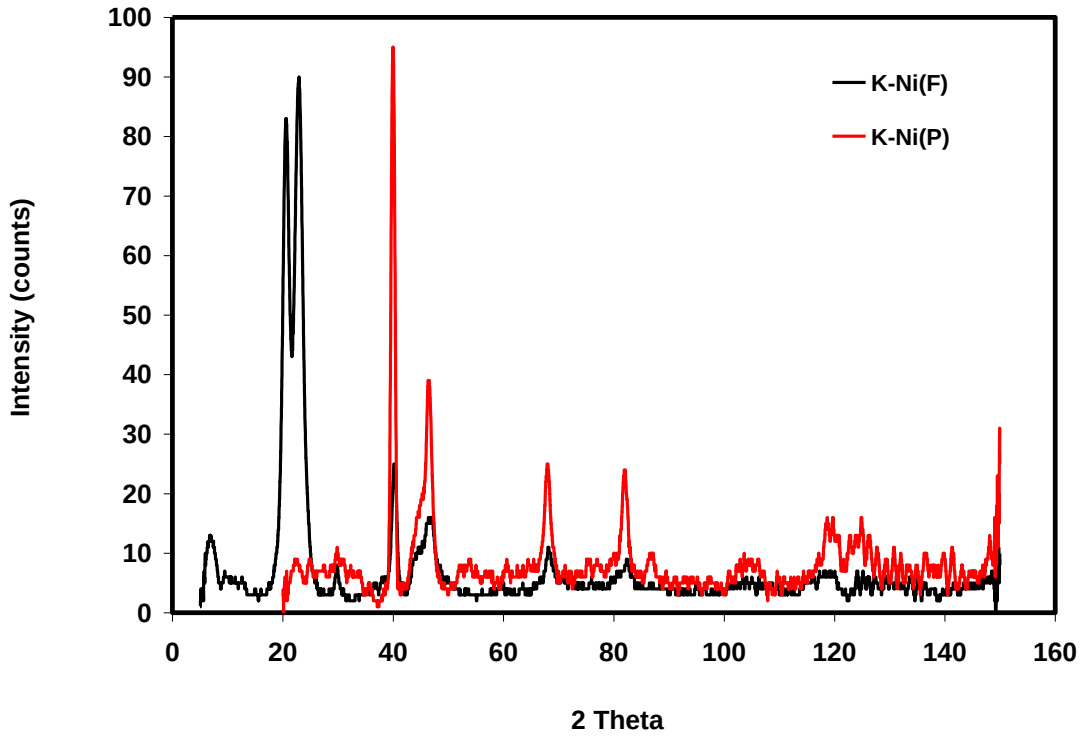

Figure 4-5. XRD signals obtained using Cu K(α) radiation of Kevlar fibers coated with nickel, K-Ni(F), and of powdered fibers coated with Ni, K-Ni(P).

Also, the intensities of the reflections are higher for the powder because this material exhibits a larger surface area than that of fibers. While the signal with a maximum of 44.5 degrees that is part of the doublet may be interpreted as corresponding to diffractions from the {111} planes of metallic Ni, none of the other anticipated diffractions from the {200}, {220} and {311} crystallographic planes (2θ = 51.8, 76.3 and 92.9 º, JCPDF card 4-0850) were detected.

Electroless Ni plating is known to yield some metallic Ni and also amorphous phosphides (Ni_xP_y) that crystallize upon annealing at high temperatures to form Ni_2P, Ni_3P and $Ni_{12}P_5$.[22-25] Attempts to match the diffraction data of the phosphides with the signals at 2θ > 35 degrees shown in Figure 4-5 were unsuccessful. However, the data match well the diffractions from metallic (fcc) Pd located at 2θ = 40.1, 46.7, 68.1 and 82.1 degrees arising from the {111}, {200}, {220} and {311} planes, (JCPDF card 46-1043). Even the weaker signals shown in Figure 4-5 can be indexed as Pd reflections from the {222}, {400}, {331} and {420} crystallographic planes (2θ = 86.6, 104.8, 119.3 and 124.6 º). Furthermore, the "doublet" can be identified as composed of reflections from Ni {111} planes at 44.5 degrees and a stronger peak at 46.6 degrees due to diffractions from Pd {200} planes. Detection of metallic Pd confirms the occurrence of reaction 1 and the low intensity of the XRD data is consistent with EDS results indicating that only small amounts of palladium are present on the fiber surfaces. Metallic Ni is clearly a minor product of the electroless process, which yields mainly amorphous materials, presumably Ni_xP_y phases.[22-25] Electroless Ni deposition using a hypophosphite bath has been rationalized in terms of:[13]

$$Ni^{2+} + 2H_2PO_2^- + 2H_2O \rightarrow Ni + 2H^+ + 2H_2 + 2HPO_3^{2-} \qquad (2)$$

The results of the present study indicate that reaction 2 fails to accurately represent the overall deposition process since metallic Ni and H_2 are just side products.

TEM images of a microtomed Kevlar fiber coated via the Ni electroless deposition method are presented in Figure 4-6. Dark areas corresponding to deposited materials denser than the polymeric matrix, which are not penetrated by the electron beam, and were detected only on the fiber surface. Powder TEM samples derived from the plated fibers were suitable for imaging the surface coatings.

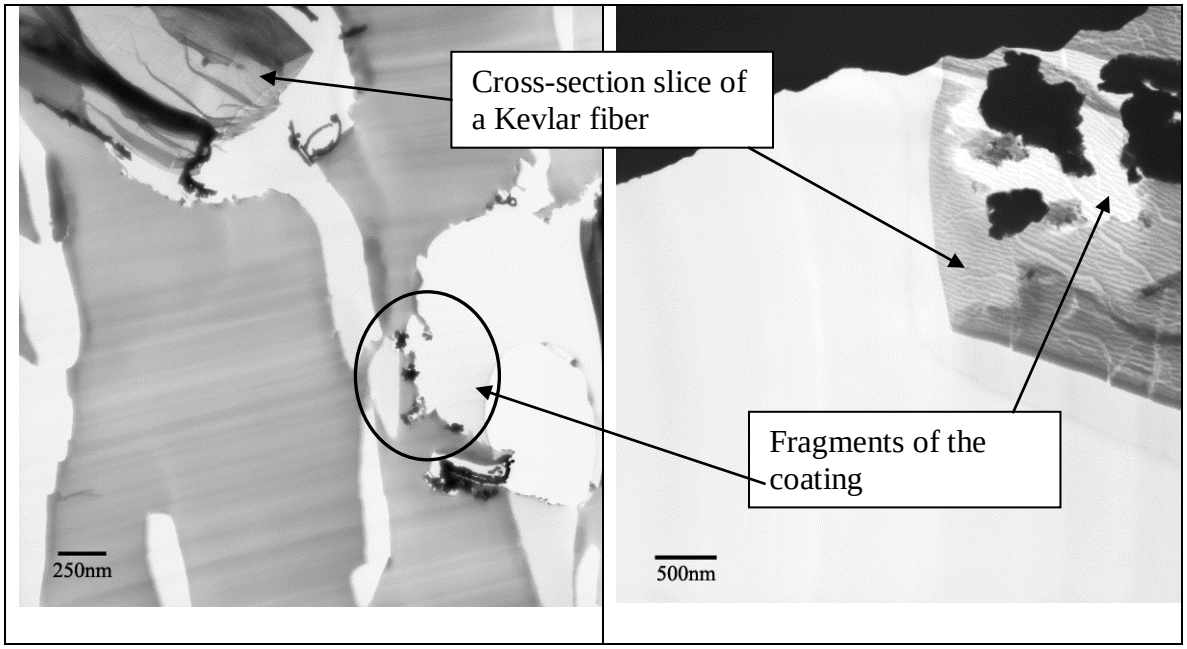

Figure 4-6. TEM images of cross-sectioned slices of a Kevlar fiber plated using Ni electroless deposition.

Presented in Figure 4-7 are images obtained at different magnifications from a surface fragment of a plated fiber measuring several μm. Large irregular objects with dimensions between 100 nm to 1 μm are present together with numerous nearly spherical particles characterized by an average diameter of about 50 nm. Given the XRD results presented above,

the particles are, most probably, composed of amorphous Ni_xP_y phases.

Yarn treated with the electroless Ni bath were the starting point of attempts to plate Au on Kevlar fibers. This strategy was adopted because efforts to coat fibers pretreated just with the Sn^{2+}/Pd^{2+} surface activation step were unsuccessful.

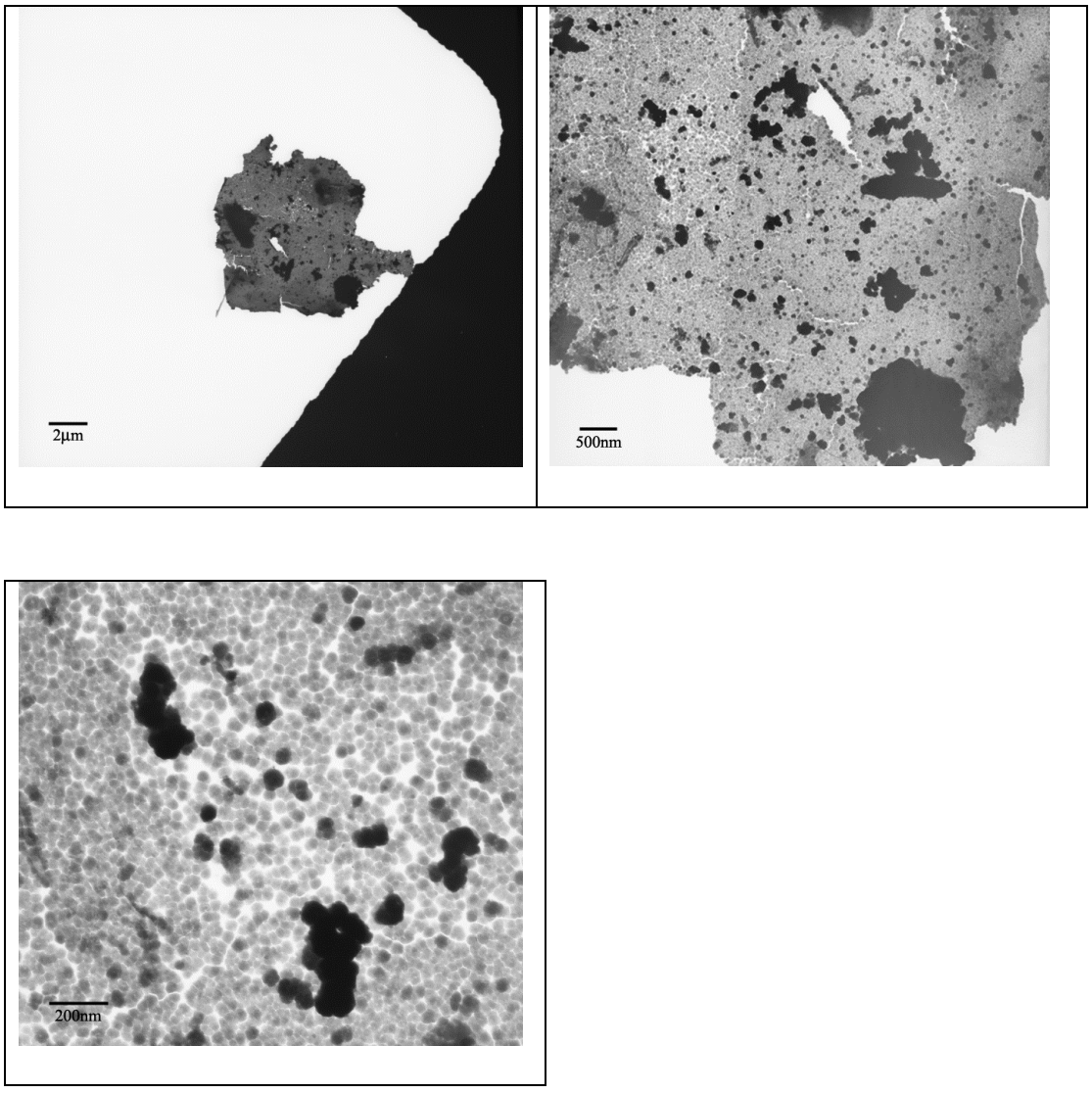

Figure 4-7. TEM images of a powder from Kevlar fibers exposed to the Ni electroless bath.

Only fibers with mass increase of at least 14% from the electroless Ni process served as suitable substrates for plating using the room-temperature Au electroless bath based on $Na_3Au(S_2O_3)_2$ and L-ascorbate ions as the reducing agents. Gold coating of PAN fibers pretreated with a similar electroless Ni process was reported to require only 3 min of immersion in the Au thiosulfate bath.[16] In contrast; Au deposition onto Kevlar fibers was not easily reproducible, requiring immersion times that varied between 5 to 30 min in order to achieve a constant golden coloration of the coatings. Reduction of the Au(I) ions by ascorbate ions on surface deposits generated by the electroless Ni bath can be represented by the reaction,

$$2Au^{+} + C_6H_7O_6^{-} \rightarrow 2Au + C_6H_5O_6^{-} + 2H^{+} \qquad (3)$$

Presented in Figure 4-8 is a SEM image obtained after sectioning fibers that were plated with the Au electroless method following the electroless Ni step. After such treatment, the fibers exhibited an average diameter of 13.5 μm, which is a substantial change as compared with the non-coated but cleaned material (diameter = 11.2 μm). As illustrated in the image sectioning of the samples induced significant damage including fracturing of segments of the coating. Separation of the metal coating from the substrate is observed in some cases, resulting in hollow metallic tubes highlighted by the circles. Analogous observations were made in an investigation that employed similar electroless plating baths to grow metal tubes using fibers as sacrificial templates.[17] The inset in Figure 4-8 displays a magnified view of the fiber highlighted by an arrow in the main image. Apart from the fiber substrate, two different layers are clearly visible; EDS measurements confirmed that Ni was present on the bottom layer whereas the top layer consisted of Au. In contrast, coatings consisting of a single layer were

obtained previously upon metallizing PAN fibers with consecutive electroless Ni and Au plating methods very similar to those employed in the present study.[16] Compared in Figure 4-9 is a diffraction pattern of clean Kevlar fibers (black line) with that of fibers exposed sequentially to Ni and Au electroless platings. Both patterns exhibit the signals at low angles corresponding to X-ray scattering from the Kevlar materials.

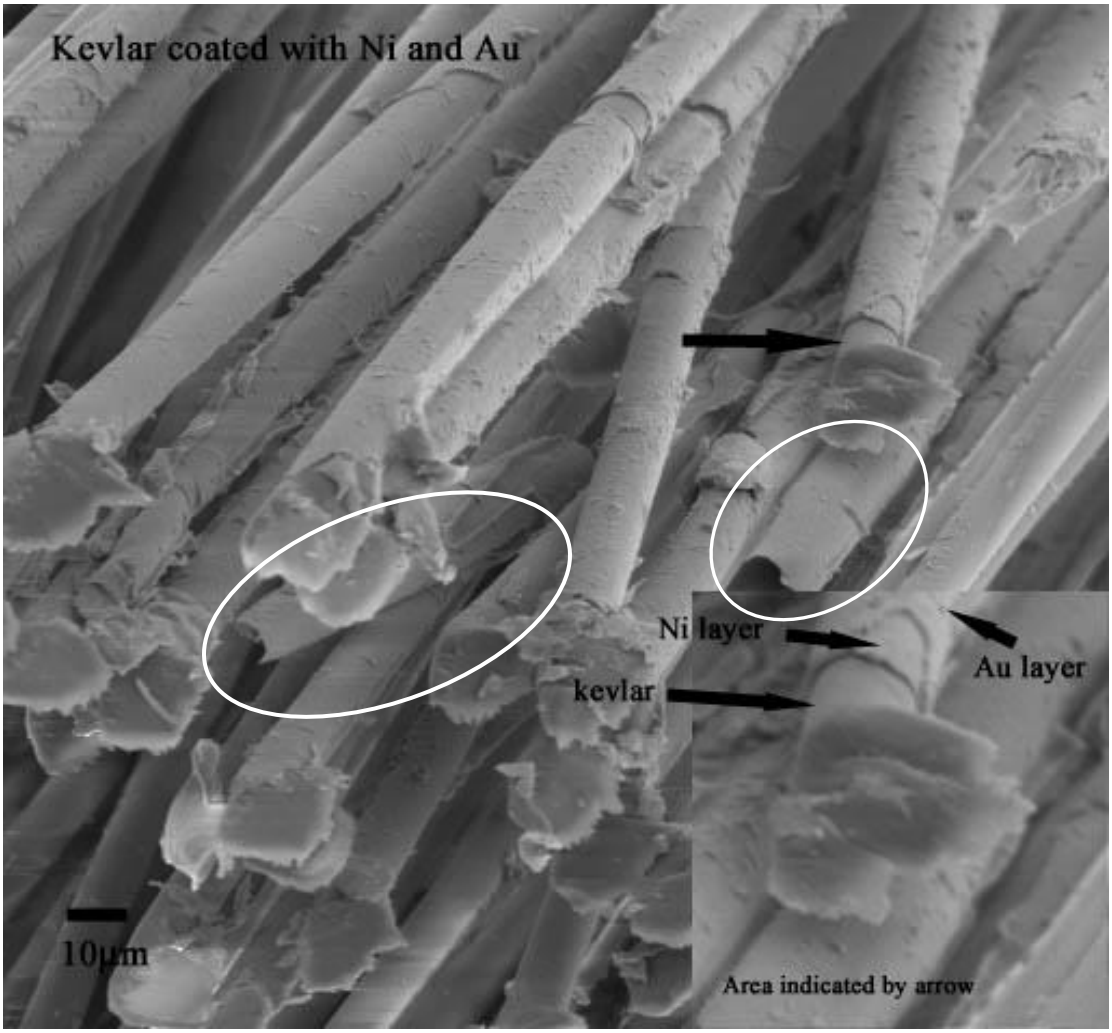

Figure 4-8. SEM image of sectioned Kevlar fibers first coated using the electroless Ni bath followed by treatment with the Au(I) thiosulfate electroless method. Inset: close-up of the area that includes the fiber tip highlighted by an arrow in the main image.

Most of the strong signals detected in the case of the coated fibers can be indexed as reflections from metallic (fcc) Au. The exception is the signal at 22.9 degrees, which is close to the diffraction from the {111} lattice plane of metallic (fcc) Ni. Although the golden color of the resulting yarn appeared fairly uniform under visual inspection, SEM examination revealed that the electroless Au plating method frequently yielded uneven coatings including fiber sections that remained uncoated. In view of these reproducibility shortcomings, the electroless Au plating method was deemed unsatisfactory and was no longer explored.

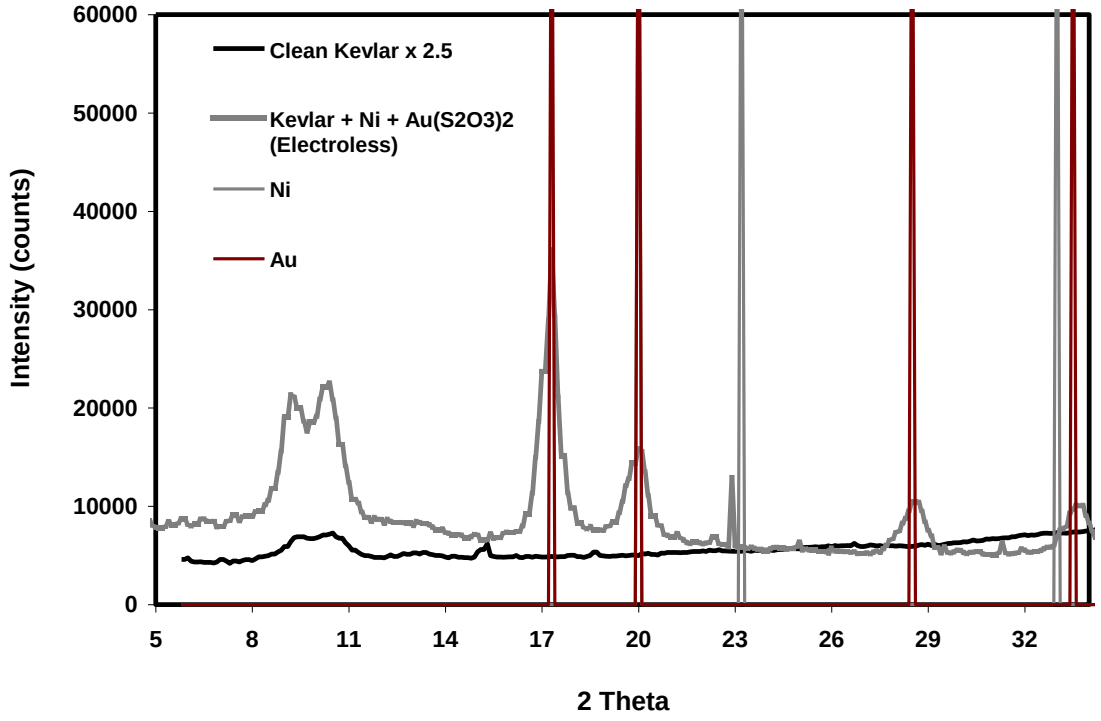

Figure 4-9. XRD patterns of Kevlar fibers (black line) and of fibers pre-coated with the electroless nickel bath (1.6 x 10^{-3} g/cm Ni), then coated with 8.1 x 10^{-3} g/cm Au via electroless deposition (grey line). Data collected using Mo K(α) radiation; vertical lines identify reference positions for the diffractions of metallic Ni (grey) and Au (red).

Electrochemical experiments were performed on Kevlar yarn plated with the Ni electroless method given that attempts to electroplate Au onto fibers treated only with the Sn^{2+}/Pd^{2+} surface activation step were unsuccessful. This result is not surprising since the very high resistivity of fibers after the Sn^{2+}/Pd^{2+} procedure made them unsuitable as electrodes. In contrast, fibers coated with a single electroless Ni deposition exhibited a typical resistivity of about 20 ohm/cm, which enabled them to serve as cathodes. Initial experiments with such fibers served to characterize the reaction parameters for Au electrodeposition with both the thiosulfate and cyanide procedures described previously. The optimum deposition parameters were identified empirically and correspond to a potential of -0.6 V vs. Ag/AgCl and a current of -2.5 mA for the $Au(S_2O_3)_2^{3-}$ system, and values of -1.09 V vs. Ag/AgCl and -2.5 mA were determined for the $Au(CN)_2^-$ system. In the NHE scale these values amount to -0.401 and -0.891 V and are lower than the standard potentials, 0.153 and -0.595 V, respectively.[19] Such potential differences probably result from the high fiber resistance together with the reactant concentrations employed in the present study that are lower than those of the standard states.

In both systems the electrochemical reduction of gold ions to gold atoms on a conductive surface acting as the cathode can be represented in a simplistic fashion by reaction 4:

$$Au^+ + e^- \rightarrow Au \qquad (4)$$

As anticipated, the net current output increased during Au coating in both systems because the deposited gold lowers the resistance of the fibrous material and facilitates further metal plating. Plating times between the range of 3-5 min produced uniform substrate coloration in the case of the thiosulfate electrochemical system. The cyanide electrodeposition method required 1 h to yield strongly adhering and dense coatings (average diameter = 12.9 μm) but the number of

fiber surface places left uncoated was markedly higher. Although both electrochemical procedures produced coatings more uniform than those resulting from the electroless Au deposition, the thiosulfate electroplating procedure was selected for further optimization since this method involved shorter reaction times and avoided handling of fairly toxic solutions.

An important property of metallized fibers is robustness of the coatings, which was probed via exposure of the coated yarn to ultrasound in H_2O. Figures 4-10 to 4-12 are a series of SEM images obtained at increasing magnifications of fibers first treated with the Ni electroless bath, followed by exposure to ultrasound and then coated with Au using the thiosulfate electrochemical procedure. Figure 4-10 shows a low magnification overview of a group of fibers containing seemingly smooth coatings. Electroplating induced a large increase in average fiber diameter to 15.9 μm as compared with that (12 μm) obtained after coating with the electroless Ni bath. An interesting observation is that Au metallization started at the yarn end connected to the external electrical circuit and propagated along the fiber axes. In contrast, Au electrodeposition on yarn not exposed to ultrasound started simultaneously on numerous places and extended via overlap of the growing coating. Tested yarns exhibited coating defects including uncoated areas and fractures that were less numerous on fibers not subjected to the ultrasound test. As shown in Figure 4-11, exposed sections of the polymer surface were frequently found, indicating that segments of the Ni electroless coating were stripped from the fibers by the ultrasound. Dislodgment of weakly adhering Ni/Ni_xP_y deposits left bare fiber surface area where electrodeposition of Au was not possible. While coating fractures were less frequent, they probably originate from to ultrasound-induced rupturing of defect regions in the Ni/Ni_xP_y coatings. Obviously, the subsequent Au electrodeposition step was unable to close

the fractures. Presented in Figure 4-12 is a close-up image centered on a fiber displaying a coating fracture and several areas were the metal deposit was missing.

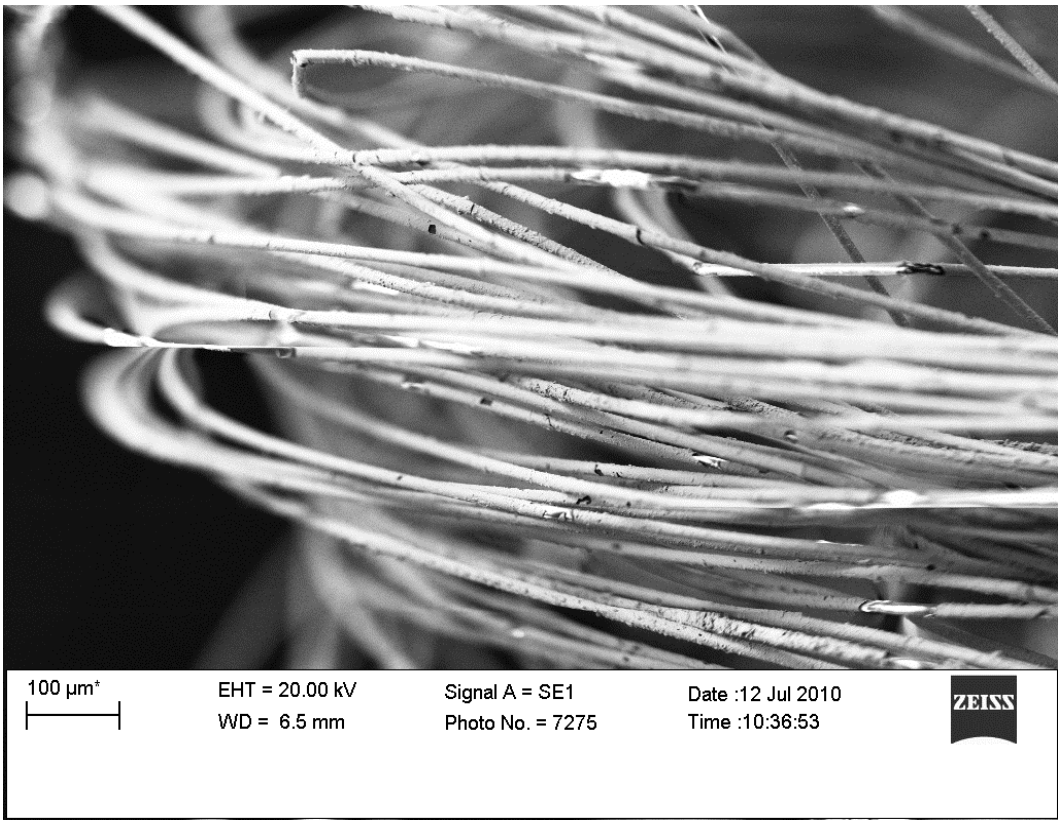

Figure 4-10. SEM image showing an overview of a group of Kevlar fibers first coated in the Ni electroless bath, then exposed to ultasound in H_2O and electroplated with Au via the thiosulfate procedure.

The surface roughness of the coating is evident at this magnification in the form of granules. Interestingly, the coating appeared as a uniform film, which contrasts with the layered structure of deposits formed when both metallization steps used electroless procedures, see Figure 4-8. As mentioned earlier, consecutive Ni and Au electroless platings on PAN fibers also yielded single-layer coatings.[16] This result was explained by assuming that deposited Au diffused to some extent into the initially plated Ni material. A similar phenomenon may have occurred

Figure 4-11. SEM image of Kevlar fibers first coated in the Ni electroless bath, then exposed to ultrasound in H_2O and electroplated with Au via the thiosulfate procedure.

during Au electrodeposition onto Kevlar fibers, where the resulting coatings were at least 10 times thicker than those plated on PAN fibers.

Presented in Figure 4-13 are TEM images of a slice microtome from fibers that were subjected to the ultrasound test. Shown on the top two images are different areas of the sample, the darker regions correspond to surface regions of the fiber that contain coating. Displayed on the bottom are high magnification images of regions highlighted by circles on the top frames. These images provide evidence that numerous small particles (highlighted by circles) exist inside the fibers. Since the particles were found within the polymer backbone only after gold was plated, an obvious interpretation is that they consist of Au. Since the presence of particles inside the fibers was observed exclusively after the ultrasound exposed the initial Ni coating, the particle formation mechanism remains unclear.

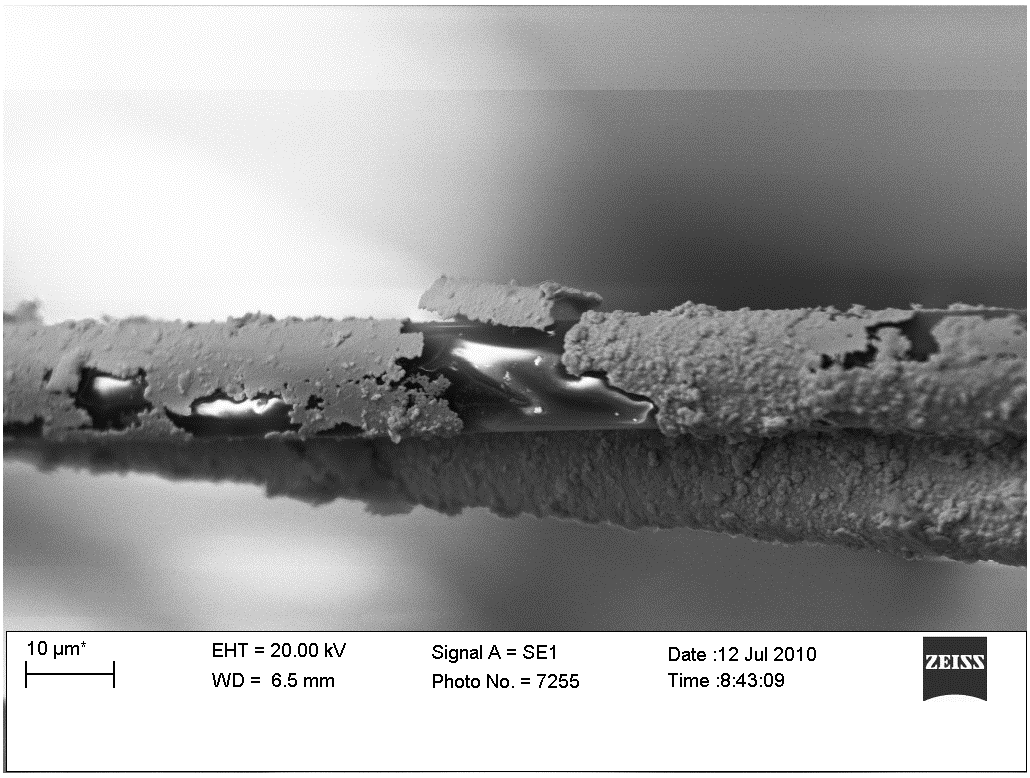

Figure 4-12. High magnification SEM image of a Kevlar fiber first coated in the Ni electroless bath, then exposed to ultrasound in H_2O and electroplated with Au via the thiosulfate procedure.

Further experiments showed that the adhesion problems could be solved through application of multiple electroless Ni plating steps, each containing a sensitization step. Adhesion of the coatings improved considerably when three consecutive electroless Ni depositions were carried out prior to three successive Au electrochemical platings (*e.g.* Ni, Ni, Ni, Au, Au, Au). Defects were rarely detected in coatings derived from this procedure, and the deposits were no longer affected by ultrasound waves or by the adhesive tape test.

Mass changes determined during Au plating varied somewhat linearly with the number of deposition steps and increases between 150-180 % were produced after three coatings. Surprisingly, treatment of the fibers with the Sn^{2+}/Pd^{2+} surface activation method between successive Au plating steps improved the efficiency of the subsequent coating step. On the

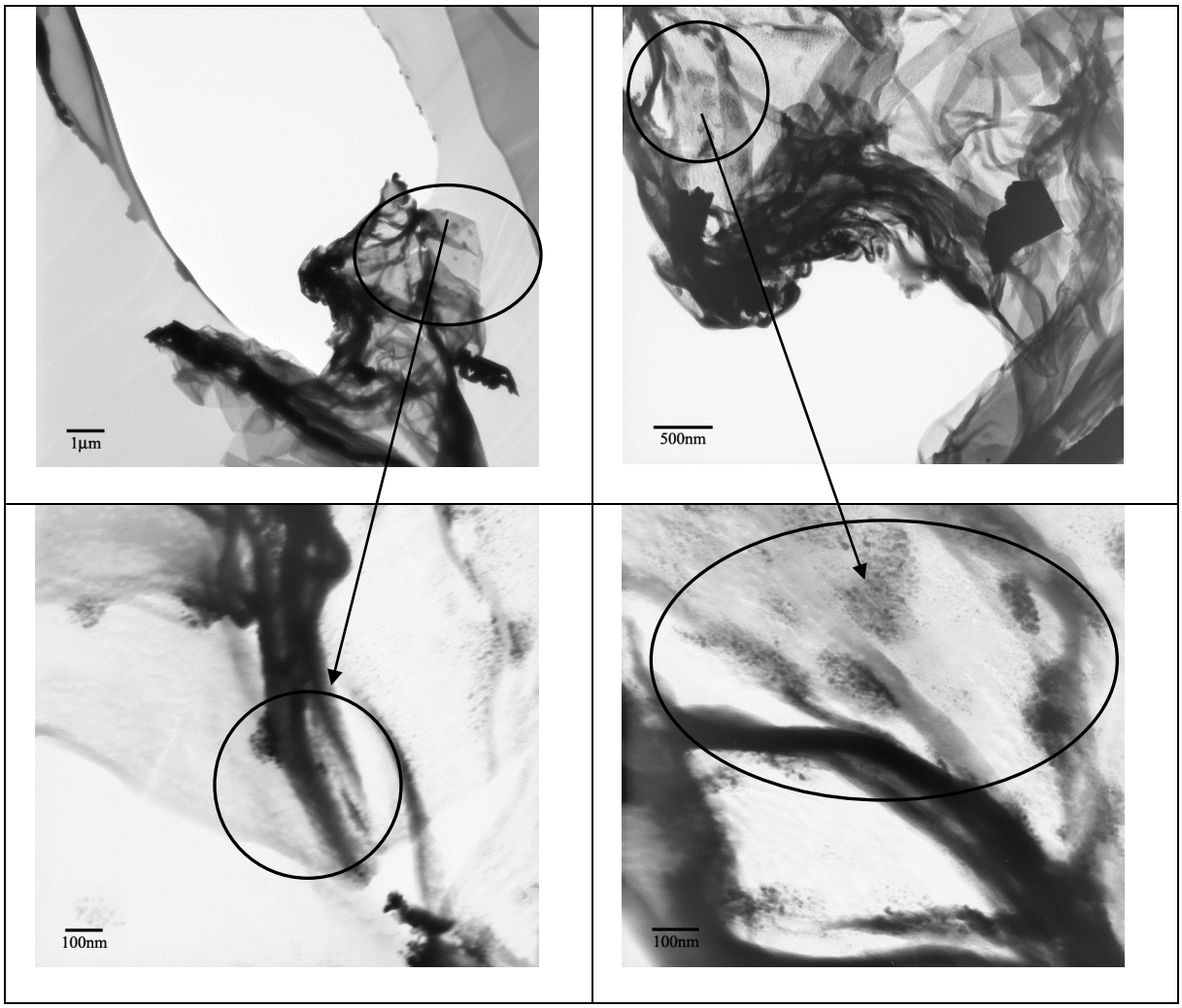

Figure 4-13. TEM images from 95 nm thick slices microtomed out of Kevlar fibers plated with the electroless Ni bath, sonicated and metallized electrochemically with Au. Each bottom picture corresponds to a magnified view of the area encircled on the corresponding top image.

other hand, nearly constant total mass increases of about 100 % resulted when surface activated Kevlar fibers were subjected to three electroless Ni coating steps, yet the contribution of each individual plating step was not equivalent. Figure 4-14 depicts a diffraction pattern obtained from fibers plated three times in the electroless Ni bath followed by three gold electrodepositions. Signals at 2θ angles of 38.3, 44.6, 64.8, 77.8, 82, 98.8, 111, 115.5 and 135.7 degrees were detected, which can be indexed as diffractions from the {111}, {200}, {220}, {311}, {222}, {400}, {331}, {420} and {422} lattice planes of metallic Au (JCPDF

card 4-0784). Despite the fact that the multistep plating method yielded large amounts of coated Ni, and that EDS measurements confirmed the presence of this element on the fiber surfaces, diffractions corresponding to metallic (fcc) nickel were not detected. These results

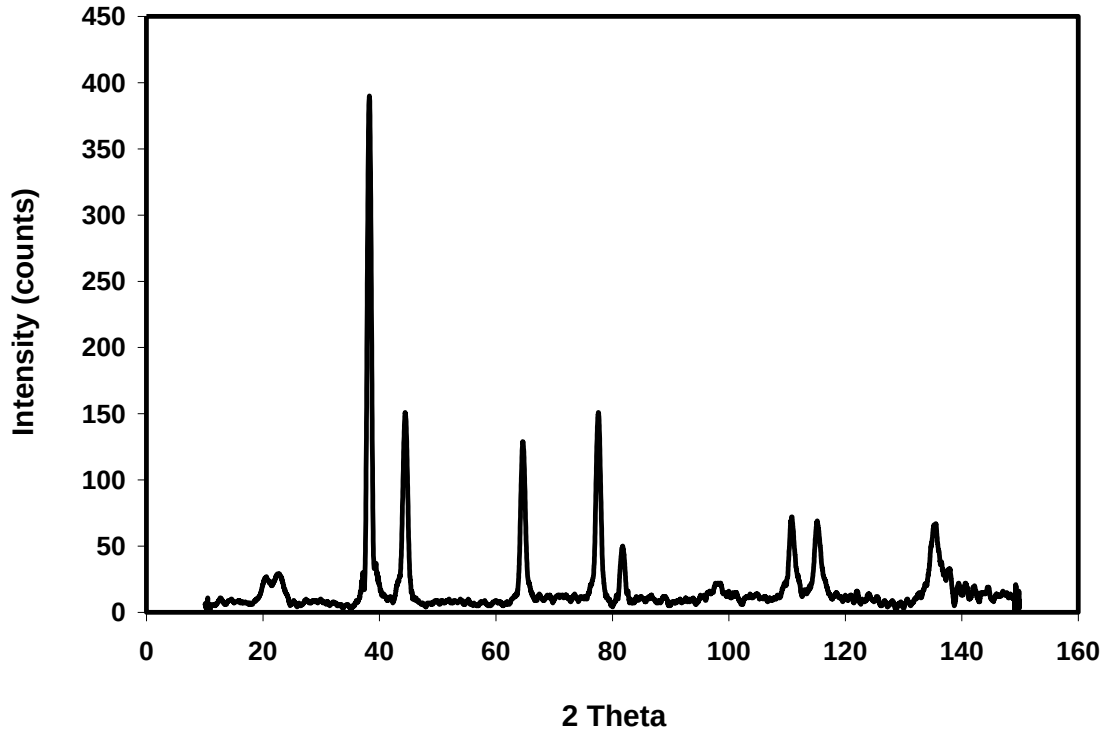

Figure 4-14. XRD pattern obtained with Cu K(α) of Kevlar fibers coated three times via electroless Ni deposition followed by three electrochemical Au platings.

are consistent with the data shown in Figure 4-5 and support the conclusion that most of the Ni deposited via the electroless process is present as amorphous Ni_xP_y phases. Given the large amounts of gold plated on the fiber surfaces via the multiple deposition method, and the small Pd concentrations present in the coatings, any XRD signals corresponding to palladium are obscured by the much more intense Au diffractions. Hence, in addition to the reflections originating from metallic Au, only the signals at low angles due to scattering of X-rays by the

fibers are observed in Figure 4-14. Figure 4-15 shows an SEM image of fibers coated by means of the multiple deposition procedure. As is evident from this Figure the coatings were, in general, uniform but exhibited numerous “grains”.

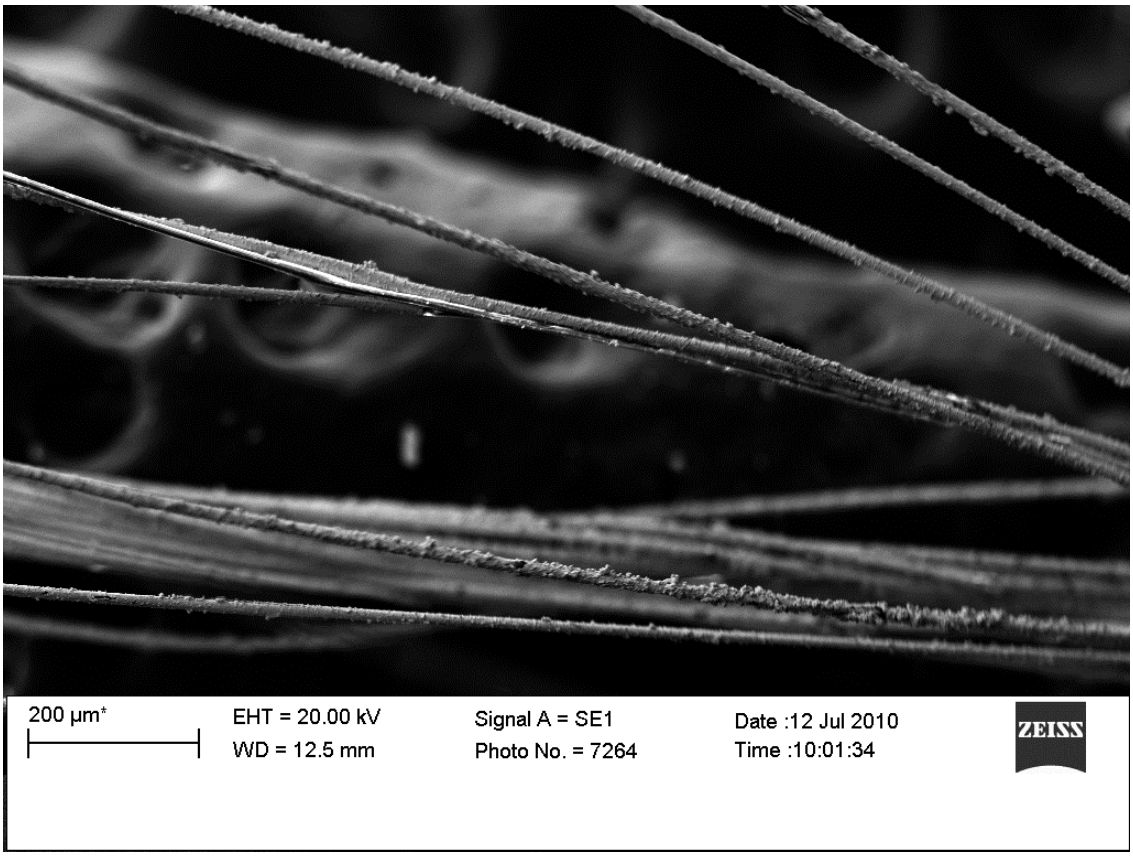

Figure 4-15. SEM image of Kevlar fibers treated three times with the electroless Ni method, then coated three times with Au via the thiosulfate electrodeposition procedure.

Presented in Figure 4-16 is an image at higher magnification of the fibers plated with the multiple deposition method. The resulting fibers exhibit an average diameter of 17.5 µm and numerous grains with sizes between 1 and 10 µm protruded from the coatings. The larger Au crystallites found in the case of the Kevlar fibers seem to be a consequence of the specific plating procedure used since multiple depositions were also employed in one of the previous

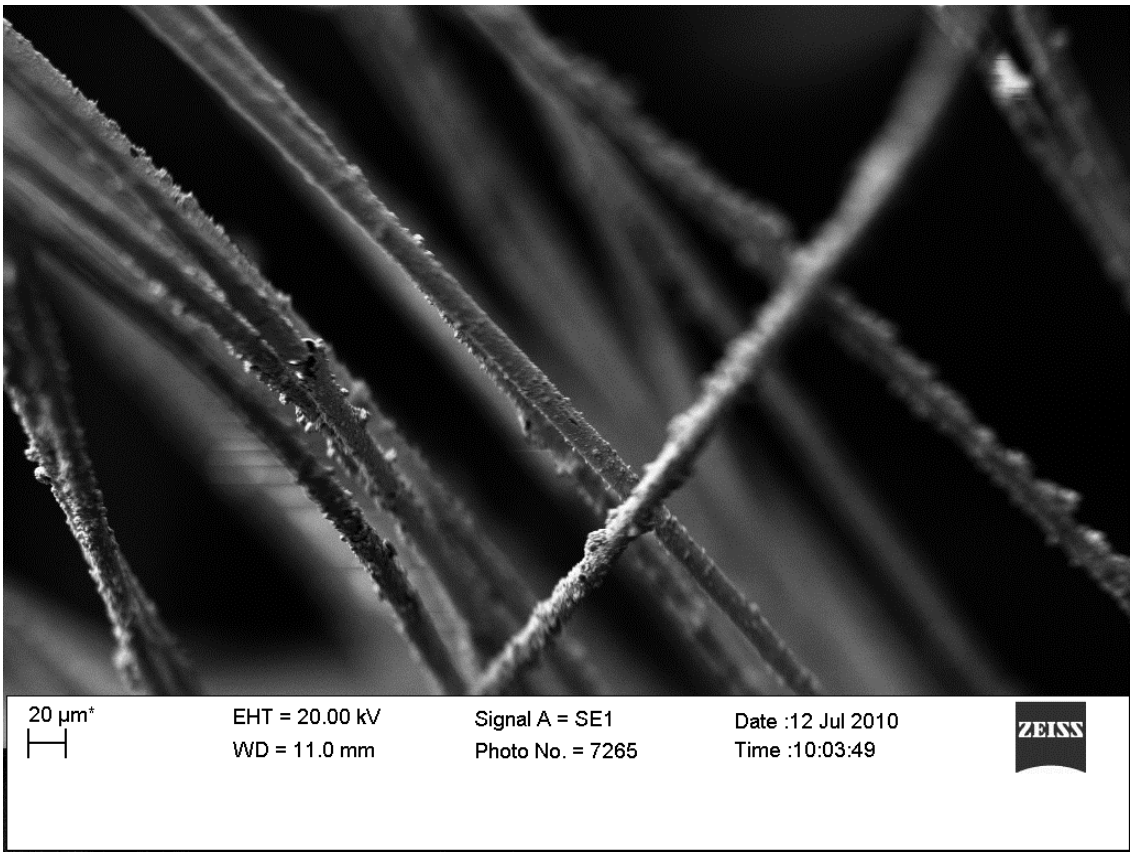

Figure 4-16. SEM image at higher magnification displaying coatings on Kevlar fibers treated three times with the electroless Ni method, then coated three times with Au via electrodeposition.

studies that generated smaller Au grains.[26] The multiple step deposition procedure employed in the present study suppressed significantly coating defects, particularly the occurrence of places on the fiber surface that remained free of coating. However, fractures in the coating were not entirely eliminated.

Compiled in Table 4-1 are results of mass increases and resulting conductivities from fibers prepared in coating experiments involving three consecutive electroless Ni platings combined with three successive electrochemical steps using the thiosulfate procedure. Included are results obtained from fibers coated via a single electrodeposition using the cyanide method. Fibers exhibiting weight increases between 60-120% after the electroless Ni

treatment exhibited resistance values (≤ 30 ohm/cm) low enough to enable Au plating with the thiosulfate electrodeposition method. An exception occurred in the case of the cyanide method, which enabled Au electrodeposition on fibers exhibiting mass increases of only 14% after the Ni electrodeposition on fibers exhibiting mass increases of only 14% after the Ni electroless treatment. The fact that the measured Au mass increases correlated with the number of electrodeposition steps suggests that depletion of $Au(S_2O_3)_2^{3-}$ ions within the bulk of the solution may play a role during plating, which is consistent with the lower mass gain detected when the yarn length doubled, compare entries 1 and 2 in Table 4-1. An interesting issue is that the increase in percent mass from the electrodeposition steps refers to the masses measured after and before Au plating. On the other hand, the mass percent increases from the electroless process resulted from the difference between plated and non-plated fibers.

Table 4-1. Conductivity and mass change for metallized fibers of a length of 9 cm.

Treatment	**Mass Change Ni**	**Mass Change Au**	**Conductivity (S cm^{-1})**
K-Ni- $Au(S_2O_3)_2^{3-}$	102.5 %	181.5 %	[a]NT: 3.07; TW: 6.02
[b]K-Ni- $Au(S_2O_3)_2^{3-}$	103 %	149 %	NT: 1.19; TW: 3.17
[c]K-Ni- $Au(S_2O_3)_2^{3-}$	110 %	49.5 %	NT: 0.75; TW: 2.4
K-Ni- $Au(CN)_2^-$	14 %	100 %	NT: 0.86; TW: 1.17

a: NT = fibers not twisted; TW = twisted fibers. b: Metallized fibers of a length of 25 cm. c: Fibers sonicated for 10 min after electroless Ni coating, then electroplated with Au.

This means that the mass increases resulting from the Au deposition process are much larger than those derived from the electroless treatment. An exception occurred for fibers subjected

to the ultrasound test, which experienced very similar increases of mass in both electroless and electrochemical platings.

Resistivity measurements were performed on twisted and non-twisted metalized yarn; as shown in Table 4-1, fiber twisting yielded a 3.6 increase in conductivity. Twisting of coated fibers is known to increase their conductivity,[14] which is rationalized on the basis that a higher number of contact points between fibers exist in twisted yarn. This leads to additional conductive pathways for electrons to migrate that are not available in non-twisted fibers. Another general correlation is that, in general, raising the mass of deposited Au increased the fiber conductivity. Comparison of entries 3 and 4 in Table 4-1 indicate that Au coating of Kevlar fibers via a cyanide bath yielded conductivity similar to that obtained by means of the thiosulfate method. Considering that the latter treatment is faster and safer, utilization of the cyanide method offers no significant advantage.

Illustrated in Figure 4-17 are results from experiments that probed the ability of metallized Kevlar fibers to sustain electrical currents utilizing freestanding, non-twisted yarn. To improve electrical contact, yarn sections were wrapped in narrow strips of Al foil and clamped to connectors linked to the potentiostat. This arrangement allowed determinations of power output at variable distances along the yarn. The data presented in Figure 4-17a demonstrates that over a yarn distance of 3.2 cm no limitation in the passage of current exists up to a power output of 9 W (the maximum value that can be determined by the potentiostat). Measurements performed over a yarn distance of 6.5 cm showed that a point failure occurred at 1.8 W. Systematic measurements showed that, on average, the Au metallized Kevlar fibers can sustain a power output of 1 W.

Compared in Table 4-2 are tensile strength results determined from individual Kevlar

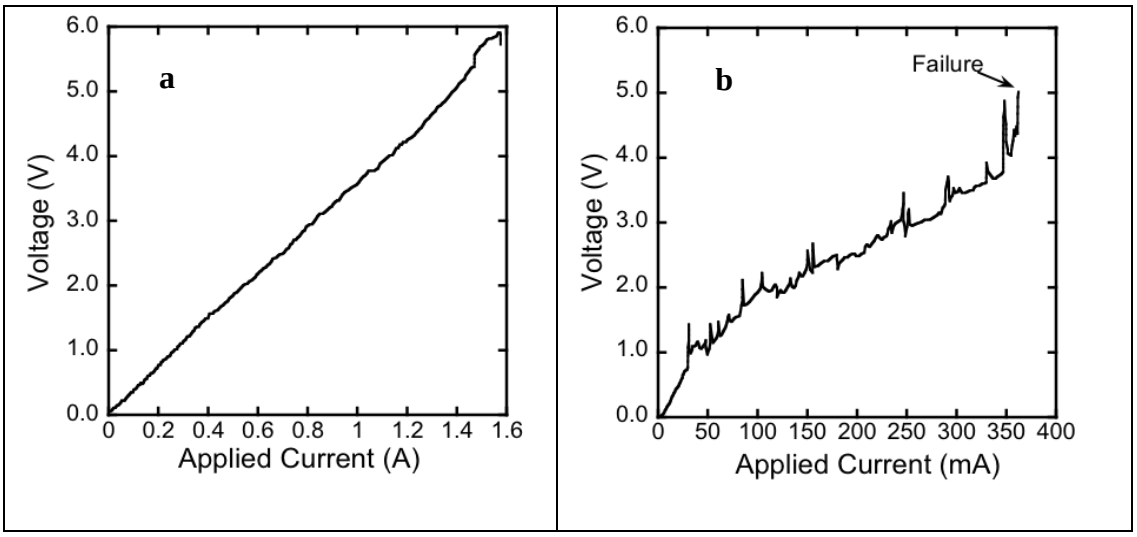

Figure 4-17. Plots of current versus voltage obtained for a 9 cm Kevlar yarn treated three times with the electroless Ni method, then coated three times with Au via electrodeposition. Panel a) displays results from measurements over a yarn distance of 3.2 cm; the data of panel b) is indicative of a point failure at 1.8 W for a distance along the yarn of 6.5 cm.

monofilaments that are the components of the metallized materials. A single electroless Ni plating step induces of modest decrease of 10% in the strength of the filaments, but an additional electrochemical Au plating step with the cyanide method induces a larger decrease of about 28 %. Metallization of the yarn with three consecutive electroless Ni platings and three successive Au electrochemical depositions resulted in practically the same (27 %) decrease in the strength of the monofilaments. Obviously, Au coatings affect the fiber strength in a fashion more pronounced than Ni and also influence negatively the reproducibility of the experiments.

Metallization of Kevlar fibers involving surface activation initiated by strong bases in dimethy sulfoxide has been reported to yield coatings that have no negative effect on the fiber tensile strength.[18] Furthermore, the resulting coated materials were claimed to exhibit the same conductivities as those of the pure metals employed in the coatings.

Table 4-2. Tensile Strength Measurements for Metallized Fibers

Sample type	**Average maximum load (cN)**	**C. V. % (average maximum load)[a]**	**% change in fiber strength**
Clean Kevlar	31.5	5.2	0.0
K - Ni	28.5	23.3	10.6
K-Ni- $Au(S_2O_3)_2^{3-}$	23.0	33.9	26.9
K-Ni- $Au(CN)_2^-$	22.7	14.4	27.8

a: C. V. = coefficient of variance measures the deviation in the measured maximum load.

Although the coatings derived from the present study affected the strength of the fiber and exhibited lower conductivities, their preparation was free of the reproducibility issues that seem to plague methods involving surface activation with bases. The conductivity values reported here for Au electrodeposited Kevlar fibers (NT =1.02 S/cm, TW = 3.65 S/cm) are as good or better than those of Cu coated cotton fibers (~1 S/cm) obtained using electroless plating techniques.[14] As anticipated, no changes in the properties of Au plated Kevlar fibers were detected after storing them under air for two years, which contrasts with the conductivity decreases experienced by the Cu coatings due to their reactivity toward O_2. Also, the Au coatings seem to exert no significant deterioration of the fiber flexibility but data from specific tests are needed to quantify this observation. The decrease in tensile strength of the resulting Kevlar materials will not hinder possible practical uses of the metalized fibers in areas such as textiles. However, utilization of the metallized fibers as materials for space tethers seems questionable given their limited conductivity together with the presence of defects in the coatings.

The tested electroless Ni and Au deposition methods suffered from a lack of reproducibility in terms of achieving uniform metallization. Part of this problem is related to the reduced

(laboratory) scale of the experiments since the reactions were carried out in relatively small containers with respect to the length of the fibers to be coated. Sporadic contacts between the fiber surfaces are unavoidable under such conditions, and are the most probably origin for the reproducibility problems, which has been reported before.[16] Despite the fact that the electroless Ni deposition failed to produce metallic nickel on the fiber surfaces, the resulting coatings (probably amorphous Ni_xP_y) aided the subsequent electrochemical Au deposition. However, plating of such Ni compounds on the fiber surfaces may inherently yield non-uniform coatings, negatively affecting the uniformity of the subsequent Au deposition. Another concern related to the electroless Ni-phosphite baths is the evolution of H_2 gas as a byproduct of the deposition process. Since H_2 is believed to form within the coatings as well, evolution of this gas inevitably leaves behind voids in the plated material and also between substrate and coated layer.[25] Further efforts should be devoted to achieving uniform metallic Ni coatings by means of deposition processes that are free of these problems.

Conclusions

Gold electrodeposition procedures were superior as compared to electroless methods in terms of reproducibility, and yielded higher mass gains, better adhesion and lower resistance. Inconsistencies encountered during Au deposition onto the surface of Kevlar fibers are likely results of problems associated with the initial Ni coating treatment and not with the electrodeposition method. Utilization of alternative electroless Ni deposition methods that produce coatings of metallic Ni is expected to yield substantial improvements in the metallization procedure. Although the metallization procedure presented here is somewhat laborious, the coated Kevlar fibers seem capable of sustaining power outputs of about 1 W and

may be useful in applications involving “smart” textiles.

References

(1) Mittal, K. L., Ed.; *Metallized Plastics 7*; V.S.P. Intl. Sci.: AH Zeist, 2001, and earlier volumes.

(2) (a) Grossman, E.; Gouzman, I. *Nucl. Instr. Meth. Phys. Res. B* **2003**, *208*, 48-57. (b) Packirisamy, S.; Schwam, S.; Litt, M. L. *J. Mater. Sci.* **1995**, *30*, 308-320.

(3) Lorenzini, E.; Sanmartín, J. *Sci. Am.* **2004**, *291*, 50-57.

(4) Frisbee, R. H. J. *Propulsion Power* **2003**, *19*, 1129-1154.

(5) Orban, R. *J. Coated Fabrics* **1989**, *18*, 246-254.

(6) Grace, M.; Chand, N.; Bajpai, S. K. *J. Engineered Fibers Fabrics* **2009**, *4*, 24-35.

(7) Park, S.; Jayaraman, S. *MRS Bull.* **2003**, *28*, 585-591.

(8) Kim, Y. K.; Lewis, A. F. *MRS Bull.* **2003**, *28*, 592-596.

(9) *Intelligent Textiles for Personal Protection and Safety*; Jayaraman, S.; Kiekens, P.; Grancaric, A. M., Eds.; IOS Press: Amsterdam, Netherlands, 2005.

(10) *Wearable Electronics and Photonics*; Tao, X., ed.; Woodhead Publishing: Cambridge, U.K., 2005.

(11) Bigg, D. M. *Short Fibre-Polym. Compos.* **1996**, 144-167.

(12) McNaughton, T. G.; Horch, K. W. *J. Neurosci. Methods* **1996**, *70*, 103-110.

(13) *Electroless Plating*; Mallory, G. O.; Hajdu, J. B., Eds.; AESF: Orlando, 1990, Chapters 1 and 14.

(14) Liu, X.: Chang, H.; Huck, W.; Zheng, Z. *ACS Appl. Mater. Interfaces* **2010**, *2*, 529-535.

(15) (a) Vaia, R. A., Lee, J.-W.; Click, W.; Price, G.; Wang, C.-S. *Mat. Res. Soc. Symp. Proc.* 1998, 519(Organic/Inorganic Hybrid Materials), 201-209. (b) Vaia, R. A., Lee, J.-W., Wang, C.-S., Click, W., Price, G. *Chem. Mater.* **1998**, *10*, 2030-2032.

(16) Pinto, N. J.; da Silva, A. N. R.; Fachini, E.; Carrion, P.; Furlan, R.; Ramos, I. *Polym. Preprints* **2003**, *44*, 138-139.

(17) Ochanda, F.; Jones, Jr., W. E. *Langmuir* **2005**, *21*, 10791-10796.

(18) Burch, R. R. In *Metallized Plastics 3*; Mittal, K. L. Ed.; Marcel Dekker: New York, 1998; pp. 45-54.

(19) Green, T. *Gold Bull.* **2007**, *40*, 105-114.

(20) Chong, E. K.; Stevens, M. G. In *Metallized Plastics 5 & 6*; Mittal, K. L. Ed.; V.S.P. Intl. Sci.: Utrecht, 1998; pp. 409-422.

(21) Zavadskii, A. E.; Zakharova, I. M.; Zhukova, Z. N. *Fibre Chem.* **1998**, *30*, 6-10.

(22) Goldenstein, A. W.; Rostoker, W.; Schossberger, F. *J. Electrochem. Soc.* **1957**, *104*, 104-110.

(23) Abrantes, L. M.; Fundo, A.; Jin, G. *J. Mater. Chem.* **2001**, *11*, 200-203.

(24) Kim, D.; Kim, J.; Yoon, J.; Lee, W.; Jung, S. *Surf. Interface Anal.* **2006**, *38*, 440-443.

(25) Chen, C.; Chen, B.; Hong, L. *Chem. Mater.* **2006**, *18*, 2959-2968.

(26) Winters, E. D.; Coronati, J. M.; Braski, D. M.; Watkins, D. R. *Plating Surface Finishing* **2000**, *87*, 68-75.

(27) San March, C.; Moody, N. R.; Cordill, M. J.; Lucadamo, G.; Kelly, J. J.; Headley, D.; Yang, N. *Mat Res. Soc. Symp. Proc.* **2004**, *821*, 281-286.

V. CONCLUSIONS

The results gathered in the present investigation demonstrate that H_2O_2 is generated in solutions of SPEEK/PVA that contained air. Formation of the peroxide occurs in a synchronous fashion with the consumption of oxygen. The kinetic data is consistent with a mechanism in which the rate-determining step is the photochemical process that generates the polymeric SPEEK radicals. Maximum rates of peroxide formation are obtained in neutral solutions, which suggest that efficient formation of H_2O_2 on the surface of SPEEK/PVA fibers is feasible. The decay of H_2O_2 that takes place at low oxygen concentrations in solution is not expected to occur in the case of the fibers due to the high and constant [O_2] that prevail on the surface of these polymeric materials.

Results demonstrate a "lock and key" mechanism for loading CH_3NO_2 into the pore cavities via illumination with 350 nm photons for spin coated films on a mica substrate. In addition, loading of CH_3NO_2 can be performed in two ways: 1) photolysis of PN films immersed in CH_3NO_2; and 2) photolysis of PN films in air, followed by immersion in CH_3NO_2 for slower loading rates. However, illuminated films in the presence of CH_3NO_2 with 350 nm or 420 nm photons show reverse effects on the isomerization pathway which could present problems for control and/or selectivity of the ligand within the PN material for specific applications. Further investigations into this research should examine azobenzene derivatives that are less sensitive to polar solvents to gain greater control on the isomerization of the ligands in the presence of highly polar liquids. In addition, efforts to make free standing films (detached from the mica substrate) should be pursued to verify mass transport results obtained in this study, which might be affected to some degree by the mica substrate.

At present, Sol1-3 powder seems reasonable for sensitization testing for the coalescence model. On the other hand, utilization of this material as an "on/off" safety switch will require a greater understanding of the solvent effects induced on the ligand in the presence of CH_3NO_2. Future efforts should be directed towards synthesizing smaller PN particles of uniform size with pore structure (bcc) similar to the one of spin coated films in efforts to correlate mass transport results for the inclusion of CH_3NO_2.

Gold electrodeposition procedures were superior as compared to electroless methods in terms of reproducibility, and yielded higher mass gains, better adhesion and lower resistance. Inconsistencies encountered during Au deposition onto the surface of Kevlar fibers are likely results of problems associated with the initial Ni coating treatment and not with the electrodeposition method. Utilization of alternative electroless Ni deposition methods that produce coatings of metallic Ni is expected to yield substantial improvements in the metallization procedure. Although the metallization procedure presented here is somewhat laborious, the coated Kevlar fibers seem capable of sustaining power outputs of about 1 W and may be useful in applications involving "smart" textiles.

References

(1) Gandhi, M. V.; Thompson, B. S. *Smart Materials and Structures;* Chapman and Hall: London, 1992.

(2) Schwartz, M. *Encyclopedia of Smart Materials;* John Wiley and Sons: New York, NY, 2002. Vol. 1.

(3) Shakeri, C.; Noori, M. N.; Hou, Z. *Smart Materials and Structures a Review.* Materials for the New Millennium, Proceedings of the Material Engineering Conference, 4th, Washington D. C., Nov. 10-14, 1996, 2, 863.

(4) Yoshida, M.; Lahann, J. ACS Nano **2008**, 2, 1101-1107.

(5) Shahinpoor, M.; Schneider, H. *Intelligent Materials;* Royal Society of Chemistry: Cambridge, 2008.

(6) Kornbluh, R. *et al. Electroactive polymer (EAP) Actuators as Artificial Muscles: Reality, Potential and Challenges;* SPIE Press: Bellingham, 2004.

(7) Kumar, A.; Srivastava, A.; Galaev, T.; Mattiasson, B. *Prog. Polym. Sci.* **2007**, 32, 1205-1237.

(8) Zhang, H.; Han, J.; Yang, B. *Adv. Funct. Mater.* **2010**, 20, 1533-1550.

(9) Corriu, R.; Mehdi, A.; Reyé, C. *J. Organomet. Chem.* **2004**, 689, 4437-4450.

(10) Varadan, V. K. *Proc. SPIE* **2001**, 4591, 28-38.

(11) Garg, D.; Zikry, M.; Anderson, G.; *Smart Mater. Struct.* **2001**, 10, 610-623.

(12) Zielecka, M.; Bujnowska, E. *Prog. Org. Coat.* **2006**, 55, 160-167.

(13) Saito, H.; Takai, K.; Takazawa, H.; Yamauchi, G. *Mater. Sci. Res. Int.* **1997**, 3, 216-219.

(14) Lazar, M. A.; Tadvani, J. K.; Tung, W. S.; Lopez, L.; Daoud, N. A. *Innovations in thin Film Processing and Characterization* (ITFPC 2009). IOP Conference Series: Materials Science and Engineering 2010, 12, 1.

(15) Wong, C. P.; Xu, J.; Zhu, L.; Li, Y.; Sun, Y.; Lu, J. ; Dong, H. Proceedings of the IEEE CPMT Conference on High Density Microsystem Design, Packaging, and Failure Analysis, 7th, Shanghai, China, June 27 – 30, 2005, 149.

(16) Barthlott, W.; Ehler, N.; Raster- Eletronenmikroskopie der Epidermis- Oberflachen von Spermatophyten. Tropische und Subtropishe pflanzenwelt **1977**, 19, 1-110.

(17) Crick, R. C.; Parkin, I. P. *Chem. Eur. J.* **2010**, 16, 3568-3588.

(18) Xia, F.; Jiang, L. *Adv. Mater.* **2008**, 20, 2842-2858.

(19) Lim, H. S.; Kwak, D.; Lee, D. Y.; Lee, S. G.; Choi, K. *J. Am. Chem. Soc.* **2007**, 129, 4128-4129.

(20) Parkin, I. P.; Palgrave, R. G. *J. Mater. Chem.* **2005**, 15, 1689-1695.

(21) Linsebigler, A. L.; Lu, G.; Yates, J. T. *Chem. Rev.* **1995**, 95, 735-758.

(22) Mills, A.; Crow, M. *J. Phys. Chem. C* **2007**, 111, 6009-6016.

(23) Kang, H.; Liu, H.; Phillips, J. A.; Cao, Z.; Kim, Y.; Chen, Y.; Yang, Z.; Li, J.; Tan, W. *Nano Lett.* **2009**, 9, 2690-2696.

(24) Amabilino, D. B. *Chirality at the Nanoscale: Nanoparticles, Surfaces, Materials and more;* Wiley-VCH: Weinheim, 2009.

(25) Nagamani, S. A.; Nirikane, Y.; Tamaoki, N. *J. Org. Chem.* **2005**, 70, 9304-9313.

(26) Liu, N. ; Chen, Z. ; Dunphy, D. ; Jiang, Y. ; Assink, R.; Brinker, C. *Angew. Chem., Int. Ed.* **2003**, 42, 1731-1734.

(27) Liu, N.; Dunphy, D. R.; Atanassov, P.; Bunge, S. D.; Chen, Z.; Lopez, G. P.; Boyle, T. J.; Brinker, C. J. *Nano Lett.* **2004**, 4, 551-554.

(28) Tao, X. *Wearable Electronics and Photonics;* Woodhead publishing Limited: Cambridge, U. K., 2005.

(29) Westbrook, P.; Priniotakis, G. *Intelligent/smart materials and textiles: an overview;* Woodhead publishing Limited: Cambridge, U. K., 2005.

(30) Lorenzini, E.; Sanmartin, J. Electrodynamic Tethers in Space; *Scientific American* August **2004**, 50-57.

(31) Coyle, S.; Wu, Y.; Lau, K.; Rossi, D. D. ; Wallace, G. ; Diamond, D. D. *Smart Nanotextiles : A Review of Materials and Applications ;* MRS Bulletin, 2007, 32, 434.

(32) Mallory, G. O.; Hajdu, J. B., Eds.; *Electroless Plating*; AESF: Orlando, 1990.

(33) Vaia, R. A.; lee, J. W.; Wang, C.S.; Click, B.; Price, G. *Chem. Mater.* **1998**, 10, 2030-2032.

(34) Dong, H.; Fey, E.; Gandelman, A.; Jones, W. E. *Chem. Mater.* **2006**, 18, 2008-2011.

(35) Little, B.; Li, Y.; Cammarata, G.; Mills, G. *ACS Appl. Mater. Interfaces*, preparing for submission.

(36) Liu, X.: Chang, H.; Huck, W.; Zheng, Z. *ACS Appl. Mater. Interfaces* **2010**, 2, 529-535.

(37) Carlini, C.; Angiolini, L.; Caretti, D.; Corelli, E. *Polym. Advanced Technol.* **1996**, *7*, 379-384.

(38) Gu, C.; Xu, Y.; Liu, Y.; Pan, J. J.; Zhou, F.; He, H. *Optical Mater.* **2003**, *23*, 219-227.

(39) Tian, H.; Yang, S. *Chem. Soc. Rev.* **2004**, *33*, 85-97.

(40) Ercole, F.; Davies, T. P.; Evans, R. A. *Polym. Chem.* **2010**, *37*, 37-54.

(41) Irie, M.: Ikeda, T. *In Functional Monomers and Polymers*; Takemoto, K.; Ottenbrite, R. M.; Kamachi, M. Eds.; Marcel Dekker: New York, 1997; p. 65-116.

(42) (a) Malone, K.; Weaver, S.; Taylor, D.; Cheng, H.; Sarathy, K. P.; Mills, G. *J. Phys. Chem. B* **2002**, *106*, 7422-7431. (b) Weaver, S.; Taylor, D.; Gale, W.; Mills, G. *Langmuir* **1996**, *12*, 4618-4620.

(43) *Organic Photochromic and Thermochromic Compounds*; Crano, J; R. Guglielmetti, R., Eds.; Kluwer Academic/Plenum Publishers: New York, 1999; Vol. 2.

(44) (a) Korchev, A. S. ; Konovalova, T.; Cammarata, V.; Kispert, L.; Slaten, B. L.; Mills, G. *Langmuir* **2006**, *22*, 375-384. (b) Korchev, A. S.; Shulyak, T. S.; Slaten, B. L.; Gale, W. F.; Mills, G. *J. Phys. Chem. B* **2005**, *109*, 7733-7745. (c) Korchev, A. S.; Sartin, M.; Mills, G.; B. L. Slaten, B. L.; Gale, W. F. In *Clusters and Nano-Assemblies: Physical and Biological Systems*; Jena, P.; Khanna, S. N.; Rao, B. K.; Eds, World Scientific Publishing Co.: Singapore, 2005; 371-377. (d) Korchev, A. S.; Bozak, M. J.; Slaten, B. L.; Mills, G. *J. Am. Chem. Soc.* **2004**, *126*, 10-11.

(45) Gilbert, A.; Baggott, J. *Essentials of Molecular Photochemistry*; CRC Press: Boca Raton, 1991; Chapter 7.

(46) Ulanski, P.; Bothe, K.; Rosiak, J. M.; von Sonntag, C. *Macromol. Chem. Phys.* **1994**, *195*, 1443-1461.

(47) Neta, P.; Grodkowski, J.; Ross, A. B. *J. Phys. Chem. Ref. Data* **1996**, *25*, 709-1050.

(48) Lien, L.; Fellows, C. M.; Copeland, L.; Hawkett, B. S.; Gilbert, R, G. *Aust. J. Chem.* **2002**, *55*, 507.

(49) von Sonntag, C.; Bothe, E.; Ulanski, P.; Adhikary, A. *Radiat. Phys. Chem.* **1999**, *55*, 599-603.

(50) Bielski, B. H.; Cabelli, D. E.; Arudi, R. L.; Ross, A. B. *J. Phys. Chem. Ref. Data* **1985**, *14*, 1041-1100.

(51) Görner, H. *Photochem. Photobiol.* **2006**, *82*, 801-808.

(52) Radschuwelt, A.; Rüttinger, H.-H.; Nuhn, P.; Wohlrab, W.; Huschka, C. . *Photochem. Photobiol.* **2001**, *73*, 119-127.

(53) Pitts, Jr., J. N.; Letsinger, R. L.; Taylor, R. P.; Patterson, J. M.; Recktenwald, G.; Martin, R. B. *J. Am. Chem. Soc.* **1959**, *81*, 1068-1077.

(54) (a) Winkelmann, K.; Calhoun, R. L.; Mills, G. *J. Phys. Chem. A* **2006**, *110*, 13827-13835. (b) Calhoun, R. L.; Winkelmann, K.; Mills, G. *J. Phys. Chem. B* **2001**, *105*, 9739-9746. (c) Weaver, S.; Mills, G. *J. Phys. Chem.* **1997**, *101*, 3769-3775.

(55) Gonzalez, M. C.; Le Roux, G. C.; Rosso, J. A.; Braun, A. M. *Chemosphere* **2007**, *69*, 1238-1244.

(56) Schreuder-Gibson, H.; Truong, Q.; Walker, J. E.; Owens, J. R.; Wander, J. D.; Jones, Jr., W. E. MRS Bulletin 2003, 574-578.

(57) Singh, A.; Lee, Y.; Dressick, W. J. *Adv. Mater.* **2004**, *16*, 212-215.

(58) (a) Wagner, G. W.; Sorrick, D. C.; Procell, L. R.; Brickhouse, M. D.; Mcvey, I. F.; Schwartz, L. I. *Langmuir* **2007**, *23*, 1178-1186. (b) Wagner, G. W.; Yang, Y.-C. *Ind. Eng. Chem. Res.* **2002**, *41*, 1925-1928.

(59) (a) Hong, K. H.; Sun, G. *J. Appl. Polym. Sci.* **2009**, *112*, 2019-2026. (b) Hong, K. H.; Sun, G. *J. Appl. Polym. Sci.* **2008**, *109*, 3173-3179. (c) Hong, K. H.; Sun, G. *Polym. Eng. Sci.* **2007**, *47*, 1750-1755.

(60) Heller, H. G.; Langan, J. R. *J. Chem. Soc., Perkin Trans. 2* **1981**, 341-343.

(61) Kormann, C.; Bahnemann, D. W.; Hoffmann, M. R. *Environ. Sci. Technol.* **1988**, *22*, 798-806.

(62) Stefanic, I.; Asmus, K.-D.; Bonifacic, M. *Phys. Chem. Chem. Phys.* **2003**, *5*, 2783-2789.

(63) Wilkinson, F.; Brummer, J. G. *J. Phys. Chem. Ref. Data* **1981**, *10*, 809-999.

(64) Mosinger, J.; Mosinger, B. *Experientia* **1995**, *51*, 106-109.

(65) Ramseier, M.; Senn, P.; Wirz, J. *J. Phys. Chem. A* **2003**, *107*, 3305-3315.

(66) Beckett, A.; Porter, G. *Trans. Faraday Soc.* **1963**, *59*, 2038-2050.

(67) Fickett, W. *Am. J. Phys.* **1979**, 47, 1050-1059.

(68) Tarver, C. M. *Shock Compression of Solids VI*; Springer-Verlag; New York City, NY: 2003, Chapter 10.

(69) Milne, A. M.; Bourne, N. K. *AIP Conference Proceedings* 2001, 620 (*Shock Compression of Condensed Matter*, Part 2) pp. 914-917.

(70) Engelke, R. *Phys. Fluids* **1983**, 26, 2420-2424.

(71) Cartwright, M.; Lloyd-Roach, D.; Simpson, P. J. *J. Energy. Mat.* **2007**, 25, 111-127.

(72) Zeman, S. *Struct. Bond* **2007**, 125, 195-271.

(73) Field, J. E. *Acc. Chem. Res.* **1992**, 25, 489-496.

(74) Borisenok, V. A.; Bel'skii, V. M. *Russ. J. Phys. Chem. B* **2008**, 2, 187-193.

(75) Ramaswamy, A. L. *J. Energ. Mat.* **2006**, 24, 35-65.

(76) a) Liu, N. G.; Dunphy, D. R.; Atanassov, P.; Bunge, S. D.; Chen, Z.; Lopez, G. P,; Boyle, T. J.; Brinker, C. J. *Nano Lett*. **2004**, *4*, 551-554. b) Liu, N. G.; Chen, Z.; Dunphy, D. R.; Jiang, B.; Assink, R. A.; Brinker, C. J. *Angew. Chem. Int. Ed.* **2003**, *42*, 1731-1734.

(77) Reduner, E. *Nanoscopic Materials: Size-dependent Phenomena*; RSC Publishing, Cambridge, UK: 2006, chapters 6 and 7.

(78) Spizer, D; Comet, M.; Baras, C.; Pichot, V. J. Phys. & Chem. of Solids **2010**, 71, 100-108.

(79) Dattlebaum, D.; Sheffield, S.; Stahl, D.; Dattlebaum, A.; Trott, W.; Engelke, R. *Influence of Hot Spot Features on the Initiation Characteristics of Heterogeneous Nitromethane* (in press)

(80) Sanchez, C.; Boissière, C.; Grosso, D.; Laberty, C. ; Nicole, L. *Chem. Mater.* **2008**, 20, 682-737.

(81) Hoffmann, F.; Cornelius, M.; Morell, J.; Fröba, M. *Angew. Chem. Int. Ed.* **2006**, 45, 3216-3251.

(82) Grosso, D. et al. *Adv. Funct. Mater.* **2004**, 14, 309-322.

(83) Liu, N.; Dunphy, D. R.; Rodriguez, M. A.; Singer, S. Brinker, *J. Chem. Commun.* **2003**, 1144-1145.

(84) Kruk, M.; Jaroniec, M. Chem. Mater. **2001**, 13, 3169-3183.

(85) Jaroniec, M.; Solovyov, L. Langmuir **2006**, 22, 6757-6760.

(86) Lin-Vien, D *et al. The handbook of Infrared and Raman Characteristic Frequencies of Organic Molecules*; Academic Press Inc, San Diego, CA: 1991, chapters 9 and 10.

(87) Brinker, C. J. and Scherer, G. W. *Sol-Gel Science: The Physics and Chemistry of Sol-Gel Processing*; Academic Press, Inc., San Diego, CA: 1990, chapter 3.

(88) Reichardt, C. *Solvent and Solvent Effects in Organic Chemistry*; VCH Publishers, New York, NY: 1988, chapter 5.

(89) Wildes, P. D.; Pacifici, J. G.; Irick, G. I.: Whitten, D. G. J. Amer. Chem. Soc. **1971**, 2004-2008.

(90) Schanze, K. S.; Mattox, T. F.; Whitten, D. G. *J. Org. Chem.* **1983**, 2808-2813.

(91) Mittal, K. L., Ed.; *Metallized Plastics 7*; V.S.P. Intl. Sci.: AH Zeist, 2001, and earlier volumes.

(92) (a) Grossman, E.; Gouzman, I. *Nucl. Instr. Meth. Phys. Res. B* **2003**, *208*, 48-57. (b) Packirisamy, S.; Schwam, S.; Litt, M. L. *J. Mater. Sci.* **1995**, *30*, 308-320.

(93) Lorenzini, E.; Sanmartín, J. *Sci. Am.* **2004**, *291*, 50-57.

(94) Frisbee, R. H. J. *Propulsion Power* **2003**, *19*, 1129-1154.

(95) Orban, R. *J. Coated Fabrics* **1989**, *18*, 246-254.

(96) Grace, M.; Chand, N.; Bajpai, S. K. *J. Engineered Fibers Fabrics* **2009**, *4*, 24-35.

(97) Park, S.; Jayaraman, S. *MRS Bull.* **2003**, *28*, 585-591.

(98) Kim, Y. K.; Lewis, A. F. *MRS Bull*. **2003**, *28*, 592-596.

(99) *Intelligent Textiles for Personal Protection and Safety*; Jayaraman, S.; Kiekens, P.; Grancaric, A. M., Eds.; IOS Press: Amsterdam, Netherlands, 2005.

(100) *Wearable Electronics and Photonics*; Tao, X., ed.; Woodhead Publishing: Cambridge, U.K., 2005.

(101) Bigg, D. M. *Short Fibre-Polym. Compos.* **1996**, 144-167.

(102) McNaughton, T. G.; Horch, K. W. *J. Neurosci. Methods* **1996**, *70*, 103-110.

(103) *Electroless Plating*; Mallory, G. O.; Hajdu, J. B., Eds.; AESF: Orlando, 1990, Chapters 1 and 14.

(104) Liu, X.: Chang, H.; Huck, W.; Zheng, Z. *ACS Appl. Mater. Interfaces* **2010**, *2*, 529-535.

(105) (a) Vaia, R. A., Lee, J.-W.; Click, W.; Price, G.; Wang, C.-S. *Mat. Res. Soc. Symp. Proc.* 1998, 519(Organic/Inorganic Hybrid Materials), 201-209. (b) Vaia, R. A., Lee, J.-W., Wang, C.-S., Click, W., Price, G. *Chem. Mater.* **1998**, *10*, 2030-2032.

(106) Pinto, N. J.; da Silva, A. N. R.; Fachini, E.; Carrion, P.; Furlan, R.; Ramos, I. *Polym. Preprints* **2003**, *44*, 138-139.

(107) Ochanda, F.; Jones, Jr., W. E. *Langmuir* **2005**, *21*, 10791-10796.

(108) Burch, R. R. In *Metallized Plastics 3*; Mittal, K. L. Ed.; Marcel Dekker: New York, 1998; pp. 45-54.

(109) Green, T. *Gold Bull.* **2007**, *40*, 105-114.

(110) Chong, E. K.; Stevens, M. G. In *Metallized Plastics 5 & 6*; Mittal, K. L. Ed.; V.S.P. Intl. Sci.: Utrecht, 1998; pp. 409-422.

(111) Zavadskii, A. E.; Zakharova, I. M.; Zhukova, Z. N. *Fibre Chem.* **1998**, *30*, 6-10.

(112) Goldenstein, A. W.; Rostoker, W.; Schossberger, F. *J. Electrochem. Soc.* **1957**, *104*, 104-110.

(113) Abrantes, L. M.; Fundo, A.; Jin, G. *J. Mater. Chem.* **2001**, *11*, 200-203.

(114) Kim, D.; Kim, J.; Yoon, J.; Lee, W.; Jung, S. *Surf. Interface Anal.* **2006**, *38*, 440-443.

(115) Chen, C.; Chen, B.; Hong, L. *Chem. Mater.* **2006**, *18*, 2959-2968.

(116) Winters, E. D.; Coronati, J. M.; Braski, D. M.; Watkins, D. R. *Plating Surface Finishing* **2000**, *87*, 68-75.

(117) San March, C.; Moody, N. R.; Cordill, M. J.; Lucadamo, G.; Kelly, J. J.; Headley, D.; Yang, N. *Mat Res. Soc. Symp. Proc.* **2004**, *821*, 281-286.